UNIVERSITÀ DEGLI STUDI DI CATANIA
DOTTORATO DI RICERCA IN FISICA

Stefania Tropea

EXPERIMENTAL STUDY ON CARBON FRAGMENTATION FOR HADRONTHERAPY

Ph.D. Thesis

Tutor:
Prof. F. Cappuzzello
Co-Tutors:
Dr. C. Agodi
Dr. M. De Napoli

Ph.D. Coordinator:
Prof. F. Riggi

XXVI CICLO 2010/2013

"Nothing in life is to be feared, it is only to be understood.
Now is the time to understand more, so that we may fear less."
Marie Curie

Contents

Introduction

Nowadays, one of the most advanced methods for solid tumors treatment is represented by hadrontherapy, a radiotherapy technique which applies collimated beams of protons or heavier ions for the sterilization of tumor cells. Particularly, hadrontherapy is a high precision technique of external radiotherapy which yields a better perspective for defeating radioresistant tumors and it has given a boost to the use of radiation in the fight against cancer.

Due to their very favourable profile of the released dose in tissue, the charged hadron beams can be very effective in destroying the tumor and sparing the adjacent healthy tissue in comparison to the standard X-ray based treatments. On the other hand, the use of accelerated particles requires appropriate methods for accurately evaluate the dose distribution inside and outside the planned target volume during the irradiation treatment.

The most important difference between protons and heavier ions is the increased biological effectiveness of the latter, i.e. a lower physical dose is needed with ions to obtain a given biological effect. For carbon ions, which are considered the optimal choice, the effect of the favourable absorbed dose distribution, which is highly localized, is enhanced by the large relative biological effectiveness (RBE) towards the end of the particle range, offering an additional advantage for slow growing radioresistant tumors.

Nevertheless, the carbon ions based therapies are still not completely under control as great uncertainties affect the dose distributions inside the patient due to the nuclear interactions between carbon ions and the traversed human body. Indeed, when the carbon beam penetrates matter, the primary ions can be fragmented as a result of the collisions with the tissue atomic nuclei. The collisions along the carbon path lead to the attenuation of the primary beam intensity and the production of secondary fragments.

Neutrons and ions lighter than carbon are produced as hydrogen, helium, lithium, beryllium and boron isotopes. These lighter fragments have longer

ranges and wider energy distributions with respect to the primary particles and give rise to a characteristic dose *tail* behind the Bragg peak. As far as the biological effect of ion radiation is dependent on the particle field composition, a detailed knowledge of the fragmentation process is essential in order to guarantee the appropriate treatment accuracy.

Currently, the Monte Carlo codes are the most powerful tools able to precisely compute the biological dose to be delivered within a modern treatment planning system. However, the accuracy of a Monte Carlo simulation is associated to the reliability of the physical processes implemented in the code. In particular, for a realistic estimation of fragmentation products, nucleus-nucleus models inside the code have to be validated versus experimental data, which are still a small amount in the literature.

As a consequence, the main goal of the present work consist in estimating the double-differential fragmentation cross sections with respect to energy and angle in the energy range of interest for hadrontherapy.

After an overview of the historical development of radiotherapy and, more specifically, of hadrontherapy, the physical and biological rationale of carbon ions application in tumor treatments are dealt with in Chapter 1, focusing particularly on the fragmentation issue. In order to extract fragmentation cross sections in different experimental conditions, two measurements were performed at intermediate energies on both a thin carbon target and different tissue-equivalent targets, and a third one were done in the relativistic energy domain on a thicker carbon target. In Chapter 2 the experimental devices used in order to perform the three experiments have been described.

The first two experiments were carried out at the Laboratori Nazionali del Sud (LNS-INFN) in Catania with a beam of carbon ions at 62 AMeV. The cross sections angular and energy distributions were obtained for the thin carbon target analysis and also a comparison with those extracted by means of the GEANT4 Monte Carlo code were performed. The results are shown and discussed in Chapter 3 together with those associated to the second experiment done at the same energy but on thick tissue-equivalent targets. In Chapter 4 the preliminary results of the measurement performed at the GSI laboratory (Darmstadt, Germany) with a 400 AMeV carbon beam and the comparison with those obtained with the FLUKA Monte Carlo code are presented and discussed. In the end, the conclusions of the whole work done are drawn and the future perspectives are outlined.

Chapter 1

Hadrontherapy

Cancer is a group of diseases characterized by uncontrolled growth and spread of abnormal cells. If the spread is not restrained, it can result in death. Cancer is caused by both external factors (tobacco, chemicals, radiation, and infectious organisms) and internal factors (inherited mutations, hormones, immune conditions, and mutations that occur from metabolism). These causal factors may act together or in sequence to initiate or promote carcinogenesis.

Malignant neoplasms are the main cause of death among persons aged 45 to 64, for both men and women. Overall, an estimated 12.7 million new cancer cases and 7.6 million cancer deaths occurred in 2008 worldwide, with 56% of the new cases and 63% of the deaths occurred in the less developed regions of the world. As shown in Figure 1.0.1, the most commonly diagnosed cancers worldwide are lung (12.7%), breast (10.9%) and colorectal cancers (9.7%). The most common causes of cancer death are lung (18.2%), stomach (9.7 %) and liver cancers (9.2%).

Faced with increasing numbers of cancer cases, a major public health issue, researchers and practitioners are mobilising the world over. Indeed, this pathology is rising sharply in Europe: between 2000 and 2020 the number of new cases is expected to rise by 50% [1].

The goal of any cancer therapy is to destroy the malignant cells in the body while doing minimal damage to the healthy tissue. Modern cancer therapies, no matter if they are chemotherapy, targeted medications, surgery, X-ray therapy, or particle beam therapy, are all about collateral damage: destroy the cancer but safeguarding the patient life [2]. However, radiation therapy can be considered the most important, effective and cost effective treatment modality for all types of solid malignancies.

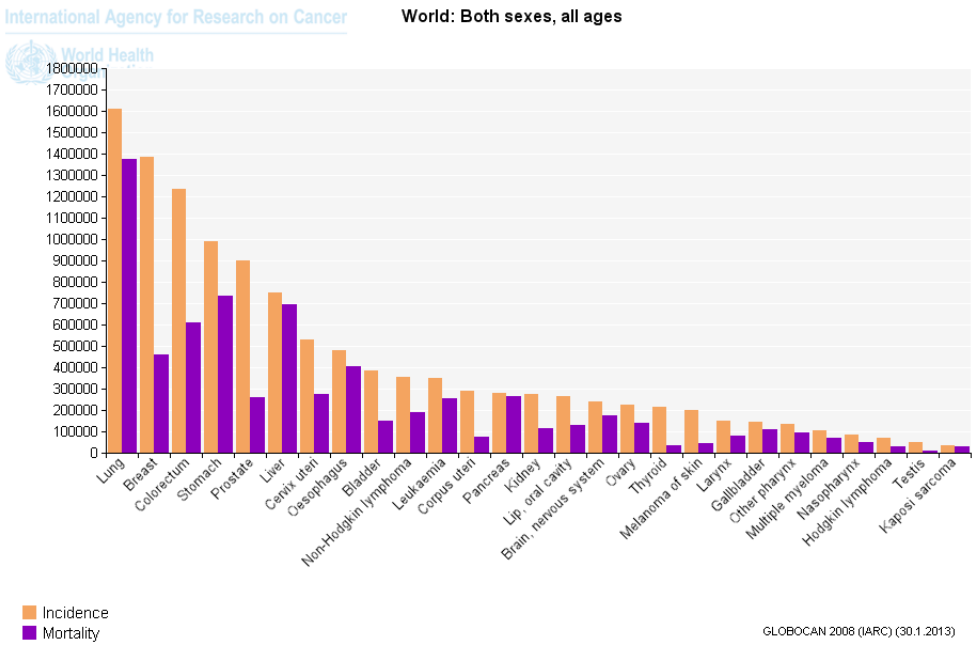

Figure 1.0.1: Incidence and mortality data for all ages and both sexes [2].

It has been estimated that about 45% of all cancer patients can be cured (excluding those suffering from non-melanoma skin cancers). Radiation therapy contributes to the cure of approximately 23% of all cancer patients, when used alone (12%) or in combination with surgery (6%) or chemotherapy-immunotherapy (5%). Thus, about half of the cancer patients who are cured benefit from radiation therapy. This proportion illustrates the important role of radiation therapy in cancer management [3]. Up to 2008, in industrialized countries, about 70% of cancer patients have been referred to a radiation therapy department for at least part of the treatment. The majority has been treated with "conventional" photon beam therapy, which for that reason remains the reference radiation treatment modality.

The impressive development and progress in conformal therapy with photons and, more recently, with protons, raises a difficult issue: the extent to which photon or proton beam therapy has reached a plateau in development (at least as far as physical selectivity is concerned). A search for improvement is actually directed to alternative radiation modalities, such as ion beam therapy.

1.1 Historical background and evolution of hadrontherapy

The era of radiation treatment began in the closing years of the nineteenth century, chiefly with the X-rays discovery, done by German physicist Wilhelm Conrad Röntgen on November 8, 1895 [4], and reported to the world shortly after the first of the year 1896 [5]. Röntgen's discovery was a scientific bombshell, and was received with extraordinary interest by both scientists and laymen. The discovery of a new form of energy that could penetrate solid objects and record their structure excited Röntgen's scientific contemporaries who recognized instantly that this finding could change medical practice forever. A century later, the vastly more sophisticated arts of medical imaging are still based upon the recognition that body parts absorb a beam of X-rays according to their density, producing an image which allows identification of body structures, as well as the recognition of abnormalities, reflective of injury and disease conditions.

By the first few months of 1896, X-rays were being used to treat skin lesions prior to any understanding of the beams physical or biological characteristics. The driving force was, of course, patients overwhelming need of treatment for uncontrollable and debilitating diseases. Particularly, Leopold Freund, a dermatologist and professor of radiology at the Medical University of Vienna, was the first physician to use ionizing radiation for therapeutic purposes. In 1896, a year after discovery of X-rays and the same year that Antoine Henri Becquerel discovered radioactivity, Freund successfully treated a five-year-old patient in Vienna suffering from hairy moles covering her whole back. The case was published in 1901 and in 1903 Freund published the first textbook on radiation therapy [6].

Shortly thereafter, in 1898, Marie and Pierre Curie discovery of radium and polonium stimulated speculation that radioactivity also could be used to treat disease. Indeed, reports of the use of radium (*curietherapy*[1]) occurred throughout the first decade of the twentieth century.

In retrospect, it is clear that lack of knowledge of the biological effects and mechanisms of actions of the new rays led to much morbidity and poor

[1]Curietherapy (nowadays referred to as brachytherapy) is a term used to describe the short distance treatment of cancer with radiation from small, encapsulated radionuclide sources. This type of treatment is given by placing sources directly into or near the volume to be treated. The dose is then delivered continuously, either over a short period of time or over the lifetime of the source to a complete decay. Most common brachytherapy sources emit photons. However, in a few specialized situations, β or neutron emitting sources are used.

cancer control. Particularly, it took until 1904, when Edison's assistant Clarence Dally died following injuries to his hands and arms, that physicians and physicists took the possibly fatal power of the X-rays into account. During this *discovery era*, which lasted until the early 1920's, radiation therapy remained a more or less empirical science, as far as the major progress originated from clinical application. However, two general tendencies started to be visible: the clinical results were improved by a greater conformity of the applied radiation to the target volume and by an increased biological effectiveness of the radiation.

The next major era in radiation therapy began during the 1920's, primarily as the result of two major contributions. The first was the invention by W.D.Coolidge [7] of a sealed-off vacuum X-ray tube, equipped with an hot tungsten cathode, which could be operated at the unprecedented energies of 180.000 to 200.000 volts, thus introducing *the kilovoltage era* in radiotherapy. Unfortunately, X-rays generated by these tubes were fairly *soft* and, from the medical point of view, the depth-dose curves were particularly disadvantageous since the maximum dose would be delivered at the skin surface and then would rapidly fall off with the depth in the tissue. Secondly, that era witnessed an important advance for all uses of X-rays and γ-rays, the adoption of the röntgen R as the internationally accepted unit of radiation exposure by the International Congress of Radiology in 1928 [8], later succeeded by the absorbed dose unit, called *rad*[2].

Although the kilovoltage era was one of great achievement, radiotherapists were severely prevented by the physical limitations of dose distribution since, with energies between 50 kV and 200 kV, it was very difficult to deliver sufficient doses into deep-seated tumours, primarily because of the associated unavoidable skin toxicity. It was obvious that beams of higher energy were needed, and by the early 1950's, several groups of physicists had begun to come up with new ideas for devices of much higher energy such as the cobalt teletherapy machines and the megavoltage linear electron accelerators, giving rise to the *the megavoltage era*. Following the discovery of artificial radioactivity in 1934 done by Irène and Frédéric Joliot-Curie, ^{60}Co was adopted as an alternative source of high-energy γ-rays for teleradiother-

[2]More precisely, exposure is given by $X{=}dQ/dm$, where dQ is the absolute value of the total charge of the ions of one sign produced in air when all the electrons and positrons, liberated or created by photons in mass dm of air, are completely stopped in air. The unit used for exposure is the röntgen R, where 1 R = 2.58 $\times$ 10^{-4} C/kg. In the SI system of units, röntgen is no longer used and the unit of exposure is simply 2.58 $\times$ 10^{-4} C/kg of air [9]. The old unit of the absorbed dose *rad* (see Section 1.2.1) is defined so that 1 rad = 100 erg/g.

apy, with a higher dose rate than could be achieved with radium. Moreover, the 1.33 MeV maximum energy of the emitted gamma made it possible to obtain far better depth-dose curves, showing a maximum at about 5 mm below the skin surface and markedly decreasing the dose to the superficial tissues, as shown in Figure 1.1.1.

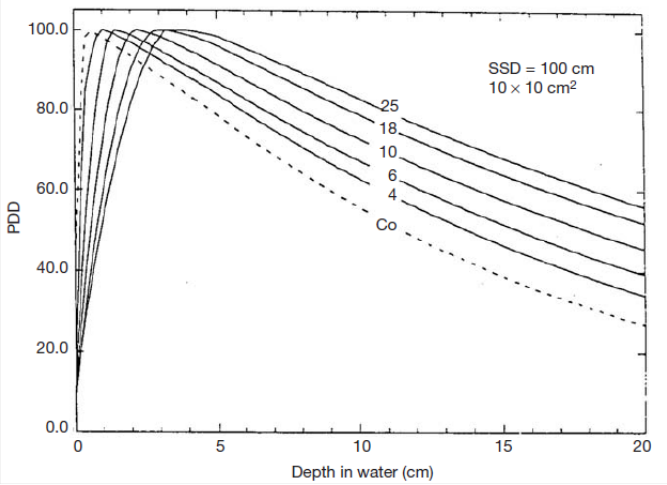

Figure 1.1.1: Percentage Depth-Dose (PDD) curves in water for a 10×10 cm^2 field at a Source to Surface Distance (SSD) of 100 cm for various megavoltage photon beams ranging from ^{60}Co γ-rays to 25 MV X-rays [9].

On the other hand, the most important developments in radiotherapy arose when a high voltage accelerator was developed in 1932 by R. Van de Graaff [10] and, five years later, the first hospital-based accelerator of this type, a 1 MeV air-insulated machine, was installed in Boston. A further improvement in treatment delivery techniques came with the development of the *betatron* in 1943 by D.W. Kerst [11], through which high energy X-rays and electron beam therapy became feasible. As a result, the first patient was irradiated in 1949 with X-rays generated by 20 MeV electrons from a Kerst betatron installed in Urbana (USA). Betatrons were widely circulated but, since the mid 1970's, their application showed a gradual decline because of some disadvatages such as the relatively low intensity of the X-ray beams produced, the small treatment field area together with the relevant weight, which made these machines unhandy. In the mean time, the advances made during the World War II made it possible to use microwave generators for electron acceleration, leading to the born of the first *radiofrequency linear*

accelerators designed by C.W. Miller [12], which were soon to take up a dominant place on the world market of medical accelerators [13] replacing betatrons.

Nowadays, as sources of radiation for modern radiotherapy with collimated beams, the *electron linear accelerators* (linacs) are still used. Such accelerators are capable of producing both electrons and photons beams with energies varying between 3 and 25 MeV. While electron beams are suitable for the treatment of superficial or semi-deep tumors, the photon beams from a linear accelerator can be applied for a very efficient treatment of tumors situated at a depth of many centimeters inside the body with respect to the skin surface. In order to irradiate selectively such targets, thus achieving a better conformation of dose to the tumor, sophisticated irradiation techniques have been developed which involve the use of multiple beam entry ports onto a point, usually conciding with the geometrical center of the target (cross-fire technique). These irradiation techniques are applied by having the structure containing the linac rotate around a horizontal axis (*gantry*). The most recent *Intensity Modulated Radio-Therapy* (IMRT) makes use of 6-10 entrance ports. The beams may be non-coplanar and their intensity is varied across the irradiation field by means of variable collimators (*multileaf collimators*) that are computer controlled. Nowadays, in the developed countries, every years about 20000 patients out of 10 million inhabitants, are treated with high-energy photons and about 8000 linacs are used worldwide for cancer treatment.

Despite the remarkable development of conventional radiotherapy, it was found that some tumors, called *radioresistant tumors*, respond poorly to the photon treatments and sometimes even non-radioresistant tumors, located near critical body parts, can not be given a tumorocidal dose because of unavoidable dose to the surrounding normal tissues. In this context, the tendency which drove the historical development of radiotherapy was the searching of an increased biological effectiveness of radiation. In order to overcome both the physical and the biological limitations of conventional radiotherapy the use of neutrons, protons and heavier charged particles was proposed, which led to the born of the "*Hadrontherapy*".

"Hadrontherapy" is a collective word covering all forms of radiation therapy which use beams of particles made up of quarks: neutrons, protons, pions, antiprotons, helium (i.e. alpha particles), lithium, boron, carbon and oxygen ions. As in the case of photons, the use of hadrons for medical applications is sensibly influenced by the scientific progress and it is strictly related to the historical development of the accelerators technology [14].

Fast neutrons (i.e. neutrons having kinetic energies between a few MeV and a few tens of MeV) were the first hadrons used in radiotherapy soon after the invention of the cyclotron by Ernest Lawrence and Stanley Livingston in 1930 [15]. Soon after, in 1935, John Lawrence, who was a medical doctor in Yale, joined his brother Ernest in Berkeley for appliying the new powerful accelerator for medical purposes [16]. The two main applications were the production of radioisotopes and, later, the therapeutical use of fast neutron beams. Neutrons act via their scattering and recoil ions which are, in biological tissues, mostly low energy protons and, as a consequence, produce a greater biological damage with respect to photons. At the end of 1938, the first patients were treated with neutrons but the technique was primitive and the doses given to healthy tissues too high. Indeed, even if a better tumour control was achieved, thanks to the increased biological effectiveness of neutrons, the poor depth dose profile unfortunately compensated this advantage with severe late effects in normal tissues. For this reason, some years later, in 1948, after the effects evaluated on 226 patients, Dr. Robert Stone concluded that neutron therapy had not to be continued [17]. It has to be noted that today neutron therapy is mostly restricted, in some laboratories, for the treatment of radio resistant tumours of the salivary glands, while in most countries this technique has been terminated.

The application of high-energy beams of heavy charged particles to radiotherapy was first considered by Robert R. Wilson, who was one of Lawrence's students. In 1945 he designed a new 160 MeV cyclotron and, one year later, proposed the use of proton beams in radiation oncology [18]. In fact he had measured depth dose profiles at the Berkeley cyclotron with a significant increase in dose at the end of particle range, the so called *Bragg peak*, which had been observed fifty years before in the tracks of alpha particles by William Henry Bragg [19]. As soon as Wilson analized the stopping process of protons in matter, he understood that, due to the Bragg peak, the dose can be concentrated on the tumour target sparing healthy tissues better than what can be done with X-rays and wrote the famous seminal paper [18], which is considered the first work on hadrontherapy (see Figure 1.1.2). Two years later the 184-inch synchrocyclotron at Lawrence Berkeley Laboratory (LBL) became available for experiments and the physical and radiobiological properties of proton beams were thoroughly investigated by Cornelius Tobias [20], thus confirming the predictions made by Wilson. Patient treatments started in 1954 at LBL, first with protons and later, in 1957, with helium beams. Radiotherapy with heavier ions started in 1975 at the Bevalac facility of the LBL mostly appliying beams of ^{20}Ne.

In the first trials at Berkeley, the beam was distributed to the target volume adapting methods from conventional photon therapy, in which the photon beam is passively shaped by collimators and absorbers. Thus, the energy modulation of charged particle beams was first performed with modified collimator and absorber techniques [21].

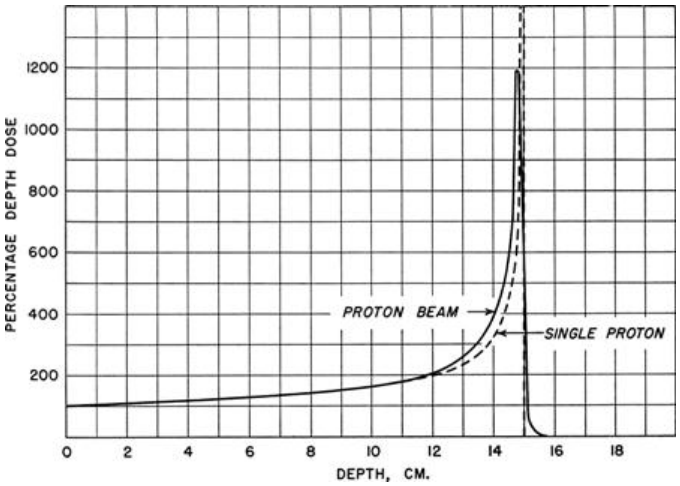

Figure 1.1.2: The original picture from Robert R. Wilson's paper on protontherapy [18].

In other words, ions were treated as photons without making use of their most important characteristic, i.e. the electric charge, which makes their beams easy to detect and to control by means of magnetic fields. This was also because of the fact that, in those early times, the computer power available was too poor for a control system of an active beam scanning, as described in the next sections.

It has to be remarked that the first hadrontherapy treatments were performed by means of particle accelerators that had originally been built for nuclear physics experiments and were then adapted to tumour therapy. This was the case in Berkeley as well as at Harvard Cyclotron Facility, which made the largest impact on the development of protontherapy and where, up to now, the highest number of patients have been successfully treated. Some years later, other nuclear physics laboratory in USSR and Japan set up proton beams for therapy and in 1984 the Paul Scherrer Institute (Switzerland) did the same. The clinical proton beam currently used in the facility

CATANA[3] for eye melanoma treatments at Laboratori Nazionali del Sud (LNS, Catania, Italy) is also an example of beams produced by a superconducting cyclotron (SC) originally designed for nuclear physics experiments and adapted for therapy [22].

As far as all the treatment facilities were located in physics laboratories, the irradiation condition was far from ideal and, although many times it was felt and said that hadrontherapy field could not develop without dedicated equipment, this step took almost 20 years. Indeed, the first hospital-based centre was built at the Loma Linda University Center (California), which signed an agreement with Fermilab (founded and directed for many years by Robert Wilson) and treated the first patient in 1990. Afterwards, a smooth conversion from a physics laboratory to a hospital facility took place in Japan, where from 1983 to 2000 about 700 patients were treated at the Proton Medical Research Center (PMRC, University of Tsukuba). Moreover, USA proton therapy was further expanded during the 1990s. Over 50000 patients have worldwide been treated with proton beams by now and other facilities are under construction or in planning stages [23].

Between 1954 and 1974 at Berkeley, under the leadership of C. Tobias, about 1000 pituitary tumors were treated with protons. A few years later, heavier ions, helium in 1957 and argon in 1975, came into use at the LBL. As a consequence, 2800 patients received treatments to the pituitary glands with helium beams, thus achieving a better dose conformation to the tumor with respect to protons, and moving the first step towards the light ion radiosurgery. About 20 years later, argon beams were tried in order to increase the effectiveness against radioresistant tumors, but problems arose owing to non-tolerable side effects in the normal tissue. After a few irradiations, Tobias and collaborators used lighter ions, first silicon and then neon ions for 433 overall patients, until Bevalac stopped operation in 1993. Only towards the end of the program it was found that the neon charge (Z=10) is too large and undesiderable effects were produced in the traversed and downstream healthy tissues [24].

Further experimental studies were needed, but only in the early 1990's carbon ions were recognized as the optimal ion choice. In fact their effects in the tissue entrance are similar to those of X-rays and protons, while just at the end of their path in matter, ionization density is definitely larger and not repairable damages are produced to the cellular systems. This resulting radiation field is a common feature to the light ions in general, but carbon ions currently represent the best compromise for treatments, especially in

[3]Centro di Adroterapia ed Applicazioni Nucleari Avanzate.

case of radioresistant tumors, as shown in the next sections.

In 1994 the Heavy Ion Medical Accelerator (HIMAC) dedicated to radiotherapy, by virtue of the proposal made by Yasuo Hirao [25] and collaborators, started with carbon ions at National Institute of Radiological Science (NIRS) in Chiba (Japan) using similar technical concepts as those pioneered at Berkeley. The first patient has been treated with a carbon ion beam of energy up to 400 AMeV, corresponding to a maximum range of 27 cm in water. At the same time, new technical solutions were developed almost in parallel at the Gesellschaft für Schwerionenforschung (GSI) in Darmstadt, Germany. By the end of 2007 more than 4000 patients have been treated at the HIMAC facility showing that, among light ions, a better tumor control rate can be achieved with carbons.

1.2 Physical aspects of radiotherapy with ion beams

1.2.1 Dose and therapeutic ratio

The fundamental goal in radiation oncology is the local control of the tumour and, in some situations, of surrounding diffusion paths (*loco-regional radiotherapy*). In order to reach this objective, one must deliver to the tumor, which may be considered in physical terms as the *target*, a sufficiently high *dose* of radiation so as to destroy it, at the same time mantaining the dose to the surrounding healty tissues, inevitably involved in the irradiation, within such limits so that they do not undergo serious or even irreversible damage or complications.

The dose deposited in tissue is the most important physical quantity in radiotherapy. The *absorbed dose* [26] is defined as the mean energy $d\bar{\epsilon}$ imparted by ionizing radiation to a mass element dm in a finite volume by,

$$D = \frac{d\bar{\epsilon}}{dm}. \tag{1.2.1}$$

The absorbed dose is measured in gray (Gy), being 1 Gy = 1 J/kg. For example, in conventional radiotherapy with photons and electrons, doses of the order of 60-70 Gy are deposited in the tumour tissues in amounts of about 2 Gy per session over about 30 days.

In the hypothesis of a fairly accurate identification of the target, it is possible to evaluate the probability of obtaining the local control of the tumour through the analysis of the so-called *dose-effect curves*. They represent for tumour tissues the possibility of obtaining the desired effect as a function of the dose delivered, and for healthy tissues the probability of producing

serious or irreversible damage, always as a function of the absorbed dose by the same tissue. In Figure 1.2.1 hypothetical dose-effect curves are shown, as function of the absorbed dose, for a generic tumour tissue (A) and for the healthy tissue involved in the irradiation (B). As can be seen, the absorbed dose necessary to achieve a probability close to 100% of obtaining local control of the tumour corresponds also to a very high probability of producing serious complications in the healthy tissue, when this receives the same dose. The two sigmoid curves plotted in Figure 1.2.1 are usually referred to as Tumor Control Probability (TCP, curve A) and Normal Tissue Complication Probability (NTCP, curve B) [9].

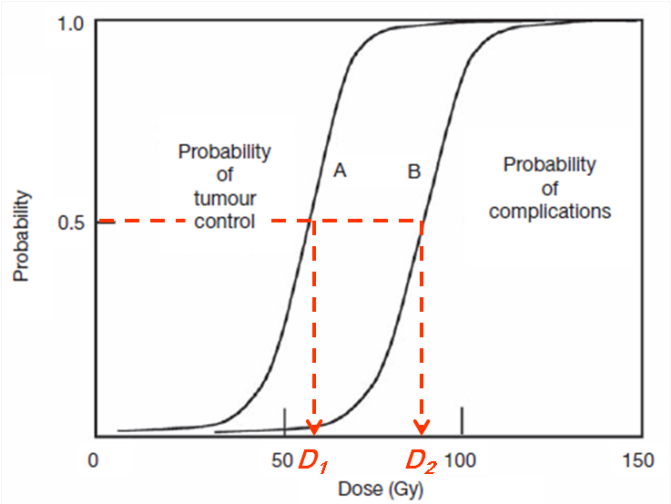

Figure 1.2.1: Dose-effect curves for neoplastic (A) and normal (B) tissues.

In the daily practice, the radiotherapist has to find a compromise between the local control of the tumour and the possible emergence of complications: the possibility to find such a compromise can be expressed quantitatively by the *therapeutic ratio*, i.e. the ratio D_2/D_1 [9] between the dose corresponding to a 50% probability of producing complications D_2 and the dose corresponding to a 50% probability of obtaining the local control of the tumour D_1 [27]. On the basis of these considerations, it is clear that the probability of curing the tumour without unwanted side effects increases in line with the ballistic selectivity or conformity of the irradiation delivered.

The optimum choice of radiation dose delivery technique in the treatment of a given tumour is such that it maximizes the TCP and simultaneously

minimizes the NTCP. For a typical good radiotherapy treatment, TCP $\geq$ 0.5 and NTCP $\leq$ 0.05. The case shown in Figure 1.2.1 refers to an ideal situation; in reality, the therapeutic ratio varies with many factors, such as the dose rate and Linear Energy Transfer (LET, see Section 1.4) of the irradiation, the presence of radiosensitizers or radioprotectors, the design of the treatment plan and the precision of implementation of the treatment plan.

Particularly, the probability of curing tumours can be increased by using charged hadrons beams because the absorbed dose is more confined in the tumour tissue with respect to electrons and photons application, thus allowing an enhanced ballistic precision. Moreover hadrons show increased biological effects respect to electromagnetic radiation and also respect to protons. This last feature makes them more successful also in the treatment of radioresistant tumours. Concerning carbon ions treatment, an example of the resulting tumor control probability curve with respect to photons is shown in Figure 1.2.2 and the related study confirmed the effectiveness of carbon ion therapy for severely radioresistant tumors [28].

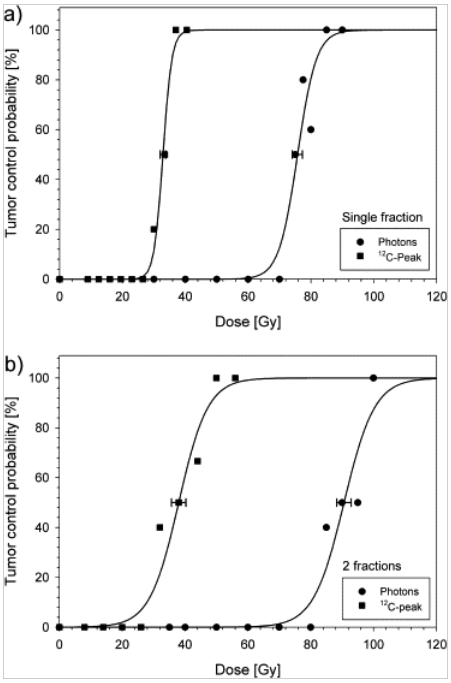

Figure 1.2.2: Dose-response curves for (a) a single dose fraction and (b) two dose fractions of photons and carbon ions [28].

Moreover carbons show increased biological effects also with respect to protons (see section 1.4). Thus the therapeutic advantages of carbon beams when compared to electron, photon and also proton beams can be found at a macroscopic scale (high level conformation) as well as at the microscopic scale (possibility of varying the radiobiological properties). The latter deals with microscopic distribution of the deposited energy, which changes when different ion beams are considered. For this reason it is often said that hadrons, and specifically carbons, as *densely ionizing* radiation, in contrast to the *sparsely ionizing* radiation such as X-rays, γ-rays and electrons.

1.2.2 Inverse depth-dose profile: stopping of ions in matter

The main reason for using charged particle beams in radiotherapy is their *inversed dose profile*, i.e. the increase of energy deposition with penetration depth, which makes them a more advantageous choice with respect to electromagnetic radiation. As already mentioned, the increase of ionization density along the ions path in matter was firstly described, for α particles slowing down in air, by W.H. Bragg in 1905 [19]. As a result, ions depth-dose profiles are still known as *Bragg curves*.

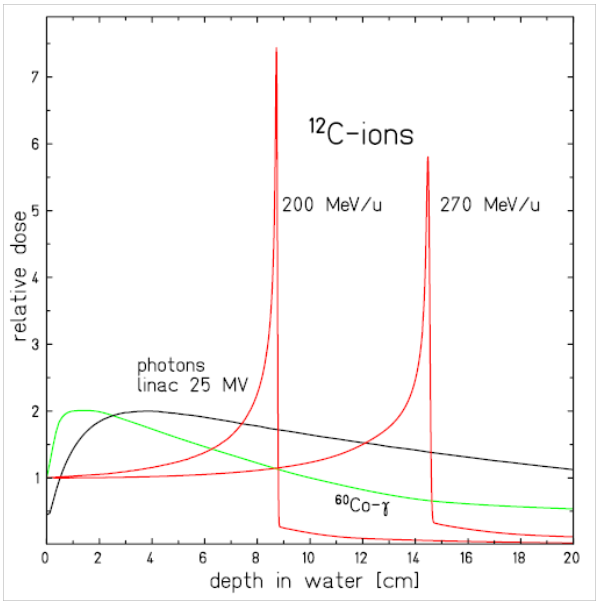

Figure 1.2.3: Depth-dose profiles of ^{60}Co radiation, megavolt photons, and ^{12}C ions in water [29].

Many years later R. Wilson [18] proposed the application of protons and heavier ions for precision exposures in radiotherapy. A comparison of depth-dose profiles for electromagnetic radiation (^{60}Co and megavolt photon beams) and carbon ions beams is displayed in Fig. 1.2.3 [29].

The peculiar physical processes which characterize respectively electromagnetic radiation and charged particles interaction with matter directly affect their different depth dose profiles. Concerning photons interaction, three are the possible processes: the photoelectric effect, the Compton scattering and the electron-positron pair production. The relative probability of each of these interaction mechanisms is a function of the incident photon energy and the atomic number Z of the absorbing material. On the other hand, charged particles dissipate their energy mainly via interaction with the electrons of the target material, which are subsequently emitted as δ-*electrons*, i.e. the maximum energy electrons able to ionize other medium atoms. More than 75% of the initial energy is lost in the ionization process and only 10 to 20% in the target excitation [30]. Particularly, the interaction strength is directly correlated with the interaction time so that at high velocities the energy transfer to the target is small but grows when the particles are slowed down.

As can be seen in Figure 1.2.3, for low-energy photons the stochastic absorption by photoelectric and Compton processes yields an exponential decay of absorbed dose with penetration depth and the beam doesn't show a path of finite lenght. For higher photon energies the produced Compton electrons are strongly forwardly scattered and transport some of the transferred energy from the surface to deeper layers, yielding an increase in dose in the first few centimeters. For high energy *bremsstrahlung* radiation[4], which is mostly used in conventional therapy, this maximum is shifted a few centimeters from the surface of the patient body, thereby improving the target-to-entrance dose and sparing the very radiosensitive skin.

In contrast, the energy deposition of charged particles, like protons or heavier ions, shows a completely different trend. When ions enter an absorbing material, they are slowed down. The rate of average energy loss per unit path lenght for a given target medium increases with decreasing particle velocity, giving rise to a sharp maximum in ionization near the end of the range. Thus the depth-dose distribution is characterized by a relatively low

[4]Like charged particles, electrons also suffer a collisional energy loss when passing through matter. However, because of their small mass, an additional energy loss mechanism comes into play: the emission of electromagnetic radiation arising from scattering in the electric field of a nucleus, a physical process known as *bremsstrahlung*, a german term meaning *braking radiation*.

dose in the entrance region (*plateau*) near the skin and a sharply elevated dose at the end of the range, which in this case is finite and energy dependent (*Bragg peak*), as the position of the peak can be precisely adjusted to the desired depth in tissue by changing the kinetic energy of the incident ions. The ballistic precision of charged particles with respect to electromagnetic radiation is evident by looking at Figure 1.2.3. As a result, in the surrounding healthy tissues before or just behind the Bragg peak, the dose released is minimized respect to the target volume and a better compromise is achieved.

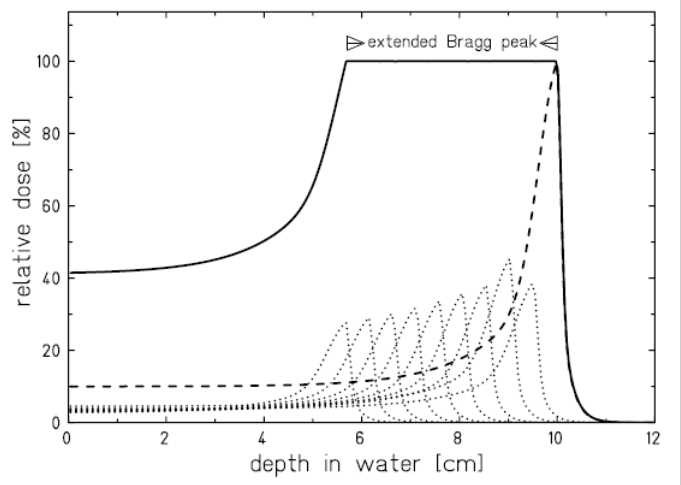

Figure 1.2.4: Construction of an extended Bragg peak by superposition of single Bragg peaks of different energy. [31].

It is important to note that, from the point of view of practical applications in radiotherapy, a monoenergetic beam with a narrow Bragg peak makes possible to irradiate a very small and localized region within the body, with an entrance dose lower than that in the peak region [32]. Indeed, the tumour volume to be treated is normally much larger than the width of the Bragg peak and the lateral spot of the particle beam. In order to fill the target volume with the necessary amount of stopping particles, the peak has to be "spread out" in the longitudinal direction. This is achieved by superimposing several Bragg peaks at different depths obtained by suitably selecting the projectiles energy distributions. The resulting depth-dose profile, known as Spread-Out Bragg Peak (SOBP), shows an "extended" Bragg peak area which has to accurately overlap the target volume (see Figure

1.2.4.).

Even if the peak-plateau ratio decreases for SOBP with respect to a pristine Bragg peak, the final dose distribution allows tumor conform treatments of enhanced quality with respect to those obtained by applying photons [31].

Radiotherapy of deep-seated tumors requires, tipically, ion beam ranges in tissue of up to 30 cm, corresponding to specific energies up to 220 AMeV for protons and 430 AMeV for carbon ions, with particle velocities $\beta \equiv v/c \approx 0.6$ and 0.7 respectively. At these velocities the energy-loss rate dE/dx in the slowing-down process is dominated by inelastic collisions with the target electrons (*electronic stopping power*) and can be well described by the *Bethe-Bloch formula* [33][34][35],

$$-\frac{dE}{dx} = Z_p^2 f(v), \tag{1.2.2}$$

with Z_p and v the charge and velocity of the projectile respectively.

The energy dependence of the specific energy loss in water for ions of interest in hadrontherapy is shown in Figure 1.2.5 [36].

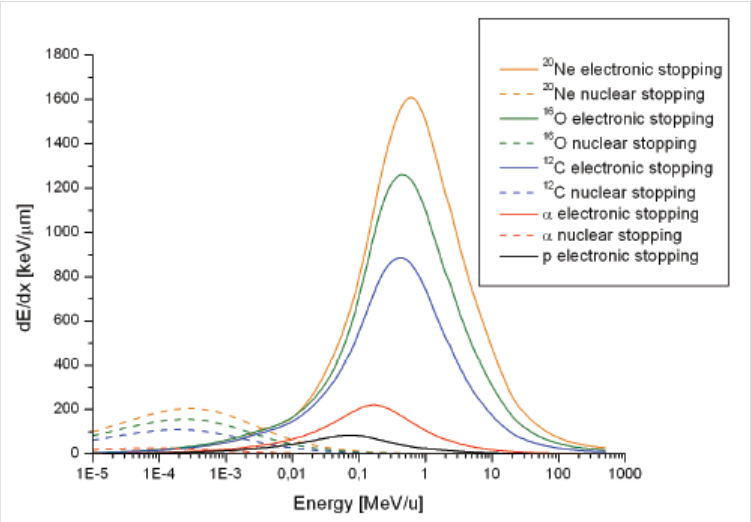

Figure 1.2.5: Electronic (full lines) and nuclear (dashed lines) energy loss per unit path length dE/dx for ions of therapeutic interest in water. dE/dx values are calculated with the *Stopping and Range of Ions in Matter* code (SRIM) [36].

At non relativistic energies, dE/dx is dominated by the $1/v^2$ term and decreases with increasing velocity while, in the relativistic energy domain,

near about $v \approx 0.96c$, a minimum is reached. Particles at this point are known as *minimum ionizing*. The minimum value of dE/dx is almost the same for all particles of the same range. As the energy increases beyond this point, the term $1/\beta^2$ becomes almost constant and dE/dx rises again due to the logarithmic dependence.

In this energy domain, the atomic electrons are completely stripped off and the projectile charge is equal to the atomic charge number Z_p. For energy below the minimum ionizing value, each particle exhibits a dE/dx curve which, in most cases, is distinct from the other particle types. At very low energy, the stopping power reaches a maximum and then drops rapidly, due to the tendency of particles to pick up electrons (see Figure 1.2.5). As a result, for light ions below about 10 AMeV, the mean charge state decreases due to the interplay of ionization and recombination processes and Z_p in equation 1.2.2 has to be replaced by the *effective charge* Z_{eff}, which is well described by the *Barkas empirical formula* [37]:

$$Z_{eff} = Z_p \left(1 - e^{-125\beta Z_p^{\frac{2}{3}}}\right). \tag{1.2.3}$$

Considering these dependences, at not relativistic energies, the energy loss rate grows up as the kinetic energy of the projectile decreases along the penetration depth, particularly in the last few millimetres of the particle path where it shows a much steeper rise. For this reason the distribution of the ionizing density produced by the charged particle along the track is characterized by a rather constant plateau, followed by a sharp maximum towards the end, where gives rise at the Bragg peak. Nevertheless, at the end of the path the stopping power drops quickly to zero because of the rapid reduction of the effective charge Z_{eff} for very low energy values.

The maximum energy loss rate, corresponding to the Bragg peak, is reached at a projectile velocity v_p of:

$$v_p \approx Z_p^{\frac{2}{3}} v_0 \tag{1.2.4}$$

where $v_0 = e^2/\hbar$ is the Bohr velocity. For ^{12}C ions this maximum occurs at a specific energy of $E_p \approx 0.35$ AMeV. At still lower projectile energies ($E_p \leq 0.10$ AMeV) elastic collisions with target nuclei begin to contribute significantly to the energy loss and dominate the stopping process at the very end of the particle path (the last few μm). This mechanism of ions energy loss is commonly called *nuclear stopping power*. Examples of this latter are reported in Figure 1.2.5 (dashed lines) for ions of therapeutic interest. The

dose contribution associated to nuclear stopping power is very small and can be neglected in radiotherapy applications [38].

1.2.3 Range straggling and lateral scattering

Assuming that stopping power is known, it is possible to calculate the *range* R of an energetic charged particle traversing a medium, i.e. the distance it travels before coming to rest. The total path length of the particle trajectory in the absorber is thus given by:

$$R(E_0) = \int_0^{E_0} \left(\frac{dE}{dx}\right)^{-1} dE, \tag{1.2.5}$$

where E_0 is the ion incident energy. For heavy charged projectiles equation 1.2.5 is a very close approximation of the *mean range* R, i.e. the average traversed absorber thickness, because heavy ions are very little scattered and travel almost on a straight line.

Ranges of various ion beams in water are shown in Figure 1.2.6(a). One can observe that the range of ions with the same energy per nucleon scales with a factor of A/Z^2, being A and Z the mass and the atomic number of the particle, respectively. As a consequence, protons and α particles show the same path in water when plotted as a function of their specific energy.

According to equation 1.2.2, the energy loss of a single carbon ion plotted as a function of the absorber depth would result in a very sharp peak near the stopping point. Actually, statistical fluctuations of the energy loss in the large number of collisions of the slowing-down process result in a broadening of the Bragg peak for an ion beam consisting of many particles. These fluctuations, responsible of a dispersion of the path length (*range straggling*), are described by the asymmetric Vavilov distribution [39] for charged particles passing through a thin layer of matter (*energy loss straggling*). In the limit of many collisions the Vavilov distribution becomes a Gaussian *f(ΔE)* given by [40] [41]:

$$f(\Delta E) = \frac{1}{\sqrt{2\pi}\sigma} e^{\frac{(\Delta E - \langle \Delta E \rangle)^2}{2\sigma^2}} \tag{1.2.6}$$

where σ is the straggling parameter which expresses the half-width at the *(1/e)*-th height. Hence, statistical fluctuations of energy loss cause a smearing of the range of the stopping particle beam and, consequently, a larger width of the Bragg peak experimentally measured. Range straggling effects for ion beams vary approximately inversely to the square-root of the atomic mass and increase as the penetration depth grows up. Indeed, at

the same penetration depth heavier ions show narrower Bragg peaks and also a steeper distal fall-off, which has a positive effect on the final level of conformation of the radiation to the tumour, as shown in Figure 1.2.6(b).

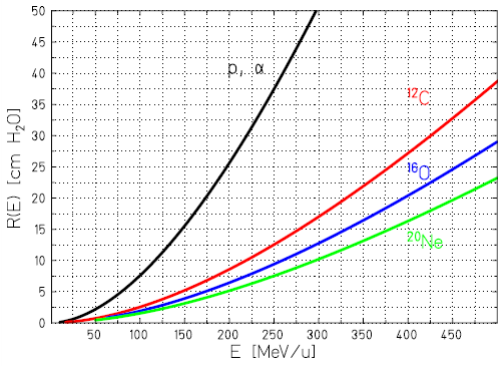

(a)

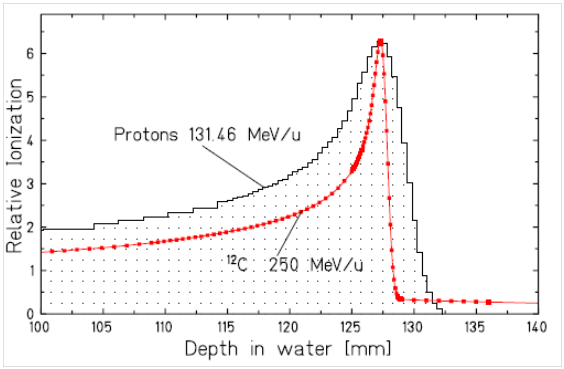

(b)

Figure 1.2.6: (a) Mean range of heavy ions in water [36] (a) and (b) measured Bragg peaks of protons and ^{12}C ions having the same mean range in water [42].

For example, the relative range straggling in tissue amounts to about 1% of the mean range of protons and only to 0.3% for ^{12}C ions [43]. In clinical practice, however, the profile of the Bragg peaks is broader, mainly due to the density inhomogeneities of the penetrated tissue.

At higher energies and longer penetration depths, the half width of the Bragg maximum becomes larger and the height smaller. Typical values for carbon ions are given in Table 1.1 [44].

Moreover, a typical fragmentation tail is also well distinguished in case

of heavy ions, but this aspect with its implications will be discussed in the next sections.

Energy (AMeV)	90	180	270	330
Range (mm)	21.3	82.8	144.3	200.5
FWHM (mm)	0.7	2.3	5.0	7.0

Table 1.1: Typical values for carbon ions Bragg curves [44].

The small lateral deflection of heavy ions penetrating through an absorber is a particular advantage in comparison to protons and is of clinical revelance for treatments near organs at risk (OAR). Particularly, multiple scattering of an incident ion stems from the small angle deflection due to collisions with nuclei of the traversed material. Numerous small angle deflections in an ion beam lead to lateral spreading of the incident ions away from the central trajectory resulting in larger divergence of the beam. Elastic Coulomb scattering dominates this process with a small strong-interaction scattering correction, while scattering due to electronic interactions, which dominate the stopping process, can be neglected. The angular distribution of the scattered particles is roughly Gaussian for small deflection angles, and the mean beam deflection is approximately proportional to the penetration depth. The Coulomb scattering of the projectiles is described very precisely in the theory of Molière [45] [46]. Measurements of proton scattering confirmed this theory [47] and a parameterization for small angles angular distribution *f(α)* [48] is given by:

$$f(\alpha) = \frac{1}{\sqrt{2\pi\sigma_\alpha}} e^{-\frac{\alpha^2}{2\sigma_\alpha}} \tag{1.2.7}$$

with:

$$\sigma_\alpha = \frac{14.1MeV}{\beta pc} Z_p \sqrt{\frac{d}{L_{rad}} \left(1 + \frac{1}{9} log_{10} \frac{d}{L_{rad}}\right)} \tag{1.2.8}$$

where σ_α is the standard deviation, p the momentum, L_{rad} the radiation length and d the absorber thickness. Values of L_{rad} for common materials can be found in [49] and can be easily computed also for compounds (e.g. water 36.08, Al 24.01, Fe 13.83, Pb 6.37 g/cm^2). Targets containing heavy elements cause a larger angular spread than targets of light elements with

the same thickness and the angular spread for heavy charged particles is small (of the order of 1 mrad for thin target) but increases significantly towards low energies due to the βpc term in the denominator of equation 1.2.8.

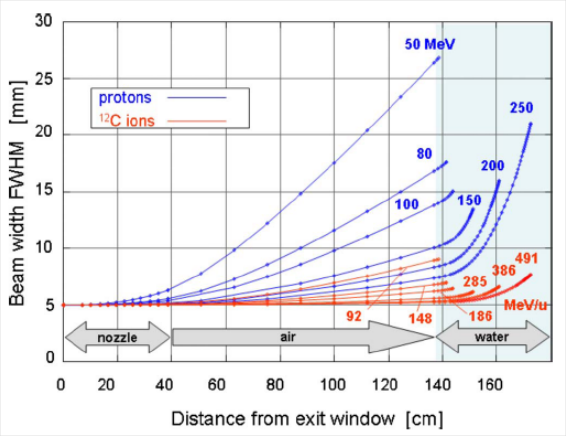

(a)

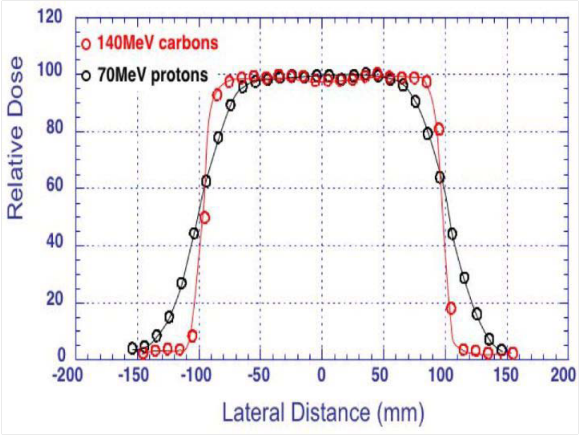

(b)

Figure 1.2.7: (a) Calculated beam spread for ^{12}C ions and protons in a typical treatment beam line [29] and (b) comparison between lateral distribution of dose deposited by proton and carbon ion beams having approximately the same range; the comparison clearly shows the improved selectivity of carbon ion beams respect to protons [50].

Comparison of beams with the same range in water (e.g. 150 MeV protons and 285 AMeV ^{12}C ions with $R = 15.6$ cm) shows that the angular spread (σ_α) for protons is more than three times larger than that for ^{12}C ions (see Figure 1.2.7(a)). This fact represents a further advantage of the clinical use of carbon ion beams and it also contributes to an enhanced ballistic precision.

Effects on lateral broadening are much more evident looking at the so called *apparent penumbra*, which is the sharpness of the lateral dose fall-off [50]. Heavier ion beams exhibit sharper lateral dose fall-offs at the field boundary than lighter ions: in Figure 1.2.7(b) the penumbras of proton and carbon beams are compared. The penumbra width increases essentially linearly with the penetration depth of the beam. For low-Z ions, such as protons, sharpest dose fall-offs are obtained when the final collimator is at the surface of the patient. For higher-Z ion beams, such as carbon ion beams, active scanning techniques without collimations will produce narrow penumbras.

1.3 The problem of nuclear fragmentation

While the stopping process of high-energy ions penetrating a thick absorber is governed by collisions with atomic electrons, the probability of nuclear reactions is much smaller, but leads to significant effects at large penetration depths. Particularly, beam fragmentation represents the main disadvantage of using carbon ion beams for tumour treatments. Ion beams suffer nuclear reactions by interacting with the elements placed along the beam line as well as inside the tissue itself. The first contribution can be opportunely reduced, and it is strictly dependent on the beam delivery system used (the best results are obtained when active systems are applied). The second one is an intrinsic contribution and therefore not eliminable, but it is important to know in details the effects on the delivered dose.

At energies of several hundred AMeV, the most frequently occurring nuclear reactions are peripheral collisions where the beam particles may lose one or several nucleons. This process can be described by the *abrasion-ablation model* [51] as illustrated in Figure 1.3.1.

Nucleons in the overlapping zone of the interacting projectile and target nuclei are abraded and form the hot reaction zone (*fireball*), whereas the outer nucleons (*spectators*) are only slightly affected by the collision. In the second step (*ablation*), the remaining projectile and target fragments as well

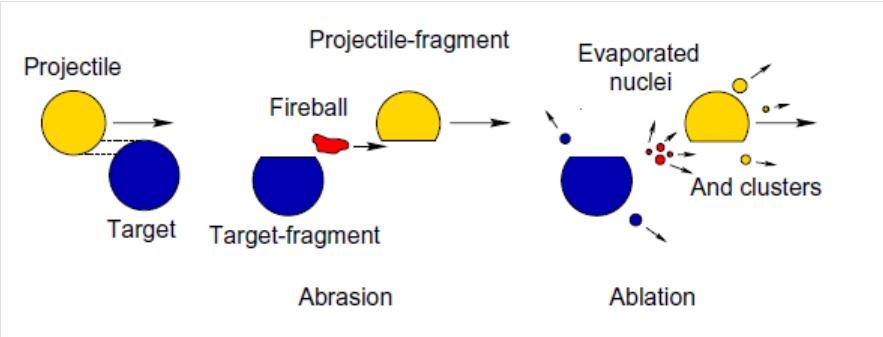

Figure 1.3.1: A simplified model of the nuclear fragmentation due to peripheral collisions of projectile and target nucleus as described by Serber [51].

as the fireball de-excite by evaporating nucleons and light clusters. Those emitted from the projectile fragments appear forward peaked in the laboratory frame due to the high velocity of the projectile. The projectile-like fragments continue travelling with nearly the same velocity and direction, and contribute to the dose deposition until they are completely slowed down or undergo further nuclear reactions. Neutrons and clusters from target-like fragments are emitted isotropically and with much lower velocities. The particles ablated from the fireball cover the range between the projectile and target emission.

Nuclear fragmentation reactions lead to an attenuation of the primary beam flux and a build-up of lower-Z fragments with increasing penetration depth. As far as the range of particles (at the same velocity) scales with A/Z^2 (see section 1.2), the lower-Z fragments have longer ranges than the primary ions and, thus, are responsible for the undesired dose behind the Bragg peak, usually called *tail*. In Figure 1.3.2(a), the normalized depth-dose distributions in case of SOBP are showed for proton, carbon and neon ion beams having the same range and the tails are clearly visible for ions.

As shown, the increasing of dose just beyond the peak strongly depends on the mass of the ion: in this specific case, it approximates 15% of dose in the SOBP for ions like carbon and oxygen, while it can reach 30% in case of neon ions. This is one of the reasons why, at least from the physical point of view, it is not justified to use ions heavier than oxygen for a really conformal therapy. Moreover, also biological reasons can be address for the exclusion of very heavy ions, as discussed in the next section. Considering also the percentage of surface dose in the plateau region, carbon ions represent a

good compromise.

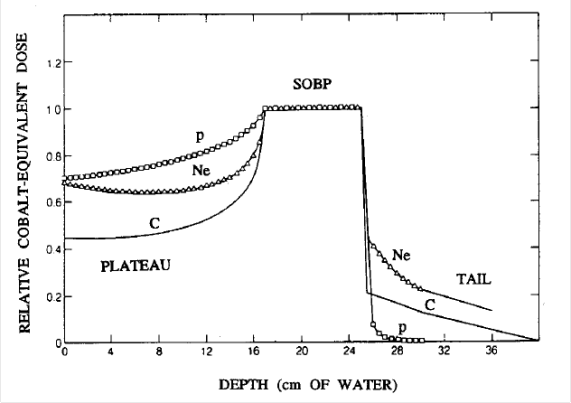

(a)

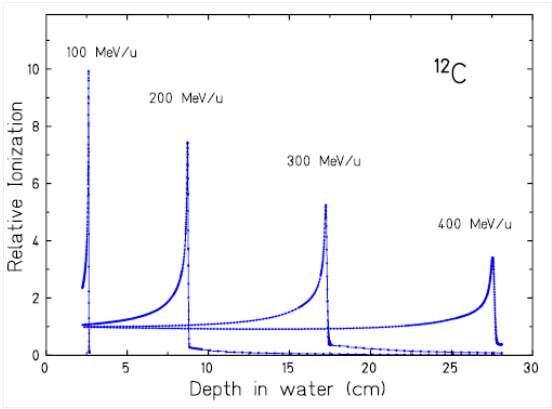

(b)

Figure 1.3.2: (a) Comparison of spread out Bragg peak (SOBP) for proton, carbon and neon beams with the same range in water. Tails due to fragmentation are evident for ion beams and more dramatic for neon ion beams [27]. (b) Measured Bragg curves of ^{12}C ions stopping in water [42].

Nevertheless, the effects of fragmentation have to be carefully taken into account in treatment planning also because of the different biological effects characterizing the secondary particles produced, which give rise to a *mixed radiation field*.

The study of fragmentation of carbon ion beam and the calculation of

the fragments contribution in terms of dose and ionization density is a key point in hadrontherapy and it represents the main concern of the present work.

Indeed, for a volume irradiated by a parallel beam of ions, the absorbed dose D can be expressed as function of the ion fluence Φ and the stopping power ($-dE/dx$) by:

$$D = \frac{\Phi(x)}{\rho}\left(-\frac{dE}{dx}\right), \tag{1.3.1}$$

where ρ is the density of the stopping material. Because of the fragmentation processes, the particle fluence decreases with the penetration distance according to the relation:

$$\Phi(x) = \Phi(0)e^{-\mu x}, \tag{1.3.2}$$

where $\Phi(0)$ is the entrance fluence and μ is the linear attenuation coefficient, proportional to the total microscopic reaction cross-section σ for the ion-tissue interaction [52]. In principle, the dose distribution from each beam could be summed to obtain the total dose distribution. In practical radiotherapy it is not possible, because the absorbed dose must be modified by a radiation weighting factor that is energy dependent and changes according to the ion species considered.

The impact of nuclear fragmentation on carbon ions depth-dose profile is shown in Figure 1.3.2(b). With increasing penetration depth the peak-to-entrance dose ratio becomes gradually smaller, mainly caused by the exponentially diminishing flux of primary ions (see equation 1.3.2). The build-up of lower-Z fragments is clearly visible in the dose tail behind the Bragg peak at larger depths.

The composition of this very complex particle field has to be known for dose optimization in heavy ion therapy, in order to take correctly into account the global biological effect in the tissue, due to secondary as well as primary particles. As an example, measured build-up curves for charged fragments of primary ^{12}C ions with Z=1 to 5 are shown in Figure 1.3.3 [42]. Hydrogen and helium fragments are the most abundantly produced. The heavier fragments like boron are slowed down shortly after the Bragg peak, while hydrogen and helium fragments with much longer ranges produce the longer part of the dose tail.

As far as carbon ion therapy is concern, both nuclear fragmentation cross-sections, as well as algorithms that deal with the transport of charged particle in matter, are essential for accurate treatment planning, as only

roughly 50% of the heavy ions directed to the patient actually reach a deep-seated tumor [53].

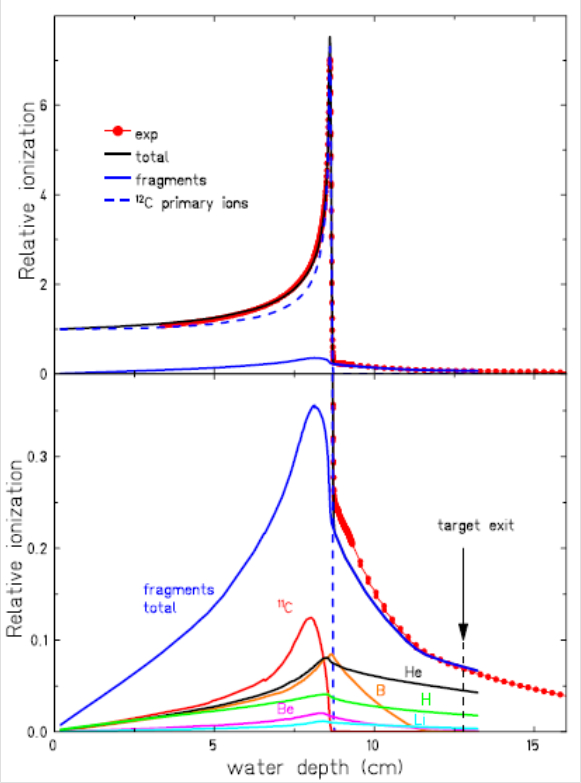

Figure 1.3.3: Top: Measured depth-dose profile of a 200 AMeV ^{12}C ion beam in water is shown with the associated contribution of primary ions and fragments as calculated by the Monte Carlo code PHITS (*Particle and Heavy Ion Transport code System*). Bottom: The magnified ordinate scale shows the contribution of fragments with different atomic numbers Z as calculated with PHITS [42].

Treatment plans actually rely on relatively fast deterministic codes, such as TRiP, developed at GSI [54], [55] or HIBRAC [56], in which theoretical and/or semi-empirical transport models are implemented. The predictive capability of these models in case of mixed radiation fields and complex geometries does not seem adequate for all practical purposes. Reliable tools to overcome the shortcomings of analytical calculations are represented by the Monte Carlo transport codes, such as GEANT4 [57] [58], FLUKA [59]

[60], MCNPX [61] [62], SHIELD/SHIELD-HIT [63] [64] and PHITS [65]. Specifically, the high accuracy ($\leq 3\%$) required for medical treatment planning and sparing of normal tissues surrounding the tumors makes necessary several inter-comparisons of the analytical codes with MC calculations [66] [67].

Concerning the carbon ion therapy, the nuclear reaction models implemented in FLUKA and GEANT4 Monte Carlo codes have been compared with experimental data in some recent studies [68] [69] [70] showing a modest agreement, but these studies are still not sufficient for the intended purposes, since the comparisons were limited to fragments build-up curves and yields. Moreover, in one of the most recent study [67], discrepancies in the order of some tens of percent between Monte Carlo model predictions and experimental data were found. The only way to improve the codes performances is by adjusting the Monte Carlo models on further experimental fragmentation data, which are currently a very limited set.

As a result, the production of light fragments and their angular distribution are still affected by large uncertainties and various codes may differ up to an order of magnitude in their predictions [71]. Similar problems are found in codes used for space radiation transport in shielding materials.

In particular, experimental data are missing, including double-differential cross-sections for carbon ions in the energy range 60-400 AMeV, which are those needed for improving treatment planning in therapy. In this context, the present work aims at filling the gap of information about the fragments build-up and their angular and energy distributions by presenting three carbon fragmentation experiments, characterized by three different combinations of the beam incident energy and the target types and thicknesses.

Regarding the intermediate energy range, measurements of carbon fragmentation at 62 AMeV have been performed on a thin carbon target and on different thick tissue-equivalent targets. For the relativistic energy domain, a measurement of a 400 AMeV carbon beam impinging on a thick carbon target has been performed. Although therapeutic carbon beams have energies of the order of hundreds of AMeV, the primary ions lose their energy passing through the patient's body so that the inelastic nuclear reactions may occur at energies much lower than the incident ones, hence different projectile energy have been investigated.

Moreover, fragmentation measurements performed with thin targets are of particular interest in benchmarking the nuclear interaction codes, since in these measurements the fragmentation of the secondary products and the electromagnetic physics effects in the target are not relevant. On the

other hand, fragmentation measurements on thick tissue-equivalent targets are essential in order to predict the surviving fraction of the primary ions and their contribution to dose after the target. The experiments will be treated in Chapter 2.

From a different point of view, an interesting potential for quality control arises from nuclear fragmentation, which by far compensate for the drawbacks, already discussed. The stripping of one or two neutrons from the ^{12}C projectile yields the positron emitting isotopes ^{11}C and ^{10}C with half-lifes of 20 min and 19 sec (*autoactivation*), respectively. The stopping point of these isotopes can be monitored by measuring the coincident emission of the two annihilation gamma quanta following the β^+ decay. In general, most of the lighter fragments have the same velocity as the primary ions at the collision point [72]. The range of these fragments is given by the formula:

$$R_{fr} = R_{pr}\frac{Z_{pr}^2 M_{fr}}{M_{fr} Z_{fr}^2} \tag{1.3.3}$$

with R being the range, Z the atomic number, M_{fr} and M_{pr} the masses of the fragments and the projectiles, respectively [31]. Hence, the range of carbon isotopes is only slightly shorter than that of the primary particle:

$$R \propto \frac{A}{Z^2} \rightarrow R\left(^{11}C\right) = \frac{11}{12} R\left(^{12}C\right). \tag{1.3.4}$$

Thus, from the measured distribution of the annihilation quanta, the range of the stopping particles can be controlled and compared to the calculated range in the treatment planning, providing an in-situ beam monitoring using Positron Emission Tomography (PET). In fact, it is further expected that the spatial distribution of β^+-activity induced by heavy-ion beams is strongly correlated with the corresponding dose distribution. Even if carbon beams mostly produce ^{11}C and ^{10}C nuclei via projectile fragmentation, also ^{15}O nuclei are produced from the target, with an half-life of 121.8 sec [73].

PET monitoring is of great interest in the hadrontherapy field because provides a direct measurement of the beam distribution inside the patient and it represents as well another great advantage coming from the exploitation of carbon ions in radiotherapy [74] [75]. The calculation of projectile range is, in fact, a critical point in treatment planning because human body is composed of a large variety of materials with different densities (bones, muscles, fat, air-filled cavities, etc).

1.4 Radiobiological rationale of ion beam therapy

1.4.1 Radiation damage by photons and heavy ions

A major advantage of heavy charged particle beams is their increased biological effectiveness compared to photon beams, more precisely in the Bragg peak region and thus in the tumour volume. This increased effectiveness is due to the specific microscopic dose deposition pattern of charged particles. Indeed, a more favourable dose distributions is associated to heavier ions also with respect to protons. Particularly, carbon ions represent the best compromise between local control of the tumour and negative side effects.

In the case of photons irradiation, the energy is transferred to the cell either by photo effect or by Compton effect, depending on the energy of the penetrating photon. Since the cross sections for these processes are rather low, the number of ionization events per incident photon within the volume of a cell is also small. Typically only a few electrons are ejected from target molecules possibly ionizing further molecules if they have received enough energy during their primary interaction. Due to this low number of events, many photons are required to deposit a relevant dose. Since these photons are randomly distributed, the resulting ionization density can be assumed to be homogenous over the entire cell volume thus giving rise to more reparable lesions. As a consequence, photons are referred to as *sparsely ionizing radiation*.

In contrast, the energy spatial distribution associated with ion beams is far more localized, thus resulting in a typically larger biological effect induced by particles, which are usually referred to as *densely ionizing radiation*. Indeed, concerning the biological response to ions irradiation, the track of the particle represents the key information. For an incident charged particle, the ionization occurs along its trajectory and most of the energy loss is transferred to the liberated electrons, which form a sort of "electron cloud" around the path of the primary ion, i.e. the *ion track* [76]. Finally, the action of these electrons determines the biological response together with the primary ionization. It is the higher electron-density, and consequently the ionization-density, that yields a larger biological effectiveness.

More in detail, the formation of a particle track can be regarded as a two-steps process: firstly, electrons are emitted in ion-atom or ion-molecule impact by means of Coulomb interaction of the projectile and the target, and secondly the liberated electrons are transported through the medium by elastic and inelastic collisions. Although the dominant ionization process can be described by the binary-encounter approximation assuming that the

projectile collides with a quasifree electron [30], another source of energetic electrons originates from the *Auger effect*, i.e. the expulsion of outer electrons in the process of filling inner-shell vacancies created by direct Coulomb collisions. A third important interaction mechanism produces the so-called *cusp* electrons. These electrons are either lost or picked up into unbound states of the projectile thus being sharply emitted into forward direction [29].

Interestingly, the ionization cross section of electrons in water exhibits its maximum at about 100 eV, which relates to a mean free path of a few nm. In other words, there is a high probability that two ionization events occur on each of the 2 nm separated, opposite strands of DNA (*deoxyribonucleic acid*). The calculation of track structure is not a trivial task and it has been subject of many publications in which different approaches have been examined. All existing models, analytical [77] or Monte Carlo simulations [78] as well as experimental studies [79], show a steep radially symmetric dose distribution with a negative gradient for an increasing distance r, approximately following a $1/r^2$ dependence. Indeed, most of the induced electrons receive either only a small energy transfer or they are scattered in the forward direction, depositing most of the dose in the center of ion tracks. However, those electrons that are fast enough to leave the track core (δ *rays*) typically undergo a large number of interactions. Due to those frequent scattering processes, the initial preference of electrons in the forward direction diminishes, resulting in a broad angular distribution.

The diameter of a track depends on the range of the electrons and, consequently, on the velocity of the ion. At higher energy the track is wide and the energy loss is low, therefore the ionization events are well separated. With decreasing energy, the track narrows and the energy loss becomes larger. Consequently, the produced damage has a higher local density resulting in a diminished reparability of the lesion and, therefore, an increased biological effect.

The main target of the radiation attack is the DNA inside cells nuclei. DNA is a very complex system and its integrity is essential for cells survival. Therefore DNA is highly protected by an extremely elaborate repair system so that DNA violations like single strand breaks (SSB) or double strand breaks (DSB) are rapidly restored. But when DNA is exposed to very high local doses, where local refers to the scale of a few nanometres, the DNA lesions become concentrated or clustered and repair system fails to correct the damage, as shown in Figure 1.4.1(a).

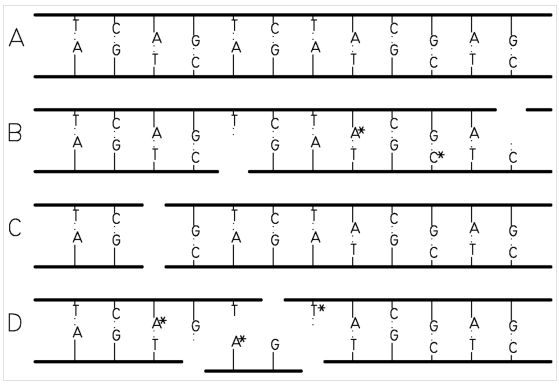

(a)

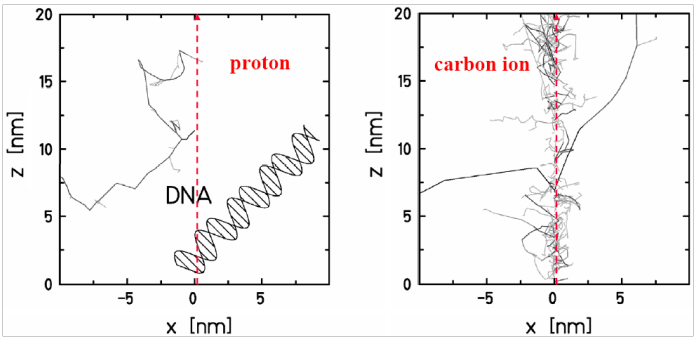

(b)

Figure 1.4.1: (a) Schematic view of an undamaged part of DNA (A), two separated single strand breaks (B), a double strand break (C), and a *clustered lesion* (D). The (*) indicate a base damage. [31]. (b) The structure of a proton and a carbon track in nanometre resolution are compared with a schematic representation of a DNA molecule. The higher density of the secondary electrons, produced by carbon ions, creates a large amount of clustered DNA damage. [80].

From the quantitative point of view, the energy deposition along particles track in tissue is represented by the Linear Energy Transfer (LET), measured in keV/μm and defined as the ratio between the energy dE deposited by a charged particle in a track element and its length dx, considering only single collisions characterized by energy deposition within a specific value Δ:

$$L_\Delta = \left(\frac{dE}{dx}\right)_\Delta . \tag{1.4.1}$$

It is sometimes called also *restricted energy loss* or *restricted* LET. If no limitation in the amount of energy released in any single collision is considered, it is called *unrestricted energy loss* and it is indicated with L_∞.

Charged particle	**Energy(AMeV)**	**LET (keV/μm)**				
$^{M}\mathrm{N}^{Z}$	Range = 262 mm	262	150	70	30	1
$^{1}\mathrm{H}^{+1}$	200.0	0.5	0.6	0.8	1.1	4.8
$^{4}\mathrm{He}^{+2}$	202.0	1.8	2.2	3.1	4.4	20.0
$^{7}\mathrm{Li}^{+3}$	234.3	3.7	4.6	6.2	8.9	40.0
$^{11}\mathrm{B}^{+5}$	329.5	8.5	10.0	13.5	19.0	87.5
$^{12}\mathrm{C}^{+6}$	390.7	11.0	13.5	17.5	24.5	112.0
$^{14}\mathrm{N}^{+7}$	430.5	14.5	17.5	22.5	31.5	142.0
$^{12}\mathrm{O}^{+8}$	468.0	18.0	21.5	28.0	39.0	175.0

Table 1.2: LET values for different ion species at different residual ranges. The energies of column 2 correspond to a range of 26.2 cm in water [80].

Hence, the previous classification of radiations is strictly dependent on LET values: high LET radiations produce more microscopic damages and, thus, they are more biologically effective with respect to low LET radiations. Thus, in a high LET track the damage is extremely localized and consequently referred to as a *clustered lesion* which is, to a large amount, irreparable. Moreover, by considering a specific kind of particle, LET is sensibly variable with penetration depth.

Even if there is not a sharp limit between high and low LET values, for many cell systems the biological effectiveness starts being important if LET is larger than about 20 keV/μm. LET values for light ions are summarized in Table 1.2 for the range corresponding to 200 MeV protons (262 mm of water) [80].

One can see that the LET of carbon ions is larger than 20 keV/μm in the last 40 mm of their range in water, while in the initial part of an approximately 20 cm range in matter (the so called "entrance channel") LET is smaller that 15 keV/μm. Helium shows high LET values only in the last millimetre. For protons, the range of elevated effectiveness is restricted to a few micrometers at the end of the range, which is too small to have a significant clinical impact. For ions heavier than carbon the residual range of elevated LET starts too early and extends to the normal tissues located before the tumour. After the work done at Berkeley with neon and helium ions, in the beginning of the 1990's, carbon ions were chosen as optimal for

the therapy of deep-seated tumours as the increased biological effectiveness, owing to the variation of the LET along the track, could be restricted mainly to the target volume [81].

1.4.2 Relative Biological Effectiveness (RBE)

As far as both physical and biological effects related to a radiation treatment are concerned, the information on LET alone is not adequate, specifically because of the need to evaluate the DNA repair capacity of the cells after irradiation. Indeed, the *Relative Biological Effectiveness* (RBE) is the final parameter to be considered in the optimization of the dose to the patient. Nevertheless, RBE shows complex dependences on absorbed dose, particle energy and atomic number, cell line and survival level and it is defined starting from the biological response for sparsely ionizing radiation, such as X-rays. In this case the biological response, which is quantitatively described by the cell survival S, is a non-linear function of dose and, for doses up to a few Grays, cell inactivation can be parametrized appliying the linear-quadratic (LQ) model [82], thus giving:

$$S\left(D\right) = S_0 e^{-\left(\alpha D + \beta D^2\right)}, \tag{1.4.2}$$

where D is the absorbed dose and α and β are experimentally determined parameters characterizing the radiation response. A plot of survival in a semi-logarithmic scale leads to the characteristic shouldered survival curve, shown in Figure 1.4.2. Particularly, the ratio α/β determines the shoulder of the survival curve and represents a measure of the repair capacity of the biological endpoint. For particle radiation of increasing LET, the β term becomes smaller and the radiation response is given by a pure linear dose relationship.

The figure clearly shows that the same level of survival is reached by a lower deposited dose, and thus to a lower energy released, in case of carbons. This fact experimentally demonstrates the different level of damage produced by sparsely and densely ionizing radiation, respectively, and its relation with LET values. The different action of radiation is quantitatively described in terms of the RBE, which is defined as the ratio of the sparsely ionizing radiation (mostly ^{60}Co rays) and the dose of particles radiation producing the same biological effect (*isoeffect*) [31]:

$$RBE_{iso} = \frac{D_{X-ray}}{D_{particle}}. \tag{1.4.3}$$

As far as RBE refers to the linear-quadratic X-rays dose effect curve, it strongly depends on effect level: it is high for low doses and it decreases with increasing dose. Thus the effect level has to be always given as an index with the RBE level.

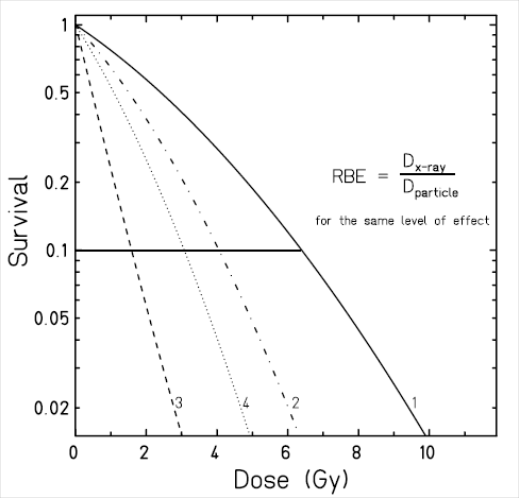

Figure 1.4.2: Survival curves for CHO-K1 cells irradiated with X-rays (1) and carbon ions of different energies: (2) 266.4 AMeV LET = 13.7 keV/μm, (3) 11.0 AMeV LET = 153.0 keV/μm, (4) 2.4 AMeV LET = 482.7 keV/μm [31].

Specifically, considering the ratio between the α-terms, i.e. the initial slopes, of two dose-effect curves, the maximum RBE can be defined, which is usually indicated as RBE_{α}. For comparisons, in literature is also often used the RBE value corresponding to a survival level of 10%, i.e. the RBE_{10}. By definition the RBE for photons equals 1.

Figure 1.4.2 also shows that different energies of the carbon ions yield different dose effect curves. Qualitatively, this can be easily explained: for high energies the track is wide and the LET low, thus the ionization events occur far enough to make repair possible, yielding shouldered curves similar to sparsely ionizing radiation. When energy decreases the diameter of the track shrinks and the LET increases. This leads to a higher ionization density where the ionization events occur closely together with a high possibility of interaction, diminishing the influence of repair and yielding a significantly increased RBE. At very high LET values at the end of the particle range (for carbon ions this is above 200 keV/μm) the local dose density becomes higher than necessary for a lethal damage and RBE decreases again [31]. In

other words in these conditions there is an over production of local damage, which gives rise to the so called *over-kill effect*, resulting also in an effective saturation, while the denominator of equation (1.4.3) continues to increase linearly. This effect is shown in Figure 1.4.3(a) converted into a depth distribution in water.

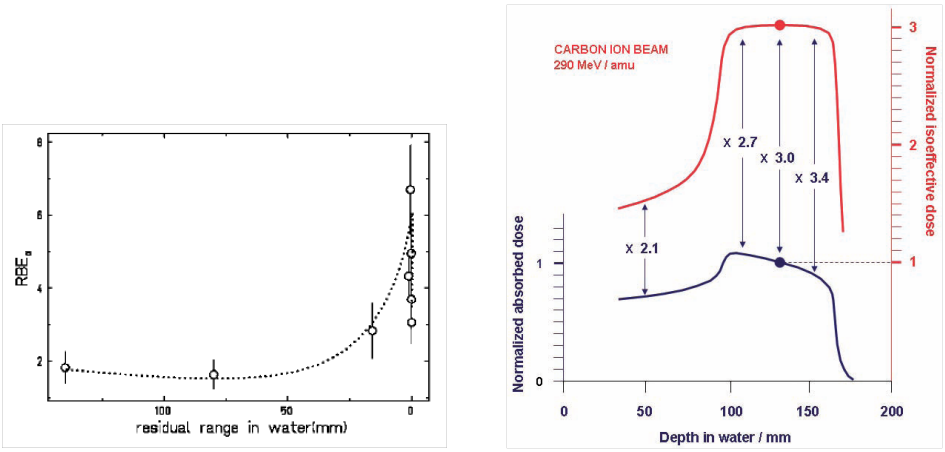

(a) (b)

Figure 1.4.3: (a) RBE$_\alpha$ for carbon irradiated CHO-K1 cells. Data from [83]. (b) Biological dose modeling for carbon ions [3].

For particle therapy the *photon-equivalent dose*, sometimes referred to as *biological effective dose* (BED) or *Gray-equivalent dose*, defined as the product of absorbed dose and RBE, is most significant because it includes the larger efficacy of ions. In Figure 1.4.3(b) one can see that for carbon ions an RBE of 2.1 is calculated in the plateau region, while its values vary between 2.7 and 3.4 in the SOBP region, with a maximum RBE value in the distal part. As a consequence and in order to produce a homogeneous BED in the target, the physical dose calculated in the SOBP region is not flat, but decresases with increasing depth.

According to what has been previously discussed it could be possible to summarize that ions heavier than carbon could achieve the same biological effects or even enhanced. That is in part true but high RBE characterizing a specific radiation is not enough to say that it will be suitable for therapy because, as already stated before, what is crucial is the compromise

between sterilization of the tumour and damage to the surrounding healthy tissues. Hence, the impact of the enhanced RBE on tumour killing is higher when the RBE maximum overlaps sufficiently with the Bragg maximum, thus getting together both effects of dose and high RBE but, at the same time, minimizing the biological effects before the peak.

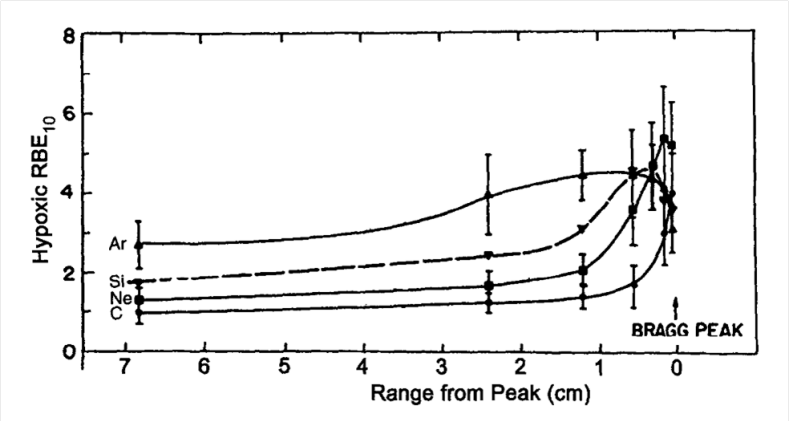

Figure 1.4.4: RBE for C, Ne, Si and Ar ions as function of the penetration depth. For carbon ions RBE is relatively low at the entrance and becomes higher closeness the peak. [76].

For carbon this condition is well satisfied, in fact the strongly elevated RBE region is restricted to the end of the particle range, where RBE has values ranging from 2 to 5, while in the entrance channel it is about 1, which means that reparable DNA damage predominates. In Figure 1.4.3(a) this behaviour is clearly shown but it is demonstrated unambiguously if comparisons with other heavier ions are taken into account. Indeed, for ions like neon, silicon and argon the irreparable damage becomes important in the entrance channel, too (see Figure 1.4.4). This is one of the reasons why carbon ions have been considered as the most suitable for hadrontherapy also from the biological point of view and chosen from the beginning of 1990's as optimal for treating deep-seated tumours.

Nevertheless, because RBE depends also on the possibility to repair the damage produced in the DNA, the repair capacity of the irradiated tissues becomes relevant. In this contest, the treatment of hypoxic tumors poses a specific challenge. When tumors are growing in size, new blood vessels need to be generated to supply oxygen to the cells in the tumor core. Often

these vessels are not generated fast enough or they might also be of minor quality. Those effects of poor angiogenesis result in a lower oxygen level as compared to healthy cells. Especially in the center of large tumors, hypoxic regions occur frequently. It is known that these hypoxic conditions lead to a larger radioresistance, however, a widely accepted mechanistic explanation for this effect is still missing. The oxygen effect is quantified by the *Oxygen Enhancement Ratio* (OER) given by:

$$OER = \frac{D_{hypoxic}}{D_{aerobic}}, \tag{1.4.4}$$

where $D_{hypoxic}$ and $D_{aerobic}$ are the doses with reduced and normal oxygen supply, respectively, resulting in the same biological or clinical effect [29]. In contrast with RBE, the OER is a dose-modifying factor and independent of dose. Typically, it is about 3 for conventional radiation, whereas it is significantly reduced for ion irradiation. Figure 1.4.5 shows the results of cell survival studies carried out at LBL in the 1970's as a preparation for the first heavy-ion treatments [84].

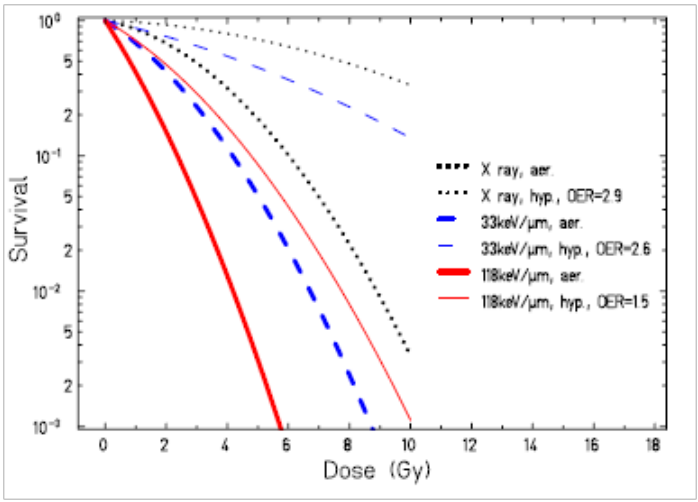

Figure 1.4.5: Influence of the oxygen level on cell survival of human kidney T-1 cells for carbon ions with different LET. Lines are based on experimental data by [84].

The difference between hypoxic and normoxic cells is reduced for high-LET particles and the survival curves converge. The OER decreases with

decreasing particle energy, and for high-LET particles it is close to 1. This behavior is in line with the general observation that cell line-specific differences diminish after ion irradiation. In numerous other cell experiments during the last decades, this behavior was validated for a large range of ions and cell lineages [85]. It was found that the minimum OER is lower for heavier ions such as carbon or neon than for light ions (e.g. helium). Supposedly, the potential higher radiation damage of ions by direct hits compared to indirect radical-induced hits reduces the oxygen effect. Along with a reduction of the OER, the RBE is further enhanced in the SOBP. Therefore, heavy particles such as carbon ions offer enormous potential for curing tumors with hypoxic regions.

In contrast to proton therapy, where the low LET of protons is believed to allow the application of a single factor (RBE = 1.1) throughout the entire radiation field [86], the situation in heavy-ion therapy is much more complex because of the large variations of LET. As already mentioned, the mixed radiation field of carbon ions SOBP is made of, not only the primaries with a large energy spread, but also the lighter fragments. Moreover, the levels of absorbed dose can vary largely within single fractions and between different tumor sites. Thus, it's mandatory to analize the dependence of the cellular systems response on the energy or LET of the penetrating particle. In Figure 1.4.6(a) a compilation of different cell survival experiments with V79 hamster cells, a frequently used cell line in radiobiology laboratories, reveals that the RBE increases with LET up to an ion-dependent maximum value and decreases for higher LET values [87] [88].

According to the higher ionization density in the track center of particles with a larger LET, the radiation damage is more severe, thus increasing the RBE. However, at a certain LET value the dose deposition is so large that a single-particle traversal sufficiently reduces the cell survival probability. In that case, the additional dose deposited by ions with a larger LET is wasted and we would not expect a larger RBE, because of the over-kill effect previously discussed.

Moreover, the particle type influences the position of the RBE maximum (see Figure 1.4.6(a)). As a result, for heavier particles the maximum is typically shifted to higher LET values. Indeed, at the LET value corresponding to the RBE maximum for protons, carbon ions are much faster than protons (see equation 1.2.2) resulting in broader tracks with a reduced ionization density in the track center. Therefore, at the same LET the biological damage and thus the cell killing effect of carbon ions is smaller than for protons. In order to achieve the maximum RBE, slower ions with a cor-

respondingly smaller track size and higher LET are required.

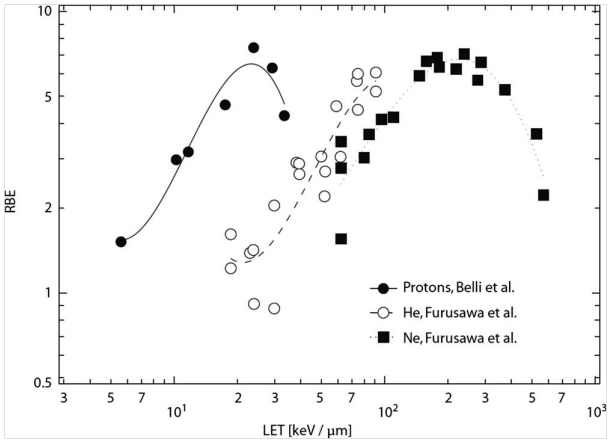

(a)

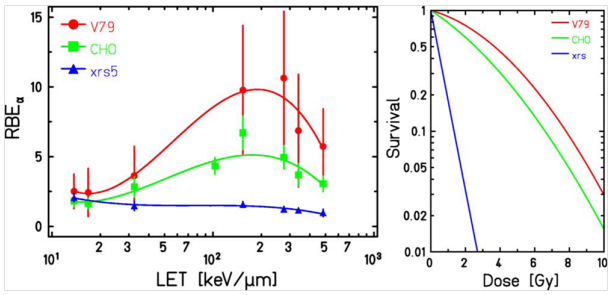

(b)

Figure 1.4.6: (a) Dependence of $\mathrm{RBE}_\alpha = \alpha_{ion}/\alpha$ on LET and particle type, where α and α_{ion} are the linear part of the survival curve for photons and ions, respectively. Data are redrawn from [87] and [88]. From [89] (b) RBE dependence on the radiation sensitivity of cell lines. Left: Dependence of initial RBE on the three cell lines CHO, V79, and XRS after carbon irradiation. Right: Survival curves of the same cell lines demonstrate the different radiosensitivities after X-rays irradiation. Experimental data are from [83].

Finally, the radiosensitivity of the irradiated cell line or tissue also determines the RBE [83], as shown in Figure 1.4.6(b) where a comparison of three mammalian cell lines with different radiosensitivities is reported. The RBE for carbon irradiation is highest for the V79 cell line, which is most resistant to conventional irradiation. Chinese hamster ovary CHO cells are

more sensitive to photon radiation and show a moderate RBE, whereas for the repair-deficient CHO-mutant XRS cell line, the increased effectiveness of ions is almost negligible. In general, the difference in radiosensitivity is largely reduced for high-LET irradiation. In order to investigate the radiosensitivity of human cell lines to therapeutic carbon ions, the survival curves for more than a dozen lineages of normal and tumor cells has been determined [90].

These considerations on the RBE dependences, based on a large number of measurements done over many years, imply that in order to take into account biological effects, beyond the physical dose, the spatial distribution of LET, energy and fluence of all the particles has to be known. This is mandatory in case of *mixed radiation fields*, as for carbon ion treatments, where LET and energies of primary particles as well as of secondaries have to be considered for an accurate treatment planning.

1.5 Carbon ion therapy highlights

As a result of what discussed in the previous sections, carbon ions are advantageous in radiotherapy because of four physical and biological properties [80]:

1. Carbon ions deposit their maximum energy density in the Bragg peak at the end of their range, where they can produce severe damage to the cells while sparing both the transversely adjacent and deeper located healthy tissues.

2. Beams of carbon ions can easily be formed as narrow focused and scanning pencil beams of variable penetration depth, so that any part of a tumour can be accurately irradiated with optimal precision. They penetrate the patient with minor lateral scattering and longitudinal straggling. Indeed, lateral and longitudinal scattering is about 3 times smaller than for protons.

3. Carbon beams have a favourable depth profile of the RBE. This is the main advantage with respect to protons: at high energies, in the entrance channel mostly repairable damages are produced, corresponding to low RBE values, while in the last 2-3 cm of the range the RBE significantly increases to values between 2 and 5, depending on the type of tumour. Moreover very radio-resistant tumours show the largest increase in RBE.

4. The location where the dose is deposited by carbon ions can be determined by means of on-line PET. The on-line PET control permits exploitation of the millimetre precision of a focused carbon beam, with its high biological effectiveness for targets that are close to or inside a critical structure.

The most advanced photon treatment plan using IMRT with 9 fields is compared with a two-field carbon treatment plan, as shown in Figure 1.4.7. In this case, and in most others, the advantage of the carbons inverse dose profile, with the high dose and high LET at the end of the range, allows reducing the dose to the normal tissues outside the target volume by a factor of 2-3. This applies also to protons, yet carbon ions are more effective for radio-resistant tumours.

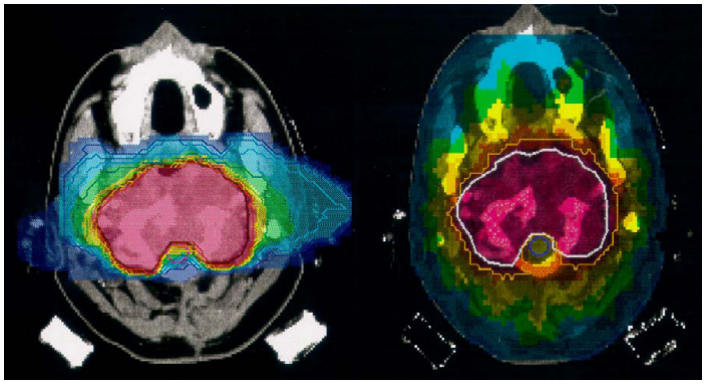

Figure 1.5.1: Comparison of treatment plans with 2 fields of carbon ion (left panel) with 9 fields of X-rays. In both cases the conformity to the target volume is good but for carbon ions the dose to the normal tissues is much smaller. [91].

1.6 Treatment planning for ion beam therapy: the INFN TPS project

In order to fully exploit the attractive potentialities of ions treatment it is necessary to arrange for an algorithm able to make up all the key parameters, physical as well as biological ones, which are necessary to optimize the dose distribution.

This delicate aim should be carried out by the Treatment Planning System (TPS). The TPS is a set of tools that allows the translation of the dose

prescription into a set of beam energies, positions and intensities needed for the treatment. Innovative contributions in this field are particularly needed in case of ions projectiles.

The first step of treatment planning for any radiation therapy modality is to define and delineate the target volume. Exploiting the modern imaging techniques, a 3D model of the treatment geometry is constructed, which is used to find suitable beam entrance ports under the condition that the traversal of critical structures should be avoided. For protons and heavier ions only few entrance ports (typically 2 nearly opposing fields) are necessary in most cases because of their superior depth-dose characteristics. Particularly, the task of the treatment planner is to determine the appropriate particle energies, positions and fluences in order to achieve the prescribed dose in a given target volume.

In the next step the RBE must be included iteratively for each irradiation point. While for protons the optimization is commonly restricted to absorbed dose only, as a constant RBE value of 1.0-1.1 is applied [86], for ion-beam therapy the biological effective dose estimate is a difficult task, in view of the manifold dependencies of RBE and the complex radiation field.

At GSI the novel treatment planning system TRiP (TReatment planning for Particles) [91] [92] has been developed aiming to find an optimum superposition of a large number of pencil beams (tipically several ten thousands) with individual energy, position, and particle number, in order to achieve the prescribed dose (*inverse planning*). TRiP includes a physical model to describe depth dose profiles and nuclear fragmentation of pencil beams of ^{12}C ions, and it also includes the radiobiological model LEM (Local Effect Model), which allows the calculation of the biologically effective dose, RBE and cell survival (or other biological endpoints[5]) for any dose level and radiation field composition, provided the photon sensitivity for the tissue under consideration is known.

A project has been carrying out by the INFN (Istituto Nazionale di Fisica Nucleare) with the aim of the design of a new advanced Treatment Planning System for ion therapy with active beam scanning, with a particular attention to carbon ion beams. This project put together different competencies with the scope of giving rise to an innovative tool to be used for ion beams therapy, as discussed in the next section.

In the hadrontherapy field, INFN has been directly involved for more than 20 years. Successful examples of cooperation between INFN, radio-

[5]A clinical endpoint is an observed or measured outcome in a clinical trial to indicate or reflect the effect of the treatment being tested.

therapists and oncologists have been accomplished. In this framework, the development of the CATANA (Centro di Adroterapia e Applicazioni Nucleari Avanzate) facility at the Laboratori Nazionali del Sud (LNS) of INFN in Catania, for the treatment of ocular melanoma by means of a proton beam, has been an example of particular significance as far as more than three hundreds of patients have already been successfully treated [22]. At present INFN is also deeply involved in the first clinical trials of the newly designed synchrotron for protons and ^{12}C ions CNAO (Centro Nazionale di Adroterapia Oncologica), built in Pavia (Italy) and based on active beam scanning technology [93].

Starting from these experiences, several INFN research groups, active in different scientific areas (experimental and theoretical nuclear physics, Monte Carlo calculations and techniques for numerical analysis, radiobiology and hardware/software development for dose monitoring purposes), proposed to cooperate in order to develop an improved Treatment Planning System for ion therapy with active scanning [94].

Particularly, in case of Intensity Modulated Particle Therapy (IMPT) irradiation technique, many thousands, individually weighted, narrow beams are delivered to the patient using several fields (beam directions) in order to deliver a uniform dose to an arbitrary shaped planning target volume (PTV). Due to the very large number of degrees of freedom, computer-aided *inverse planning* techniques are mandatory to create reliable IMPT treatment plans. Within these techniques, beam spot positions, energies and particle fluences are determined from the prescribed dose distribution by means of an optimization procedure over an appropriate *objective function.* The optimization has to be performed in order to have a TPS able to compute the dose delivered to the patient with the highest probability of eradicating all the clonogenic tumour cells (sparing the healthy tissues) and, at the same time, able to evaluate the treatment plan in real time and with a high level of interactivity. Thus, the TPS project, approved by INFN, consists in the development of the optimization techniques by facing two different aspects.

Indeed the research activities are classified into two main streams: first, to improve the knowledge on the biological effects of radiation by effectively including various physical, biological and other factors into the objective function; second, to evaluate and minimize the objective function, within the hardware constraints (computation time, memory management) by developing different mathematical methods and algorithms.

As discussed in the previous sections, RBE depends non-linearly on sev-

eral factors and, in case of ion beams, these relationships are more and more complex. Nevertheless, the biological effectiveness of primary ions as a function of depth in the irradiated tissues has to be evaluated carefully by taking also into account the effects due to all the secondary fragments produced in nuclear reactions within the irradiated volume. In general, the exposure to ion beams will result in a superposition of different radiation fields.

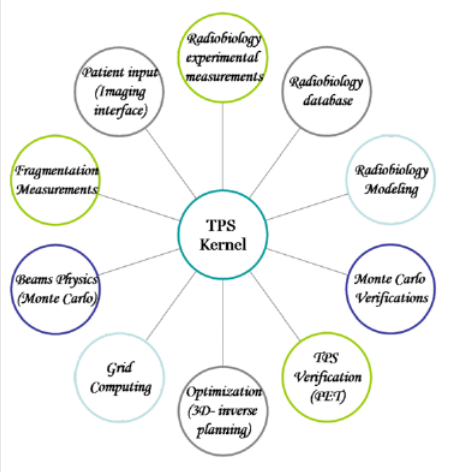

Figure 1.6.1: The INFN TPS research areas [94] [95].

Considering the state of art (TRiP developed at GSI), the INFN TPS projects has been proposed with the aim of achieving substantial improvements by putting forward innovative solutions for different open issues. Some of them are: the multi-field optimization, improvement of physical models for fragmentation (trying to cover the lack of experimental data for carbon ion fragmentation between 20 e 400 AMeV), simulation tool to verify the implemented TPS (Monte Carlo simulation for independent verifications of the TPS output), techniques for on-line monitoring of the dose delivered (PET on-line techniques), factorization of the RBE computation from the cell type (improvements of the existing radiobiological models), inclusion of 4D treatment for moving target optimization (movements affecting some organs, i.e. breathing movements of lung), water equivalent approximation (different density gradients contribution), optimization of the field definition (search of the best field angle) and finally factorization of the dependence of the TPS on the accelerator and beam control system. A schematic represen-

tation of the main research areas, in which each group of the collaboration will give its own contribution, are reported in Figure 1.5.1 [94] [95].

The work carried out in this Ph.D. thesis has been undertaken in the context of the INFN TPS project. At LNS, measurements of projectile fragmentation of carbon ion beams at 62 AMeV on thin and thick targets have been performed and the experimental fragmentation cross sections has been compared with those obtained with the GEANT4 (GEometry ANd Tracking) Monte Carlo code. Within the collaboration framework, a third experiment has been set-up at GSI in order to investigate also fragmentation cross sections in the relativistic energy range, in order to improve nuclear physics models within the Monte Carlo codes, embedded in the TPS.

1.7 Hadrontherapy in the world

Nowadays 38 hadrontherapy facilities are in operation all around the world: Europe (11 centers distributed in Italy, France, Germany, England, Switzerland, Sweden, Poland, Russia), Asia (8 centers in Japan, 2 in China, 1 in South Corea), America (11 centers in USA and 1 in Canada) and South Africa (1 centre). Figure 1.6.1 shows in detail the locations of each facility [96]. Most centers are proton facilities using cyclotron technology with *passive beam delivery system.*

Indeed, there are essentially two techniques to shape beam distribution on the tumor target: *passive and active beam delivery.* The passive delivery consists in putting before the patient several absorbers able to change beam characteristics. The passive technique consists of: a *scatterer* to enlarge the beam; a variable *degrader* and a *ridge filter* to increase energy spread creating a SOBP; a first collimator to select the central part of the beam; the so called *bolus*, a device with a "hole" that has the shape of the distal surface of the tumour; a final *multileaf collimator* that gives the beam the required transverse size.

Some variants to this scheme are the use of a rotating wheel range modulator as variable degrader and the *wobbling method.* The rotating wheel allows to change the thickness of material the beam passes through: in this way, making rotate the wheel, beams with different energies are obtained resulting in a SOBP. The wobbling method is based on the use of scanning magnets that cause the beam moves on a circle at high frequency before the scatterer so resulting in a flat beam to be adjusted transversally and longitudinally. There are some evident disadvantages of the passive method. The main drawback of passive beam shaping is related with the presence

Figure 1.7.1: Locations of the operative hadrontherapy facilities all around the world [96].

of lots of materials between the beam and the patient which cause nuclear fragmentation leading to dose tails after the Bragg peak.

In the active scanning method two magnets are used to move the beam in the two orthogonal directions. The tumour is virtually divided in slices in the longitudinal direction and each slices is thought as composed of small volumes called *voxels* (or *spots*). Each slice is irradiated fixing the beam energy and irradiating each voxel changing the currents of the scanning magnets. Furthermore, for each voxel in a slice it can be taken into account the dose given during the irradiation of the previous slices. Therefore with active scanning the irradiated target is shaped very closely to the tumour target, both in the transverse and in the longitudinal planes. The drawback of such beam delivery system is a greater difficulty in operation due to the management of the scanning magnets and of the beam position and also an increased sensitivity of the system to current ripples and changes.

Problems occur in the cases in which tumour moves because of breathing and heart beating. In this case the passive scanning appears to be the easier solution; anyway considering the superiority of the active method, several studies are in progress worldwide in order to develop methods that allow

to use the active scanning also with moving tumours. Active scanning was first used in Japan in 1980 [97] and then optimized and regularly used for treatments at PSI [98], GSI [99], HIT and CNAO [100].

A purely active scanning method, i.e. without absorbers, is possible only with a synchrotron because of the need of a variable extraction energy. Indeed the energy from a cyclotron is fixed and the active scanning is possible only after having changed the beam energy like in the passive methods with a wedge degrader.

In addition to the hadrontherapy centers already in operation, other 17 facilities are under construction or will start treatments in the next years in Europe, Asia and USA. Presently carbon ions are produced in Asia at HIMAC, GHC, PATRO and IMP, in Europe at HIT and CNAO. A particular mention is due to HIMAC centre [25] equipped with two synchrotrons and operating since 1994, it is producing the most important clinical results with carbon ions with more than 6600 treated patients.

Finally, in Figure 1.6.2 the last report of the total amount of patients treated all over the world until the end of the 2012, with both protons and carbon ions, is shown [101].

WHERE		PARTICLE	FIRST PATIENT	PATIENT TOTAL	DATE OF TOTAL	
Canada	Vancouver (TRIUMF)	p	1995	170	Dec-12	ocular tumors only
Czech Rep.	Prag (PTCCZ)	p	2012	1	Dec-12	
China	Wanjie (WPTC)	p	2004	1078	Dec-12	
China	Lanzhou	C ion	2006	194	Dec-12	
England	Clatterbridge	p	1989	2297	Dec-12	ocular tumors only
France	Nice (CAL)	p	1991	4692	Dec-12	ocular tumors only
France	Orsay (CPO)	p	1991	5949	Dec-12	4748 ocular tumors
Germany	Berlin (HMI)	p	1998	2084	Dec-12	ocular tumors only
Germany	Munich (RPTC)	p	2009	1377	Dec-12	
Germany	HIT, Heidelberg	C ion	2010	980	Dec-12	
Germany	HIT, Heidelberg	p	2010	252	Dec-12	
Italy	Catania (INFN-LNS)	p	2002	293	Nov-12	ocular tumors only
Italy	Pavia (CNAO)	p	2011	42	Dec-12	
Italy	Pavia (CNAO)	C ion	2012	3	Dec-12	
Japan	Chiba (HIMAC)	C ion	1994	7331	Jan-13	72 with scanning
Japan	Kashiwa (NCC)	p	1998	1226	Mar-13	
Japan	Hyogo (HIBMC)	p	2001	3198	Dec-11	
Japan	Hyogo (HIBMC)	C ion	2002	1271	Dec-11	
Japan	Tsukuba (PMRC, 2)	p	2001	2516	Dec-12	
Japan	Shizuoka	p	2003	1365	Dec-12	
Japan	Koriyama-City	p	2008	1812	Dec-12	
Japan	Gunma	C ion	2010	537	Dec-12	
Japan	Ibusuki (MMRI)	p	2011	490	Dec-12	
Korea	Ilsan, Seoul	p	2007	1041	Dec-12	
Poland	Krakow	p	2011	15	Dec-12	ocular tumors only
Russia	Moscow (ITEP)	p	1969	4300	Dec-12	estimated
Russia	St. Petersburg	p	1975	1386	Dec-12	
Russia	Dubna (JINR, 2)	p	1999	922	Dec-12	
South Africa	iThemba LABS	p	1993	521	Dec-11	
Sweden	Uppsala (2)	p	1989	1267	Dec-12	
Switzerland	Villigen-PSI, incl OPTIS2	p	1996	1409	Dec-12	498 ocular tumors
USA, CA.	UCSF - CNL	p	1994	1515	Dec-12	ocular tumors only
USA, CA.	Loma Linda (LLUMC)	p	1990	16884	Dec-12	
USA, IN.	Bloomington (IU Health PTC)	p	2004	1688	Dec-12	
USA, MA.	Boston (NPTC)	p	2001	6550	Oct-12	
USA, TX.	Houston (MD Anderson)	p	2006	3909	Dec-12	
USA, FL	Jacksonville (UFPTI)	p	2006	4272	Dec-12	
USA, OK.	Oklahoma City (ProCure PTC)	p	2009	1045	Dec-12	
USA, PA.	Philadelphia (UPenn)	p	2010	1100	Dec-12	
USA, NY.	New Jersey ProCure PTC)	p	2012	137	Dec-12	
USA, IL.	CDH Warrenville	p	2010	840	Dec-12	
USA, VA.	Hampton (HUPTI)	p	2010	489	Dec-12	
				88448	**Total**	
			thereof	10316	C-ions	
				78132	protons	

Figure 1.7.2: Patients statistics for facilities in operation until the end of 2012 [101].

Chapter 2

The Experiments

In the following the experimental apparata used in three different experiments done at LNS (Catania, Italy) and GSI (Darmstadt, Germany) will be described.

The two measurements done at LNS were dedicated to the study of carbon fragmentation at Fermi[1] energies on both thin and thick carbon targets, while the one performed at the GSI laboratory was devoted to carbon fragmentation at relativistic energy using a thicker carbon target.

The common goal was to estimate the angular distribution of the emitted fragments and the absolute differential cross section. Different energies of the incident beam and various kind of targets were chosen in order to fill the lack of accurate data in the energy range of interest for hadrontherapy.

2.1 Fragmentation at Fermi energies on a thin target

An extensive campaign of carbon fragmentation measurements has been recently started at the Laboratori Nazionali del Sud (INFN) in Catania. In particular, the FRAG[2] experiment was performed using a ^{12}C beam delivered by the Superconducting Cyclotron (CS) at 62 AMeV. Inside the scattering chamber, located in the 20° experimental cave, a ^{12}C (104 μg/cm^2) target was bombarded.

The reaction products were detected by a system of detector telescopes (described in the next section) and identified by the ΔE-E$_{res}$ technique.

[1]The Fermi energy is the energy of the highest occupied single-particle state, in a quantum system of non-interacting fermions at absolute zero temperature.

[2]FRAGmentation for basic science and application research.

The absolute cross sections were determined from the measured fragments yields, corrected for the dead-time of the acquisition system, the known target thickness and the beam current, measured by a Faraday cup. In Figure 2.1.1 a schematic layout of the experimental set-up is shown.

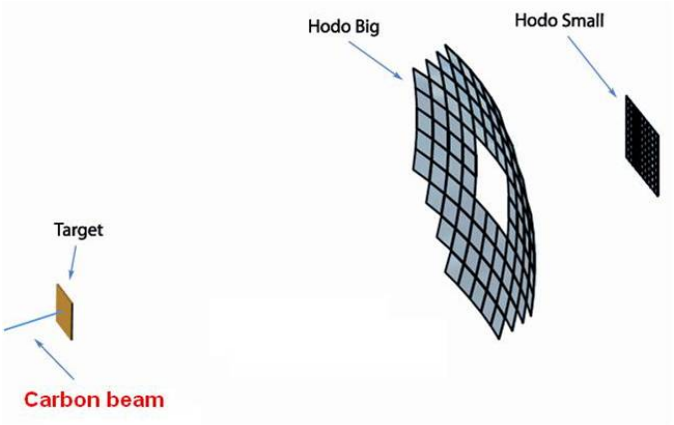

Figure 2.1.1: A schematic view of the FRAG experimental set-up at LNS.

2.1.1 Experimental apparatus

The FRAG detection set-up was conceived in order to distinguish particles in term of atomic Z and mass number A, with a good energy resolution and high efficiency at forward angles.

In particular, it consisted of two Si-CsI hodoscopes of two-fold and three-fold telescope detectors with different granularity, called Hodo-Small and Hodo-Big, placed at a distance of 80 cm and 60 cm from the target [102], respectively (see Figure 2.1.1).
Each element of the Hodo-Small consists of a 300 μm thick silicon (ΔE) detector, 1×1 cm^2 active area, followed by a 1×1 cm^2, 10 cm long CsI(Tl)[3] crystal (E) detector, coupled to a photodiode read-out. The Hodo-Small detectors were arranged in a cube of 81 telescopes, covering the angular region $2.2° \leq \vartheta_{lab} \leq 5.5°$ (see Figure 2.1.2, right).

Each module of the Hodo-Big was a three-fold telescope consisting of a 50 μm thick silicon (ΔE_1) detector followed by a 300 μm thick silicon (ΔE_2) detector and a 6 cm long CsI(Tl) scintillator, for the residual energy (E_{res})

[3]Cesium Iodide crystal (CsI) doped with Tallium (Tl).

measurement, coupled to a photodiode read-out. Each element has an active area of 3×3 cm^2.

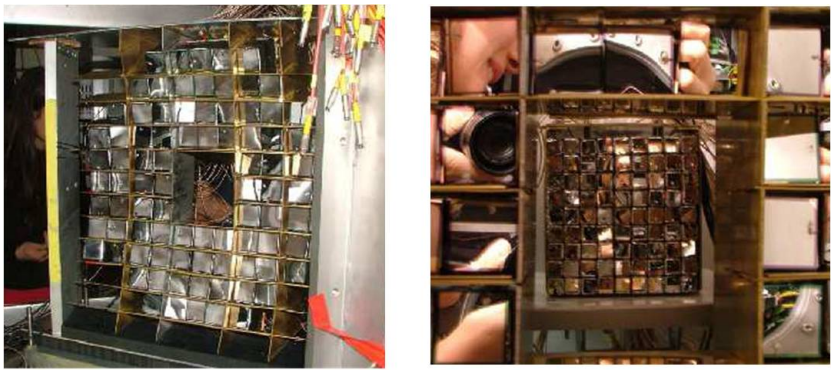

Figure 2.1.2: Left: the 88 modules of the Hodo-Big. Right: the Hodo-Small detectors arranged in a cube of 81 telescopes.

The 88 modules of the Hodo-Big are arranged on a spherical surface of radius r = 60 cm centered on the target position, covering the angular region $7.6° \leq \vartheta_{lab} \leq 21.8°$ (see Figure 2.1.2, left). The two hodoscopes cover a solide angle of 0.34 sr with a geometrical efficiency of 72%. In Figure 2.1.3, one of the Hodo-Big telescopes is shown. In order to maximize the packing, there is no housing around the scintillators and the ΔE detectors are self-supporting silicon chips.

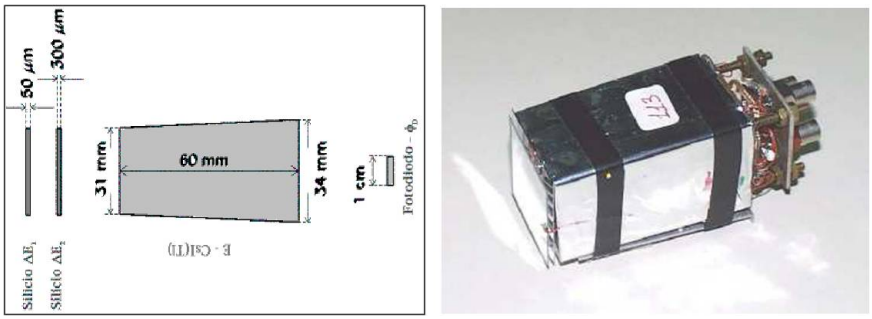

Figure 2.1.3: Schematic representation (left) and image (right) of a telescope of the Hodo-Big.

The CsI(Tl) scintillator was chosen because of the advantages it exhibits with respect to other possible candidates. It is only slightly hygroscopic,

so that hermetic sealing is not needed. Moreover it has good mechanical properties, so that it can hold mechanical shocks fairly well and can be easily machined. Its high density (4.51 g/cm^3) makes this scintillator material suitable to stop ions, in the energy range of interest, in few centimeters. Furthermore, the light emission spectrum fits well with the response curve of silicon photodiodes, being the quantum efficiency around 70% at 550 nm.

Disadvantages are represented by the scintillation quenching effect and by the dependence of the light emission on the charge, mass and energy of the particle detected, which implies a specific calibration procedure for each ion. The Hodo-Big CsI(Tl) crystals have been accurately cut in a pyramid-trunk shape (31×31 mm^2 and 34×34 mm^2, see Figure 2.1.3) in order to be centered at the same distance (60 cm) with respect to the target position, so that each of them subtends an equal solid angle of 2.8 msr.

On the other hand, the Hodo-Small CsI(Tl) scintillators are simply packed one over the other because of the telescopes small angular aperture with respect to their distance from the target. Indeed, this ensures that they are all placed at around the same position, within mechanical errors. The back side of the CsI scintillator is polished to be optically coupled to the photodiode. To eliminate optical cross talk between detectors, each module is wrapped with 0.1 mm millipore strips, covered by two teflon layers (0.5 mm thick) and coated by 0.2 mm thick aluminium foil, which acts as reflector and optical separator between adjacent modules. By covering the front side of the scintillator with an aluminized mylar 2 μm thick foil, a uniform light collection efficiency is achieved.

Photodiode (ϕ_D) were chosen because of various advantages. They are compact and have a good quantum efficiency for the CsI(Tl) light emission spectrum. Moreover they have a good gain stability and require low bias voltages. On the other hand, the output signals are small, compared to signals from a photomultiplier, thus requiring a careful signal processing to optimize energy resolution. The optical coupling is obtained using a two-component siliconic glue which has a good transmission in the wavelength of interest. The photodiode is typically 250 μm thick with an active area of 1×1 cm^2 (see Figure 2.1.3) and 0.6×0.6 cm^2 for the Hodo-Big and Hodo-Small telescopes respectively.

Signals coming from both the silicon detectors and the photodiodes ϕ_D are driven at the input of charge preamplifiers mounted as near as possible to the detectors, inside the vacuum chamber, thus keeping low capacities due to signal transmission. A PA sensitivity of 1 mV/MeV is used for the silicon signals while a 45 mV/MeV is used for the ϕ_D signals. They are

power-supplied in groups of eight, with one common test-pulse input and bias supply for each group through a motherboard housing up to 96 elements.

Preamplifiers signals are read out by shaping amplifiers which gives, from each channel, an analog output in a lemo connector and Leading Edge (L.E.) and Zero Crossing (Z.C.) logic signals.

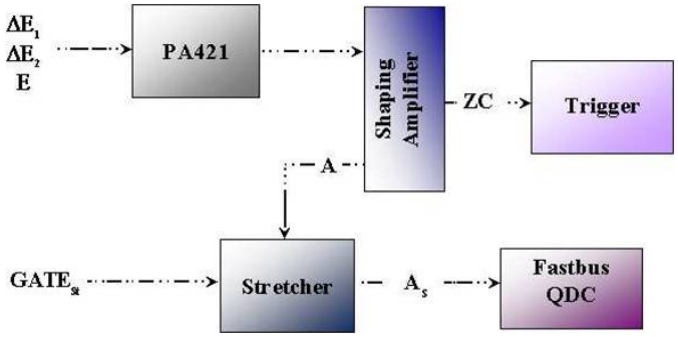

Figure 2.1.4: Block diagram of the electronics associated to each telescope of the Hodo-Big.

Shaping time of 1.0 and 3.0 μsec have been used for the Si and CsI detectors respectively. As can be seen in Figure 2.1.4, the analog outputs shaped by the amplifiers are then stretched at their maxima values for a time defined by a common gate, derived from the trigger, and then digitised by a 96-channel LeCroy Fastbus-QDC with a common gate, also derived from the trigger. Since this signal is common to all the QDC channels, the stretchers allow both the conversion and the integration of each signal on its maximum. The stretchers are controlled by two logic NIM signals for all the 96 channels. The first one (Start) allows to accept incoming signals, while the second one (GATE_{Str}) controls the time extent. These modules accept negative polarity input signals with a frequency below 63.3 kHz and amplitude between 8 mV and 8 V. During the experiment, the GATE_{Str} was delayed of 180 nsec with respect to the incoming signals, and its time width was set to 20 μsec.

The Fastbus-QDC backplane includes a 32-bit wide data bus, used both for data and for addressing. The ADC 1885F LeCroy was used for the analog signals conversion. This model contains 96 channels of analog-to-digital converter (QDC) with current integrating negative inputs. It offers

the equivalent dynamic range of a 15-bit ADC in its 12-bit data using a bi-linear technique.

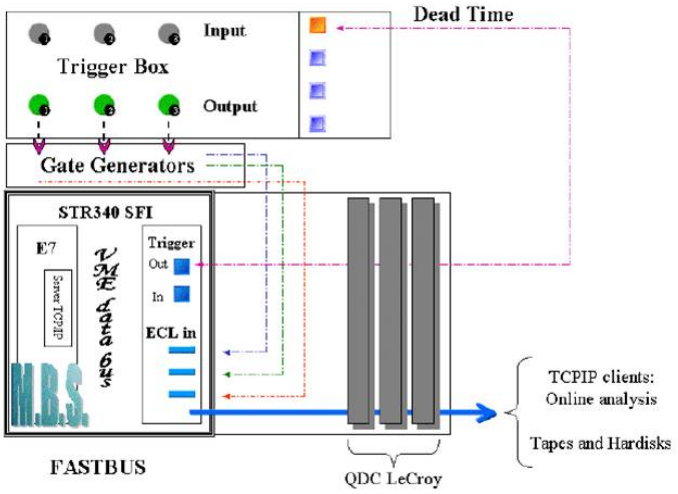

Figure 2.1.5: Schematic view of the data acquisition system used.

In order to cover a wide dynamic range with a single 12-bit ADC, a dual range technique was used. For input less than 175 pC the signal is digitized with a resolution of 50 fC/count (Low Range). For signals between 175 and 1450 pC the resolution is 400 fC/count (High Range). The digitized output from each channel consists of a 12-bit amplitude word and a range bit (13th bit). Accordingly, both small and large amplitude signals are digitized with the same 4096 channels resolution, thus obtaining a magnifying effect of the low range which, otherwise, would be compressed.

The Fastbus-QDC is handled by the SFI (Struck Fastbus Interface) module, based on a standard VME bus, which operates as a Fastbus Master and as a Readout Controller at the same time. Data are collected and properly formatted by the MBS (Multi Branch System) acquisition software, developed at the GSI laboratory (Darmstadt, Germany).

In Figure 2.1.5 is schematically shown the block diagram of the whole data acquisition system.

2.1.2 Trigger of the experiment

As it is well known, a crucial point in the set-up of the read-out electronic chain is the choice of the logic signal used as event trigger. This gives the temporal reference (*time zero*) of the detected event and enables the read out of the data.

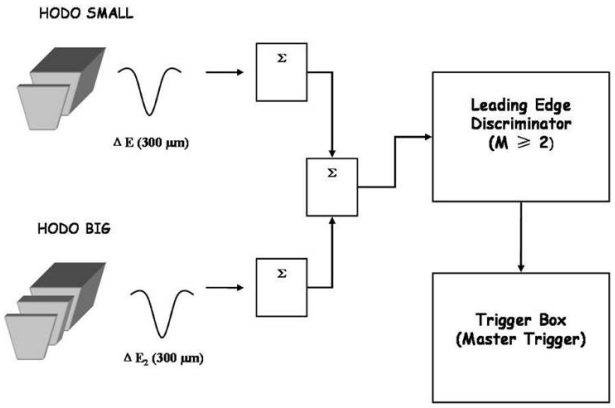

Figure 2.1.6: Schematic diagram of the experimental trigger.

To this purpose, each detector was associated to a logic value which is equal to one only when the detector generates a signal above the discriminator threshold. Moreover, all the gates, the fast clear and the start acquisition signals are derived from the trigger. As it can be seen from Figure 2.1.6, they are directly derived from a module called Trigger-Box which issues a 16 bits word, called TPAT (Trigger Pattern). Every bit in this word corresponds to an event, so that the value of the bit (1 or 0) itself would signify the occurrence of that event. This value was written into the data word, so that the data could be selected depending on the associated trigger type.

During the experiment we were interested in the acquisition of events in which at least two particles were detected (M$\geq$2) in any of the two hodoscopes (Interaction Trigger), since the main objective was to study the ^{12}C fragmentation process. To get the multiplicity (M) signal from both hodoscopes, the analog sum of the 300 μm Zero Crossing signals was extracted and sent at the input of a Leading Edge Discriminator, whose thresholds were set to 150 mV for M=1 and to 250 mV for M$\geq$2 events.

In Figure 2.1.6 a block-diagram of the defined trigger signal for the FRAG experiment is shown.

To correctly normalize data, the events associated to M≥1 were also collected (Beam Trigger) and scaled of a factor 2^4, in order to avoid the increase of the dead-time of the acquisition system. The logic OR between all the trigger signals given by the Trigger-Box is called Master Trigger. This is used to generate the QDC and the stretcher common GATE signals.

2.2 Fragmentation at Fermi energies on thick targets

The second experiment at Fermi energies, FRATT[4], discussed in the present work, was performed at the LNS-INFN in Catania, aiming at studying the fragmentation of a ^{12}C beam at 62 AMeV on different tissue-equivalent[5] targets. Specifically, the targets used were: a 3.28 mm thick PMMA[6] target and four lung-equivalent targets (3.12, 5.81, 10.3 and 20.6 mm). In order to simulate the environmental conditions of a medical treatment, the nuclear reactions took place in air. The transition from vacuum to air were obtained by means of a 50 μm thick kapton window. A collimation system was constituted by a 30.1 cm long brass cylinder, with a 3 mm entrance, 26 mm internal diameter and variable aperture, set to 1 mm for the experiment.

In Figure 2.2.1 a schematic drawing of the set-up along the beam path is shown.

After collimation, the beam interacted first with a 50 μm thick plastic scintillator made of Viniltoluene, with 60×60 mm^2 total area and an active section of 30 mm diameter, which measured the beam intensity (see Figure 2.2.2). The reaction products were detected by means of a ΔE-E_{res} telescope. The first detection stage (ΔE) is represented by a surface barrier silicon detector 96 μm thick and 50 mm^2 of total area, shown in Figure 2.2.3 (a). The second stage (E_{res}), where particles stop, is constituted by a CsI(Tl) crystal 20 cm long and with a section of 40 mm diameter coupled with a photomultiplier tube. In Figure 2.2.3 (b) a picture of the experimental set-up is shown.

[4] FRAgmentation on Thick Target.

[5] Tissue-equivalent materials (TEMs) are specifically manufactured in order to mimic the elemental composition and density of the different human organs tissues and are widely used in quality assurance and calibration procedures, both in radiodiagnostics and radiotherapy.

[6] PolyMethylMethAcrylate.

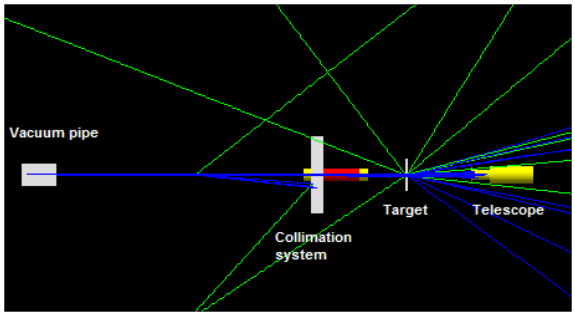

Figure 2.2.1: Layout of the beam line and the detection system. The blue tracks represent positive charged particles, while the green ones represent neutral particles.

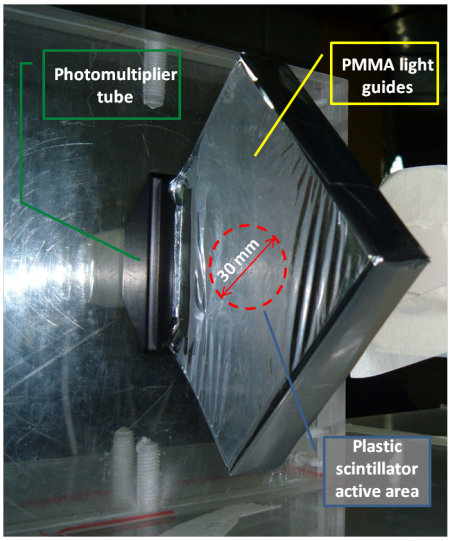

Figure 2.2.2: Picture of the plastic scintillator intercepting the beam with its support.

Signals coming from both the detection system and the plastic scintillator are processed by a NIM-CAMAC standard electronic chain. After fragmentation of ^{12}C ions within the target, charged fragments interact with the two detectors of the telescope. Each of them produces a signal which is sent to the input of a charge preamplifier (ORTEC 142A). The output pulse of the preamplifier is driven at the input of a spectroscopic amplifier (ORTEC 572). The shaped analog signals are then digitalized by a Peak

Sensing ADC for data acquisition and storage. In particular, the ADC Silena 4418/V, used for the experiment, accepts maximum signal amplitudes of 10 V and converts them on a 12 bit scale, which corresponds to 2,5 mV per channel resolution.

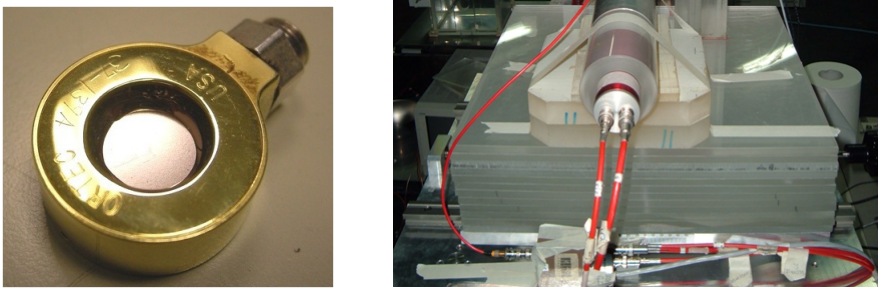

(a) (b)

Figure 2.2.3: (a): Picture of the surface barrier silicon ΔE detector used during the experiment. (b): ΔE-E_{res} telescope placed along the beam path.

The fast part of signal processing involves the use of a Time Filter Amplifier (TFA) ORTEC 474, which produces a fast shaped signal sent to the input of a discriminator (CAEN N413A) and then to a Gate Generator (ORTEC GG 8020). During the experiment, the time window of the gate signal was set to 4 μs.

The ADC crate used for the experiment is a MINI-CAMAC crate with 11 slots, where the last two are occupied by the crate controller Jorway 73A, connected by a SCSI 2 bus to the acquisition system. To read and store data, a computer with LINUX operating system and the TATOCAMAC acquisition software, developed at the INFN-LNS, was employed. The trigger of the acquisition system was derived by the ΔE silicon detector.

2.3 The experiment at relativistic energies

The FIRST[7] experiment at the SIS accelerator of GSI laboratory in Darmstadt (Germany) has been designed for the measurement of ion fragmentation cross-sections at different angles and energies between 100 and 1000 AMeV. The start of the scientific program was on summer 2011 and was focused on the measurement of 400 AMeV ^{12}C beam fragmentation on an 8 mm graphite target.

Interaction Region (before bending by ALADiN spectrometer)			
Name	**Function**	**Angular coverage**	**Trigger**
Start Counter	Start of TOF		Yes
Beam Monitor	Beam direction and impact point on target		No
Vertex Detector	Fragment emission angle from target	≤ 40	No
KENTROS	TOF, ΔE and coarse spatial resolution	$\approx$ 5-90	Yes
Large Detector Region (after bending by ALADiN spectrometer)			
Name	**Function**	**Angular coverage**	**Trigger**
TP-MUSIC IV	ΔE, fragment tracking after bending	≤ 5	No
TOF-Wall	Stop of TOF, ΔE and coarse spatial resolution	≤ 5	Yes
Veto Counter	Trigger veto, TOF and ΔE	≤ 1	Yes
LAND	Neutron detector, TOF, ΔE and coarse spatial resolution	≤ 10	Yes

Table 2.1: Overview of subdetectors constituting the FIRST experiment setup.

The beam provided by the SIS accelerator is characterized by a rate of incoming particles in the range of the kHz and by a Gaussian shape in the transverse plane of $\approx$ 2.1 mm size (σ). The time structure of the provided

[7]Fragmentation of Ions Relevant for Space and Therapy.

spill has a flat shape of ≈ 10 s out of 20 s total duration.

As shown in Table 2.1, the experimental setup consists of several subdetectors divided in two main blocks: the Interaction Region, placed around the carbon target and based on newly designed detectors, and the Large Detector Region, made by an already existing setup. The resulting dimensions of the two regions are significantly different: the impinging beam and produced fragments are studied in the Interaction Region within some tens of centimeters from the target, while the devices that detect the fragments, after magnetic bending, in the Large Detector Region have typical dimension of meters.

Following the beam path, the Interaction Region is made of a Start Counter (SC) scintillator which provides the start to the time of flight (TOF) measurement, a drift chamber Beam Monitor (BM) measuring the beam trajectory and impact point on the target, a robotized target system, a pixel silicon Vertex Detector (VD), to track the charged fragments emerging from the target and, finally, a thick scintillator Proton Tagger (KENTROS) for detecting the light fragments at large angles.

A schematic view of the FIRST experiment setup is shown in Figure 2.3.1.

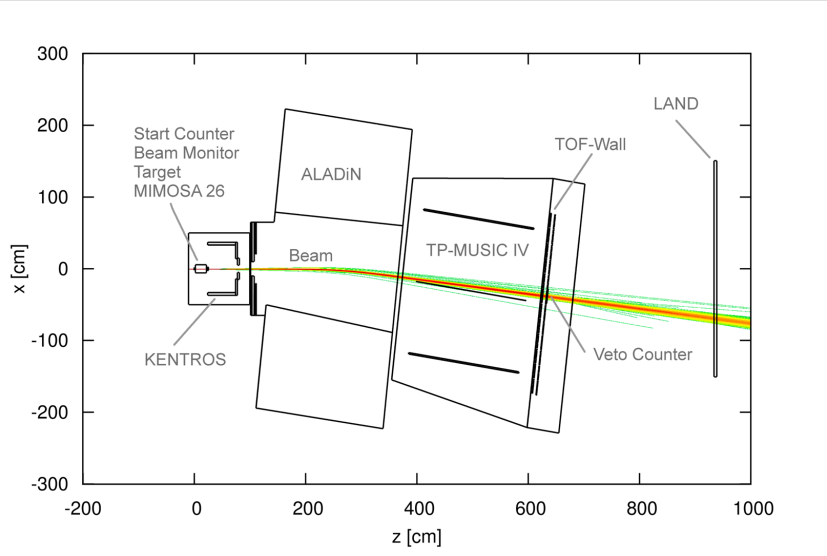

Figure 2.3.1: Top view of the implementation of the FIRST setup. The line shows the path of non-interacting beam particles.

The Interaction Region (IR) detectors worked in air: this choice greatly helped their design and running. On the other hand, the small IR volume placed at the atmospheric pressure increases the probability of out-of-target interaction only by about 5%.
With the noticeable exception of the large angle protons and a little fraction of ^{4}He, most of the projectile fragments are produced in the forward direction with the same β of the beam. These Z $\geq$ 2 fragments are within the magnetic acceptance of the ALADiN dipole magnet and, after magnetic bending, they enter in the Large Detector Region being detected by the large volume time projection chamber (TP-MUSIC IV) which measures track directions and energy releases. A large area system of scintillators (ToF-Wall) provides the measurement of the impinging point and the arrival time of the particles. The Veto Counter, a scintillator sandwich positioned after the ToF-Wall in correspondence of the non-interacting beam path, is used to analyze the beam. Finally, the Large Area Neutron Detector (LAND), made of a stack of scintillator counters, gives information about the neutrons emitted within an angle of $\approx 10^\circ$ with respect to the beam. In particular, the tracking before and after the magnetic bending, coupled with the knowledge of beam direction and impact point on the target, will provide information on the p/Z ratio of the produced fragments.

In particular, the FIRST setup [103] fulfills several requirements: a suitable particle identification capability providing a $\Delta M/M \leq 10\%$ (where M is the fragment mass), tracking capability to measure angles and momenta of the produced charged fragments, large angular acceptance for low energy protons, and finally a proper angular acceptance for the forward produced neutrons.

In the next sections, a more detailed description of each subdetector constituting the experimental setup is given.

2.3.1 The Interaction Region

A picture of the Interaction Region is shown in Figure 2.3.2. All the detectors of this region have been tested at the 80 AMeV ^{12}C beam of the Superconducting Cyclotron at LNS-INFN in Catania or at the Beam Test Facility 510 MeV electron beam of the INFN Laboratori Nazionali di Frascati [104].

The Start Counter is a thin scintillator located on the beam path 20 cm before the target. This device measures the arrival time of a beam projectile and provides a logic signal to the experiment trigger. In order to fulfill the requested precision on fragment time of flight measurement, and hence

achieve a 10% relative error on the fragment masses, a time resolution better than 250 ps (standard deviation) is necessary. Such resolution also allow the measurement of the kinetic energy of the fragments detected in the proton tagger, where a few ns time of flight is measured (flight path $\leq$ 80 cm). The scintillator must be as thin as possible to avoid beam fragmentation before the target.

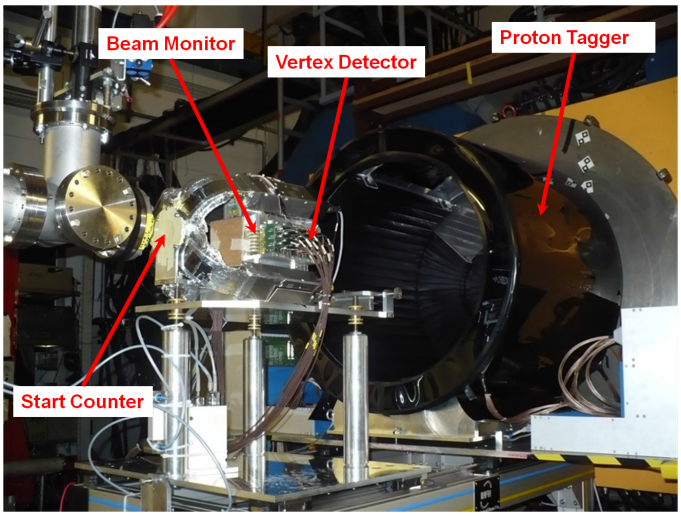

Figure 2.3.2: Picture of the Interaction Region, embedding the Start Counter, the Beam Monitor, the Vertex Detector and the Proton Tagger. The Interaction Region is located at the entrance of the ALADiN magnet.

The SC is made of a circular thin foil of EJ228 plastic scintillator, with a maximum emission wavelenght centered at 390 nm, a diameter of 52 mm and a thickness of 150 μm. The light produced by the scintillator is collected radially by a crown of 160 optical fibers, 1 mm diameter each. The fibers are radially glued and grouped in four bundles and read by fast photomultipliers Hamamatsu H10721-210, with 40% quantum efficiency and a time resolution of 250 ps/$\sqrt{N_{ph.el.}}$ (see Figure 2.3.3), being $N_{ph.el.}$ the total photoelectron yield.

The Beam Monitor is a drift chamber providing two orthogonal profiles of the beam, each view detected by six planes of three cells, for a total of 36 wires oriented alternatively in the horizontal and in the vertical direction. The cell shape is rectangular (10$\times$16 mm^2) with the long side orthogonal to the beam, in order to minimize the possibility of an interaction of the

beam with the wires. To reduce tracking ambiguities, the consecutive layers of each beam view are staggered by half a cell. The active volume of the chamber is 2.4×2.4×14 cm^3. The chamber is operated on carbon beam at a working point of 1.8 kV in Argon/CO_2, 80%/20% gas mixture.

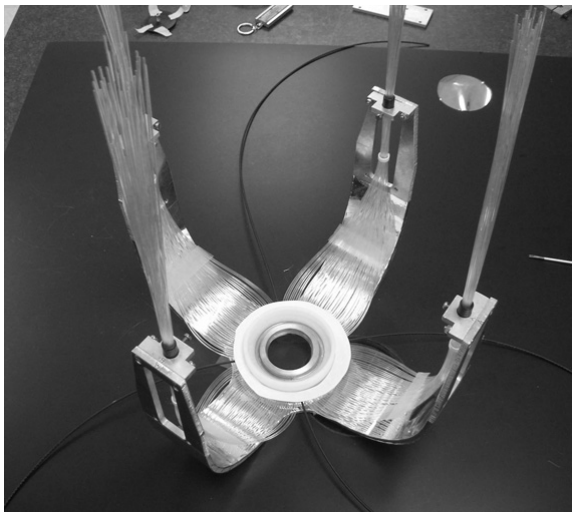

Figure 2.3.3: The thin scintillator foil of the Start Counter read out by scintillating fibers.

Custom front-end electronics boards are embedded in the detector and provide wire signal amplification by a factor of about 10. A technical drawing of the chamber is shown in Figure 2.3.4 together with the cells scheme.

The main task of the BM is the tracking of the arriving carbon, with a precision of the order of $\cong$ 100 μm on the impact point on the target. This resolution is needed to discriminate between double carbon tracks that can be registered, in a single event, by the slower vertex detector, with 10% probability at 1 kHz beam rate. In particular, the beam track detected by the BM in these events must point to the correct carbon track in the VD, where clusters of 100 μm size are built. This single hit space resolution of the chamber is also needed to provide a good angular resolution on the scattering angle between the projectile and the fragments produced. Indeed, the measured spatial resolution of $\cong$ 140 μm, the very high hit detection efficiency for carbons ($>$ 95%) and the high overall tracking efficiency ($\approx$ 90%) confirm the good detector performances.

The Vertex Detector [105] must fulfill several requirements. Even consid-

ering the non-negligible transverse size of the beam spot ($\cong$ 5 mm), a wide angular coverage is needed to track also large angle projectiles that do not enter the ALADiN region. The angular resolution on tracks direction needs to be measured with an accuracy of $\approx 0.3°$, driven by the TPS requirements. A good two tracks separation, with a precision at few % level, is needed to minimize reconstruction systematic errors. In addition, an overall thickness of few % with respect to target thickness ($\approx$ 0.5 cm) is required in order to reduce the out-of-target interactions. Moreover, a wide dynamic range is preferable in order to be able to detect both minimum ionizing particles and carbon ions of the beam.

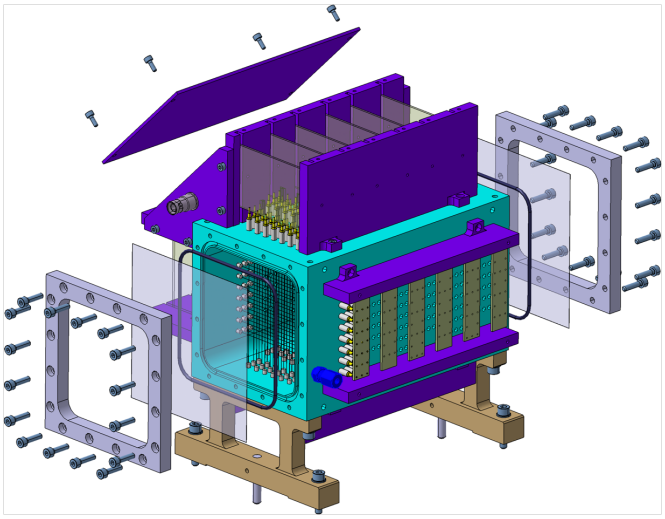

(a)

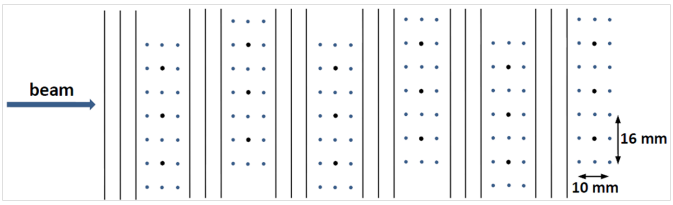

(b)

Figure 2.3.4: Technical drawing (a) and cells layout (b) of the Beam Monitor drift chamber.

In more detail, the MIMOSA26[8] [106] pixel sensor has been chosen to equip the vertex detector. MIMOSA26 has a sensitive area of 10.6×21.2 mm^2, subdivided in 576 rows and 1152 columns of pixels with 18.4 μm pitch with a frame read out time, in rolling shutter mode, of 115.2 μs. The sensor, that provides only digital information on fired pixels, is equipped with zero suppression logic to reduce the data acquisition system bandwidth. Information from the BM detector will be used to identify the on target interaction, and hence the fragmentation vertex, for each event, allowing to properly associate the different tracks and clusters, in pile-up events, to their origin vertex.

As shown in Figure 2.3.5, the vertex detector is made of four stations, each one housing two MIMOSA26s sensors glued on the two sides of a printed circuit board in corrispondence to a square hole below the 2×2 cm^2 sensor area. The measured spatial resolutions are ≈ 10 μm for both x and y positions and ≈ 60 μm for the z positions. Moreover, a tracking efficiency > 99% has been estimated.

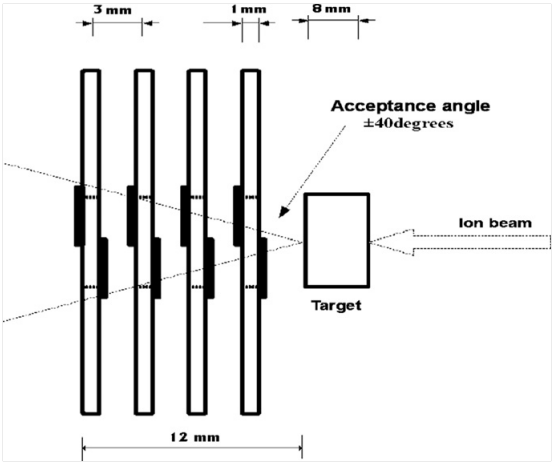

Figure 2.3.5: Relative positions of beam, target, four vertex stations and sensor housing board dimensions.

The KENTROS[9] detector, placed between the vertex detector and the ALADiN magnet, is aimed at kinetic energy and time of flight measurement of light charged particles produced at polar angles larger than about 5°. In particular, the detector response is optimized for the low energy protons.

[8]Minimum Ionizing MOS (Metal-Oxide-Semiconductor) Active pixel sensor.
[9]Kinetic ENergy and Time Resolution Optimized on Scintillator.

The kinetic energy of charged particles reaching the detector can be estimated by the energy deposition and the time of flight measurements. In order to achieve a $\leq 15\%$ relative error on protons with kinetic energies up to 100 MeV (the most interesting case from a TPS perspective, since they release their full energy inside the patient body), the detector geometry and electronics readout has been designed in order to provide a time resolution of 250 ps.

The active part of KENTROS is made of organic scintillator modules and scintillating fibers. The modules are made of EJ-200 Polyvinyltoluene fast scintillator, which has a decay time of 2.1 ns, 10000 photons/MeV light yield, 425 nm wavelength of maximum emission and 4 m attenuation length. The scintillating fibers are 1 mm diameter BCF-10 fibers by Bicron. The scintillation light is driven from the scintillator modules to silicon photomultipliers (SIPM) using plexiglass lightguides. The SIPM used are made by AdvanSiD and have 4×4 mm^2 active area. The SIPM output is processed by a custom electronics that amplifies, reshapes, splits and discriminates the signals in order to properly feed them in TDCs, ADCs and to provide a discriminated OR-ed signal for triggering purpose.

As shown in Figure 2.3.6, the cylindrical shaped detector consists of three main parts.

- A barrel (see Figure 2.3.6 (d)) which detects particles with polar angle between 36° and 90°. The external barrel diameter is 74 cm, and it is made of 50 scintillator modules, 3.8 cm thick, oriented in a direction parallel to the beam. Internally with respect to the barrel there are two layers of 1 mm diameter scintillating fibers that are bent to form circles in the polar region from 40° to 90°, providing a resolution on the azimuthal angle $\sigma_\Phi \cong 2°$.

- A big endcap (see Figure 2.3.6 (b)) covering polar angles between 15° and 36°. This device has the shape of a disk with a hole, with internal and external diameters of 28 and 74 cm, respectively. It is composed of 60 trapezoidal scintillator modules, having 3.5 cm thickness along the beam direction.

- A small endcap (see Figure 2.3.6 (c)), for particles with polar angles between 5° and 15°. This device has 10 cm internal and 30 cm external diameter. It is composed by 24 trapezoidal scintillator modules, having 3.5 cm thickness along the beam direction.

In the energy range of the protons produced in the FIRST experiment, the energy resolution ranges from a few percents for protons having 100

MeV kinetic energy to slightly more than 10% for 400 MeV kinetic energy protons.

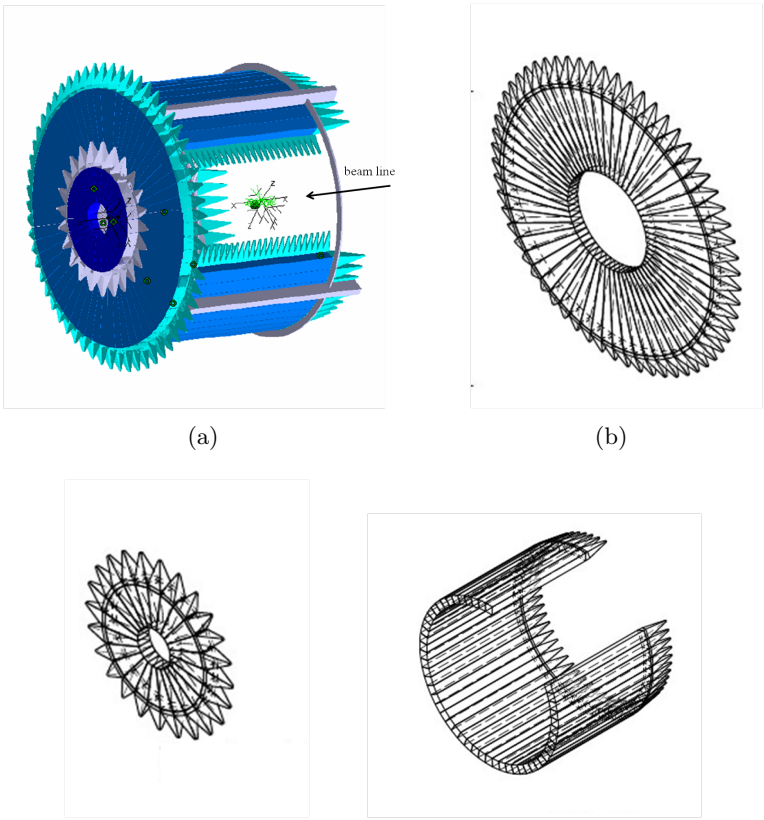

Figure 2.3.6: Technical drawings of the KENTROS Proton Tagger. a) General assembly, (b) big endcap, (c) small endcap and (d) barrel.

2.3.2 The TP-MUSIC IV time projection chamber

The fragments, produced by the 400 AMeV ^{12}C beam interacting with the target and emitted in the forward direction, enter in the large detector region and cross the ALADiN[10] [107] dipole magnet. The ALADiN field bends the charged fragments trajectory providing information about their

[10] A Large Acceptance DIpole magNet.

charges and momenta. After magnetic bending, the particles go through the TP-MUSIC IV[11] [108] detector, a tracking ionization chamber able to measure the charge and the momentum of nuclei from He up to Au with high efficiency and high resolution [109].

A cathode plane in the middle separates the active volume of the detector into two distinct drift regions with ionization chamber sections and proportional counters on each side [110], for measuring both the heavier and lighter particles signals respectively. The position of the ionizing particles in the non-bending plane is determined from the position along the proportional counters, whereas the position in the bending plane is determined by measuring the drift time of the ionization electrons from the track path to the proportional counters. In order to couple with the large dynamic range of the detector and to disentangle the different particles in multiple-hit events, 14-bit FADC's digitize the signals coming directly from the preamplifiers. The device is operated in a P10 (10% Methane and 90% Argon) gas mixture.

Unfortunately, it was not possible to use the TP-MUSIC IV detector during the experiment, due to an anomalous current increase in the main cathode, thus allowing to increase the event acquisition rate up to values of the order of kHz, while before it was limited to about 350 Hz, due especially to the large dead time determined, among other reasons, by the electrons drift time in the TP-MUSIC IV chamber.

2.3.3 The ToF-Wall detector

The ToF-Wall detector [111] has been used to measure the time of flight of the fragments produced in the studied reaction. It is located at 6.5 m from the target and its angular acceptance is within 6.5° with respect to the undeviating beam direction. The whole detector is inside a chamber filled with nitrogen and separated from that containing the TP-MUSIC IV by a mylar window.

The ToF-Wall is made up of two detector layers (front and back), perpendicular to the beam, each made of 12 modules. Each module consists of 8 plastic scintillators (BC-408), 1.10 m long, 2.5 cm wide and 1 cm thick, covered with an aluminium foil and oriented in the vertical direction. A brass foil 0.5 mm thick between the two layers shields the back side from the δ electrons generated in the front side, in order to improve the charge identification.

[11] Time Projection Multiple Sampling Ionization Chamber.

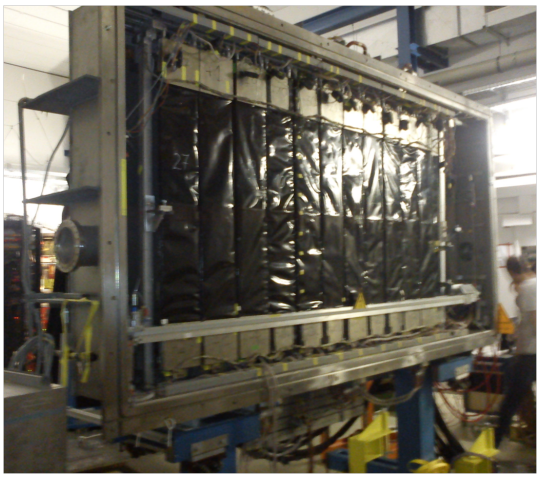

(a)

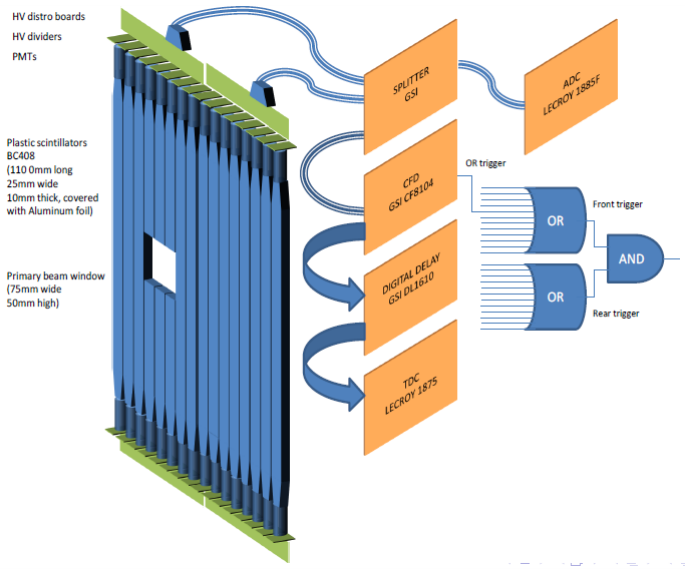

(b)

Figure 2.3.7: A picture of the ToF-Wall inside the detector chamber (a) and a sketch of two modules containing 8 plastic scintillators represented with the associated electronic chain (b). The module corresponding with the primary beam window is the central one.

The two layers are shifted from each other of 1.25 cm, corresponding to half a slat, in order to maximize the probability that incoming fragments hit at least one slat. Each slat is read on both ends by two R3478 Hamamatsu photomultipliers. The signal is split and digitized by Fastbus QDCs and by TDCs, to extract the energy and time information, respectively. Both the detector and the schematic drawing of two scintillator modules are shown in Figure 2.3.7.

Since the ToF-Wall had to compensate the lack of information due to TP-MUSIC IV breakdown, the detector operated without hardware pedestal subtraction, to enhance detection efficiency also for light fragments and prevent any further loss of information. In this context, the performances of the ToF-Wall detector are of particular importance to extract information about charge and energy of the emitted fragments. As a result, some mention of the calibration procedures adopted is given.

A calibration procedure characterized by known conditions of the beam trajectory and velocity was carried out. A set of calibration runs without target was taken by deflecting the carbon beam along the horizontal plane and all over the slats, through the ALADiN magnetic field modulation. As a consequence, ^{12}C ions energy is known and their trajectories can be reconstructed by geometrical calculations. Since hit coordinates, time of flight and energy loss are known, other constant factors, e.g. delays and gains, can be extracted by the measured quantities.

Among the physical quantities of interest measured by the ToF-Wall, there are the X, Y and Z coordinates of each fragment impact point on each slat. A right-handed coordinate system is used having the z axis pointing in the beam direction, and the x and y axis pointing in the horizontal and vertical direction respectively.

Particularly, the X and Z coordinates are univocally determined by the slat position, while the Y coordinate can be derived from the difference between top and bottom TDCs readings [112].

Defining τ_t and τ_b as the times taken by the light pulse to propagate along the slat from the hit point to the top and bottom photomultipliers (PMTs) respectively, and indicating the velocity of light within the slat as v_{slat}, the Y coordinate is given by:

$$Y = v_{slat} \cdot (TDC_b - TDC_t + \Delta_t - \Delta_b)/2, \tag{2.3.1}$$

where $\mathrm{TDC}_{t(b)} = \tau_{t(b)} + \mathrm{TOF} + \Delta_{t(b)}$, being TOF the difference between the average time value of the TDCs readings and the time measured by the Start Counter and $\Delta_{t(b)}$ the constant delay associated with the top (bottom)

channel.

During the calibration runs mentioned above, since the horizontal plane was taken as a reference, the vertical coordinate was known, then the constant offset given by channel delays, (Δ_t - Δ_b), was determined after assessing $Y = 0$ in equation (2.3.1). Consequently, it was possible to align the Y readings for all the slats by subtracting the mean to (TDC_t - TDC_b) measured values, obtaining for a single slat a resolution of $\delta Y \approx 3$ cm.

As a result, a scatter plot of the Y coordinate with respect to the slat number for both front and rear walls is shown in Figure 2.3.8.

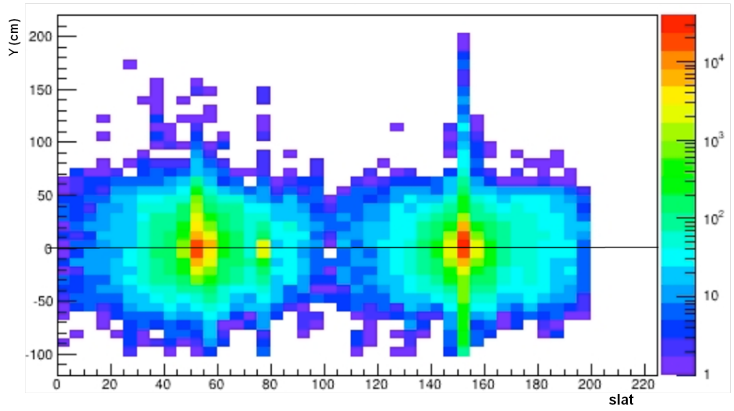

Figure 2.3.8: Scatter plot of the Y position with respect to the slat number for both ToF-Wall front and back sides, after Y calibration. The data refers to a ^{12}C + ^{12}C fragmentation run.

With the same meaning of the quantities already defined, the TOF was derived from the sum of the top and bottom TDCs readings as:

$$TOF = (TDC_t + TDC_b - T - \Delta_t - \Delta_b)/2, \tag{2.3.2}$$

being $T = \tau_t + \tau_b$ a constant.

Since, during the calibration runs, ^{12}C ions were deflected from the beam line on each slat with known energy, and their path length was determined through geometrical calculations, the TOF was evaluated slat by slat and the constant delays in equation (2.3.2) was also determined. The estimated time resolution is about 0.5 ns, to be compared with the minimum time of about 30 ns spent by the fastest fragment to reach the detector.

The fragment energy loss E_0 in a given slat is a function of its incident energy E, charge Z, mass m and impinging angle α. The energy deposited in

each slat is split into two light pulses propagating towards the two opposite PMTs, which read different signal amplitudes because of the two different paths travelled by photons.

These signals are then digitalized into the ADC_t and ADC_b values. After pedestal subtraction, these values can be related to the electric signals generated in the two PMTs, which depend on the quantity of light collected and, then, on the distance between the interaction point and the PMT. In particular:

$$ADC_t = \epsilon_t \cdot E_0 \cdot e^{-\mu(\frac{L}{2}-Y)} \tag{2.3.3}$$

$$ADC_b = \epsilon_b \cdot E_0 \cdot e^{-\mu(\frac{L}{2}+Y)}, \tag{2.3.4}$$

being ϵ_t and ϵ_b the PMT and electronics gains and μ the slat absorption coefficient. Taking the square root of the product of the two signals, the result is a quantity that does not depend on the position but only on the produced light, so that it gives the total deposited energy E_0:

$$E_0 = K \cdot \sqrt{ADC_t \cdot ADC_b}, \tag{2.3.5}$$

where $K = 1/\sqrt{\epsilon_t \cdot \epsilon_b \cdot e^{(-\mu L)}}$ is a constant.

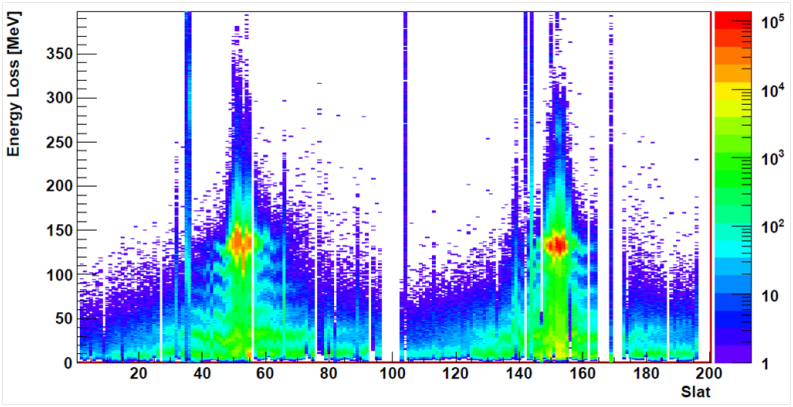

Figure 2.3.9: Energy distribution for ^{12}C ions and fragments as a function of the slat number for the front and back wall. The empty energy bins refer to those slats with, at least, one broken ADC channel.

According to the Bethe-Bloch formula, ^{12}C ions at 400 AMeV release about 116 MeV after crossing 1 cm thick plastic scintillator so that, by

means of equation (2.3.5), the calibration factors for each slat have been evaluated. The energy loss in each slat with respect to the slat number is shown in Figure 2.3.9 for fragmentation events.

The scatter plot of TOF with respect to the energy loss measured by a single slat for all the experimental runs taken with the carbon target is shown in Figure 2.3.10, together with the projection onto the energy axis. In both plots, six separated regions can be distinguished which correspond to particles with charges ranging from Z=1 to Z=6 from left to right, demonstrating the good charge identification capability of the ToF-Wall.

The good performances of the detector will be used, within the global track reconstruction, to determine the kinetic energy of the fragments produced.

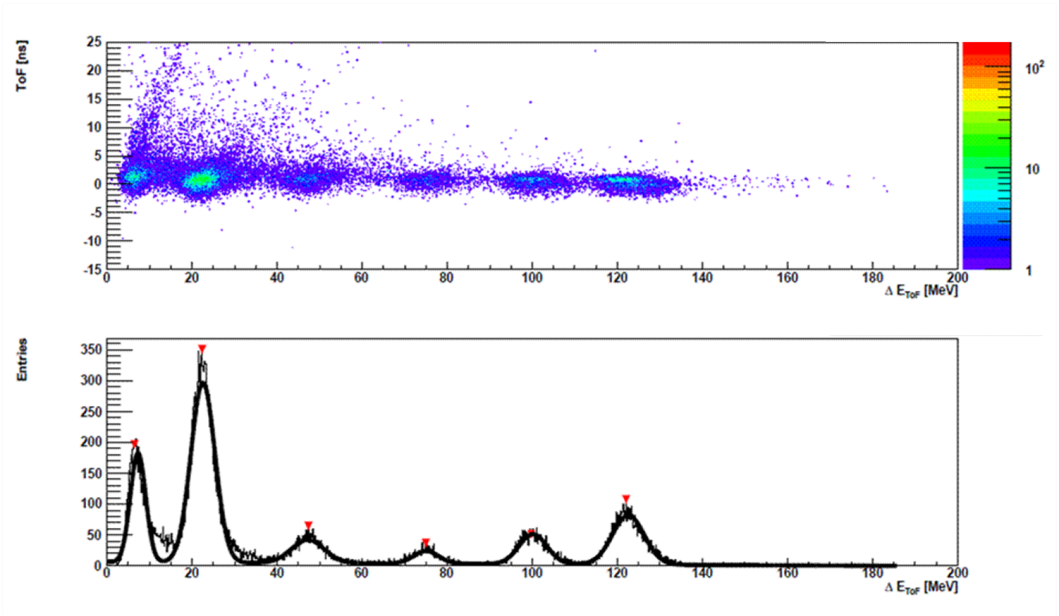

Figure 2.3.10: (top) TOF versus energy loss for a single slat. The six regions in the plot correspond to the ion fragments with charge ranging from Z=1 to Z=6; (bottom) Projection on the energy axis.

2.3.4 The LAND detector

The Large Area Neutron Detector (LAND) [113] [114] has been used to detect neutrons. The detector has an active area of 2×2 m^2 and its

depth is 1 m. It features a multilayer structure of passive converter and active scintillator materials. Using material rich of protons, such as plastic scintillators, the neutron can be detected looking to the light produced by the proton elastically scattered by the neutron.

The full detector is divided into 200 paddles of 200×10 cm^2 area and 10 cm depth. Each paddle contains 11 sheets of iron (the two outer ones are 2.5 mm thick, the others are 5 mm thick) and 10 sheets of 5 mm thick scintillator, mounted in an iron sheet box which has a wall thickness of 1 mm. Twenty paddles are arranged in one layer; adjacent layers are mounted with the paddles perpendicular to each other, thus giving position information in both vertical and horizontal directions. A sketch of the detector and the single paddle are shown in Figure 2.3.11.

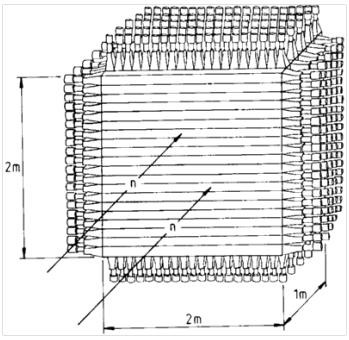

(a)

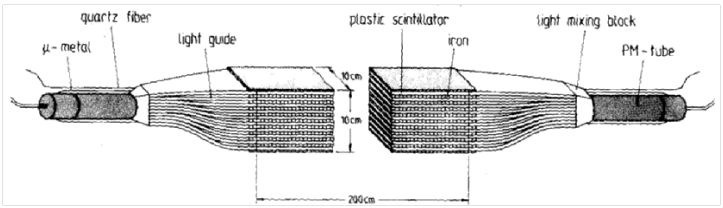

(b)

Figure 2.3.11: Sketch of LAND neutron detector (a) and of one paddle (b). The layer structure together with the bent light guide strips, light mixing blocks and photomultipliers are shown.

Light produced in a paddle is collected by means of stripe light guides on both ends of the scintillator sheets and is directed to the photomultipliers. The difference in arrival time of the two signals is used to localize the position

where scintillation light was produced by secondary charged particles, while their mean value provides time of flight information. The time resolution of the modules ranges from $\Delta t = 210$ - 250 ps (σ) and the position resolution $\Delta x = 7$ - 10 cm, depending on the detector. For neutrons emitted with kinetic energies in the 0.5 - 4 MeV range, an energy resolution of 0.4 - 1 MeV was measured.

2.3.5 The Veto Counter

The Veto Counter (VC) detector is placed after the ToF-Wall on the magnetic path of the carbon projectiles that do not interact in the setup. The counter is made of two scintillator slabs (BC-404 by Saint Gobain), with parallelepiped shape and with a volume of $6\times6\times3$ cm^3 and $4\times4\times6$ cm^3, respectively. The two slabs are put one on top of the other, with the equal sides orthogonal to the carbon track and centered with respect to the carbon path. The larger slab is read by two PMTs by Hamamatsu on both sides, while the little one is read from the rear direction, along the beam.

The signals are read out by the same ADCs and TDCs used for KENTROS. The VC monitors the amount of fragments that are produced in the same angular range of the non-interacting beam. The Veto Counter signal is also used to label non-interesting events where the carbon projectile has not interacted and arrived unperturbed on the Veto Counter.

2.3.6 Data acquisition system and trigger

The readout is handled by the Multi Branch System (MBS), a general DAQ framework developed at GSI [115]. In the MBS several intelligent bus controllers (CES RIO), running under the real-time operating system LynxOS, perform the readout of the digitization modules of the individual crates, when triggered by the dedicated trigger modules. All the trigger modules, one in each readout crate, are connected via a trigger bus to distribute the trigger and dead-time signals and to ensure event synchronisation. Data collected by single controllers are broadcast via Ethernet to an event-builder where they are merged and saved in the standard GSI format. A set of client-server applications allows to control the data acquisition, to remotely configure the detector settings and to perform on-line monitoring of the data quality. MBS can handle easily the different Front End Electronics standards used by the different subdetectors: FASTBUS, CAMAC and VME.

The dead time due to trigger signal formation and readout is of the

order of ms per event due to several factors as conversion time in the digitization modules and transfer data time from the electronics to the readout controllers and from the controllers to the event builder via TCP/IP. An efficient trigger system is then essential to select the fragmentation events and to keep the counting rate at a level where the inefficiencies due to the dead time are minimized.

The final trigger decision requests the coincidence of the Start Counter trigger with the trigger of any of the detectors: ToF-Wall, LAND, KENTROS, and the downscaled Veto Counter. In order to suppress events in which the carbon projectile does not interact with the target, coincidences between the Start Counter and the Veto Counter can be rejected. An additional unbiased trigger condition based on the Start Counter trigger alone is also foreseen with tunable downscale factor to estimate the efficiency of the other trigger conditions.

The reported trigger logic is implemented in an FPGA[12] programmable VME module (VULOM4 [116]). This module accepts individual trigger signals and implements all the logic matrices and the downscale factors needed to control the trigger conditions, the scalers to count input and output triggers, the internal generators of regular calibration triggers and the locking mechanism to block the propagation of triggers during the dead time. Different trigger conditions for the accepted triggers are encoded on different lines of the trigger bus and propagated to the readout electronics.

Finally, in order to avoid the delay lines needed to synchronize the KENTROS analog signals to the ADC's with the delayed master trigger decision, a two-level trigger system is implemented for the detectors in the interaction region. The analog signals are processed in the ADC's as soon as the local trigger from the start counter is generated; if no master trigger is received within a fixed time, fast clear signal is provided to the electronics and the event is ignored by the DAQ system.

[12]Field Programmable Gate Array.

Chapter 3

Carbon fragmentation at Fermi energies

As already mentioned, the main drawback of carbon ions treatment is related with the production of lighter fragments within the patient tissue, as far as the primary beam may undergo inelastic nuclear reactions along the penetration path. The resulting spatial dose distribution, both inside and outside the tumor region, is thus altered by secondary fragments, having longer ranges and broader angular distributions with respect to the pristine beam. Additionally, the carbon ions RBE has to be replaced by the one associated with the arising mixed radiation field, as far as RBE depends strongly on the LET value, which is different for each isotopic species. Therefore, all these effects arising from the carbon fragmentation have to be correctly evaluated when planning a tumor treatment.

In this context, the experimental results extracted from ^{12}C fragmentation data at Fermi energies on both a thin carbon target and different thick tissue-equivalent targets will be discussed in the next sections.

3.1 Thin target measurements

In the following, both double-differential cross sections and angular distributions relative to the secondary fragments produced in ^{12}C + ^{12}C reaction at 62 AMeV in a wide angular range will be evaluated [117]. Moreover, the comparisons between the measured fragmentation cross sections and the GEANT4 predictions will be also shown and discussed. These results represent the first comparison of the GEANT4 nuclear reaction models performed

so far by using experimental data obtained with a thin target at intermediate energies.

3.1.1 Calibration procedures

The first fundamental step of the data analysis is represented by the energy, charge and mass calibration for each telescope of the two hodoscopes used to detect the reaction products. The applied calibration procedure is essentially based on the ΔE-E$_{res}$ identification technique and can be divided into some well defined steps.

Particularly, two different calibration strategies had to be applied for the silicon and for the CsI(Tl) detectors. Indeed the response of a silicon detector does not depend on charge and mass of the incident particle and is represented by a linear function of the energy deposited inside the detector. In contrast, the scintillation light due to ionizing particles traversing a CsI(Tl) crystal is a not linear function of energy and depends on the charge and mass of the particles. As a result, the hodoscopes energy calibration procedure imply the determination, for each telescope, of the light response curve *L=L(E,Z,A)* for every incident isotope.

As an example, experimental data before applying the energy calibration procedures are represented by the ΔE$_1$-ΔE$_2$ and ΔE$_2$-E$_{CsI}$ scatter plots shown in Figure 3.1.1. It has to be noted the back bending shape of the isotopes bands in the ΔE$_1$-ΔE$_2$ matrixes corresponding to particles which cross both the silicon detectors and stops in the CsI(Tl) crystal (*punch through*). Moreover, the isotopic resolution is good even for lighter fragments thanks to the dual range conversion technique (see section 2.1.1) which avoided the compression of the low range scale of digitized signals.

Energy calibration of a generic Hodo-Big telescope started with finding the relation between the energy released in the 50 μm silicon detector (ΔE$_1$) and the corresponding ADC channel (ADC$_{\Delta E1}$), given by:

$$\Delta E_1\,(MeV) = a_1 + b_1 \cdot ADC_{\Delta E_1}, \tag{3.1.1}$$

being a_1 and b_1 the coefficients to be determined for each telescope. For this purpose, two energy-channels couples of values were needed at least. For high energies, punch through points were chosen and the corresponding energy values were evaluated by computing the energy losses in the two silicon detectors thicknesses. For lower energies, ΔE$_1$-ΔE$_2$ matrix points with ΔE$_2$ = 0, corresponding to particles which stops at the end of the first silicon detector, were chosen. By performing a linear *best fit* for all the

above mentioned points, for each ΔE_1 detector, the a_1 and b_1 coefficients were estimated with an error around 2%.

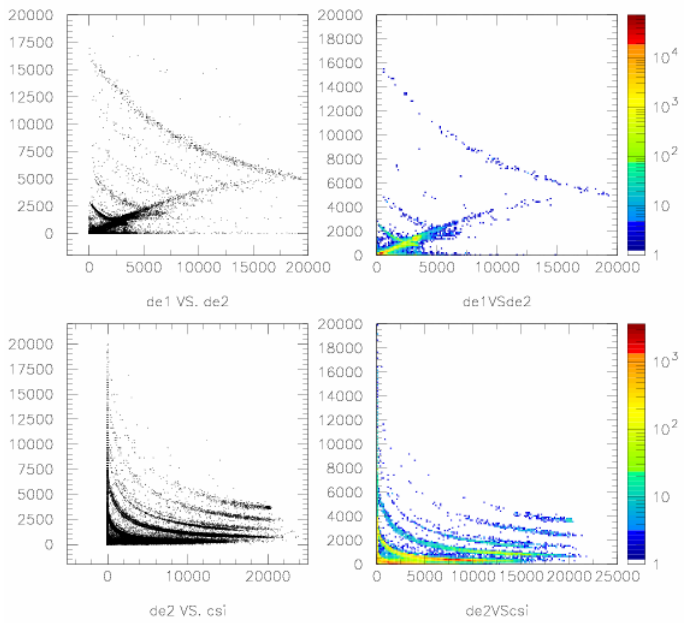

Figure 3.1.1: ΔE_1-ΔE_2 (top) and ΔE_2-E_{CsI} (bottom) scatter plots referred to a not calibrated Hodo-Big telescope.

The second step was the identification of all detected particles, i.e. the assignment of the Z and A values to each of them. For this aim, a graphic linearization of the observed bands in both ΔE_1-ΔE_2 and ΔE_2-E_{CsI} matrixes was performed by means of the fuction:

$$fpid = log\,(\Delta E) + 0.10 \cdot [log\,(E)]^2 - 0.65 \cdot log\,(E)\,, \tag{3.1.2}$$

where ΔE and E are channels values. Each band in the new *fpid-log(E)* matrix was fitted with broken lines defined by a fixed number of vertices so as to associate each line to a new variable, called PIDN (Particle IDentification Number), which uniquely defined charge and mass of the particle. As a result of this procedure, realized by virtue of opportunely created software tools, in Figure 3.1.2 a PIDN spectrum is shown where the different isotopes are well resolved.

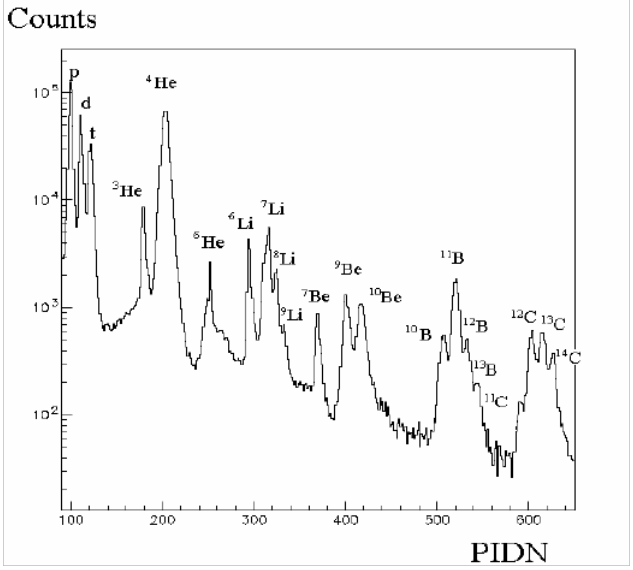

Figure 3.1.2: PIDN spectrum for all the telescopes superimposed to show the good quality of the identification procedure [118].

At this point, knowing the energy lost in the 50 μm silicon detector ΔE_1 and the particle type, the incident energy E_{inc} on each telescope was extracted by energy loss calculations. As a consequence, also the residual energy E_{res} after crossing the first silicon was extracted, being $E_{res} = E_{inc} - \Delta E_1$. For particles which stops at the end of the 300 μm silicon detector, i.e. just before the punch through point, $E_{res} = \Delta E_2$. Exploiting this relationship, the energy-channels linear correlation for ΔE_2 silicon detector was found again by means of a *best fit*, with coefficients errors estimated around 3%. In Figure 3.1.3 a ΔE_1-ΔE_2 matrix, for a selected telescope, after applying the calibration procedures, is shown.

Finally, knowing both the silicon thicknesses traversed by the particles and the corresponding energy losses in MeV, the residual energy deposited in the CsI(Tl) crystals was extracted as $E_{res} = E_{inc} - \Delta E_1 - \Delta E_2 = E_{CsI}$. The energy-channels correlation for the scintillator stage of each telescope was determined by performing a *fit* procedure which, in this case, depends on the charge and mass of the ion. For this purpose, the most suitable functional relationship between the scintillation light and the energy deposited in the crystal is given by:

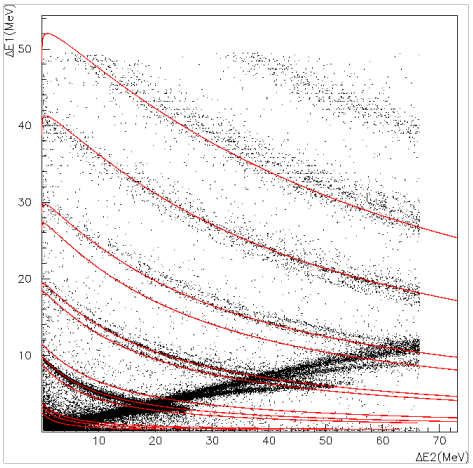

Figure 3.1.3: A ΔE_1-ΔE_2 calibrated matrix. It can be seen the very good overlap between the experimental bands and the theoretical lines obtained through energy loss calculations, confirming the calibrations accuracy.

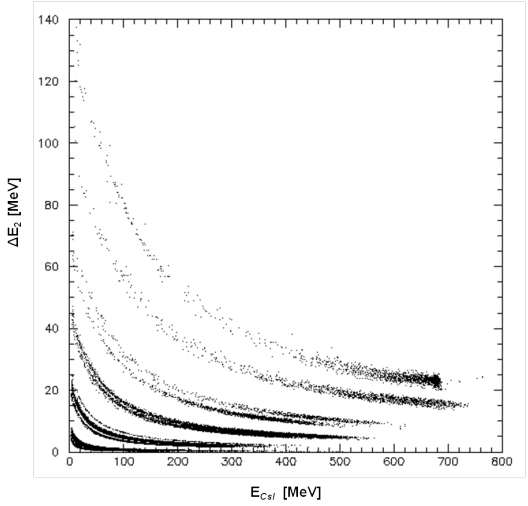

Figure 3.1.4: A ΔE_2-E_{CsI} matrix after applying the complete procedures of energy calibration and isotopes identification.

$$E_{CsI} = a + b \cdot ADC_{CsI} + \frac{c}{d + ADC_{CsI}}, \tag{3.1.3}$$

being E_{CsI} the energy, expressed in MeV, delivered inside the CsI(Tl), ADC_{CsI} the corresponding channel value of light emitted and *a, b, c, d* the coefficients of the curve of equation 3.1.3 which best fits the light response, determined for each telescope and for each (Z, A) couple of values.

An example of the resulting ΔE_2-E_{CsI} matrix obtained at the end of the outlined calibration procedures is shown in Figure 3.1.4. Thus, for each detected fragment, the charge Z and mass A are known together with the total kinetic energy released in each telescope, given by $E_{tot} = \Delta E_1 + \Delta E_2 + E_{CsI}$ where E_{tot} was determined with an estimated error around 6%.

Similar calibration methods have been applied for the Hodo-Small, taking into account that each telescope is composed, in this case, by only two detector stages, the ΔE_2 and E_{CsI}.

3.1.2 Cross section angular distributions

The production cross section ($d\sigma/d\Omega$) angular distributions were determined from the measured fragment yields at each ϑ angle corrected for the acquisition system dead-time (N_{riv}) and normalized with respect to the target thickness (ρ), the number of incident carbon ions (N_{inc}), measured by a Faraday cup, and the total solid angle $\Delta\Omega$ covered by the detector. In formula:

$$\frac{d\sigma}{d\Omega} = \frac{N_{riv}}{N_{inc}\rho\Delta\Omega}. \tag{3.1.4}$$

The uncertainties in the cross sections resulted from propagating the statistical errors on the fragment yields and the uncertainties on the target thickness, the number of incident ions and the solid angle. Particularly, the uncertainties affecting the angular positions correspond to the half-widths of each telescope, being $\Delta\vartheta_{HS} \approx 0.36°$ and $\Delta\vartheta_{HB} \approx 1.43°$ for the Hodo-Small and the Hodo-Big detectors, respectively. Since, for most of the selected angles, more than one detector positioned at the same angle is available, errors on the yields estimate were determined as the standard deviations by the average counts. Otherwise, the yield errors were evaluated as $\Delta N_{riv} = \sqrt{N_{riv}}$. Moreover, the yields extracted from the Hodo-Small telescopes were corrected for the different solid angles subtended with respect to the Hodo-Big ones (see section 2.1.1).

As can be seen by Figures 3.1.5 and 3.1.6, the angular distributions were fitted with exponential functions in order to highlight their exponential drop.

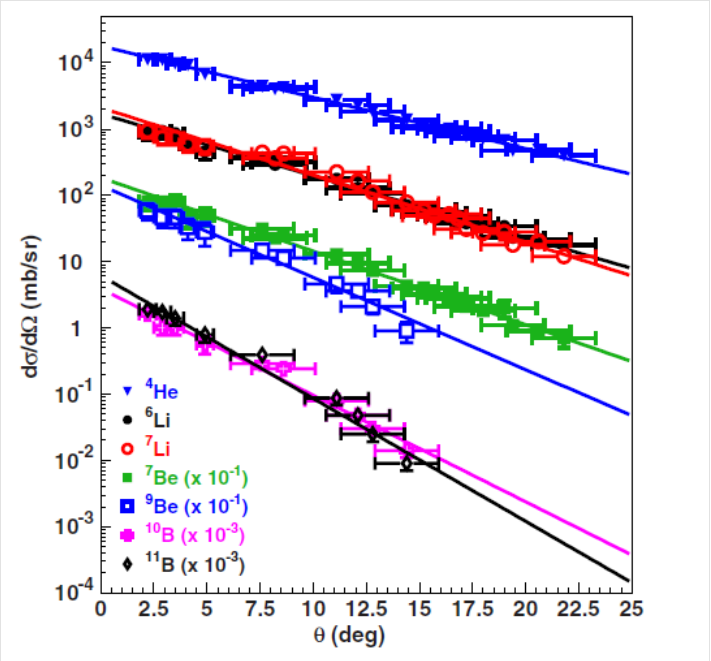

Figure 3.1.5: The production cross sections angular distributions for $Z > 1$ fragments together with exponential best-fits of the data (solid lines). The estimated angular uncertainties corresponds to the different telescope acceptances. Cross section values for the Be and B isotopes have been scaled by factors 10^{-1} and 10^{-3} respectively.

This trend clearly shows that secondary fragments are mostly emitted at forward angles. The main difference between the heavier and lighter fragments is represented by the corresponding angular distribution slopes, steeper in the first case. This means that the larger is the mass of the particle produced, the narrower is the emission angle with respect to the incident beam direction.

Moreover, the angular distributions show unambiguously that the larger fraction of the produced fragments, in the explored angular region, are α particles. As it is well known, because of their larger binding energy, α particles are very stable nuclei with respect to other light ones. This aspect may lead to clustering phenomena so that ^{12}C ion can be described as α-

cluster structures and the break-up of ^{12}C into three α particles is extremely probable.

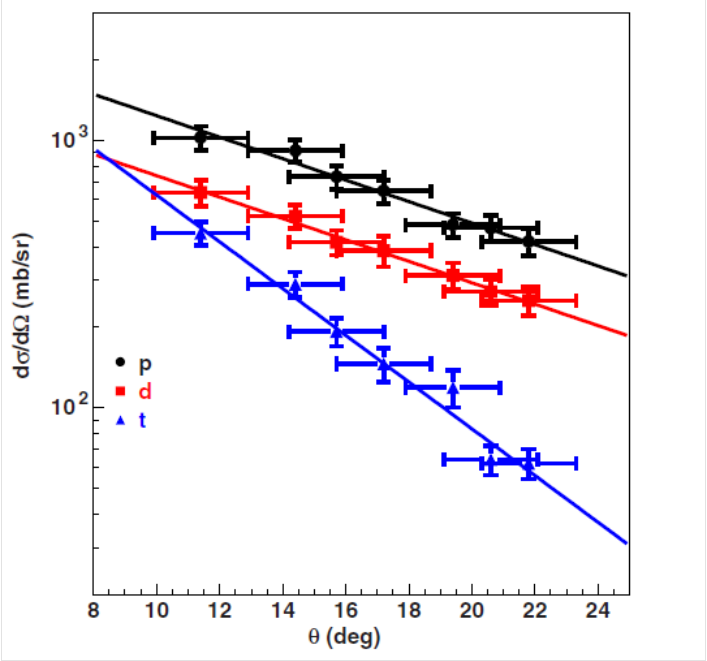

Figure 3.1.6: The production cross sections angular distributions for $Z = 1$ fragments together with exponential best-fits of the data (solid lines). The estimated angular uncertainties corresponds to the different telescope acceptances.

3.1.3 Double-differential cross sections: comparisons with GEANT4 models

The double-differential production cross sections were evaluated, dividing the equation (3.1.4) by the energy bin size. Concerning $Z > 1$ fragments, the double-differential cross sections for ^{4}He, ^{6}Li, ^{7}Li, ^{7}Be, ^{9}Be, ^{10}B, ^{11}B at different ϑ angles were determined.

As an example, in Figure 3.1.7, the ^{6}Li double-differential cross sections at four angles, $\vartheta = 2.2°$, $7.6°$, $14.4°$ and $18.0°$ are shown. As one can see from the figure, the energy distributions exhibit a Gaussian-like main peak, centered around the beam velocity (solid line) and a tail extending at lower energies. The main peak decreases and moves to lower energies as the emission angle increases. In contrast, the low-energy tail increases

with the angle, becoming the dominant part of the energy spectrum at large angles. The energy distributions of all the fragments with $Z > 1$ show a similar behavior. The presence of a Gaussian-like peak together with a low-energy tail in the fragment energy distributions has already been observed at intermediate energies [119] [120] [121] [122] [123] [124] [125]. The Gaussian-like peak can be associated with those fragments produced in peripheral collisions. Indeed, these fragments are emitted at approximately the same velocity of the beam and in a relatively small angular cone around the beam direction. On the other hand, the fragments emitted at large angles and at velocities much lower than the beam are most probably produced in more central and dissipative collisions than the ones producing high-energy fragments.

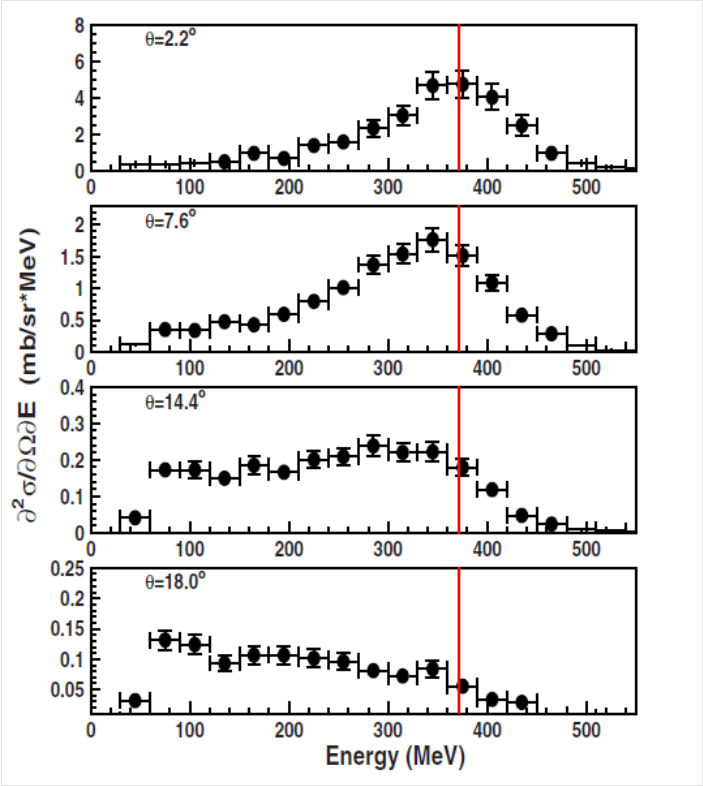

Figure 3.1.7: The ^{6}Li double-differential cross sections estimated at four angles: ϑ = 2.2°, 7.6°, 14.4° and 18.0°. The solid line refers to the kinetic energy of ^{6}Li moving at the beam velocity, i.e. around 372 MeV (being $\beta_{beam} \approx 0.35$).

A quite different shape marks the $Z = 1$ (protons, deuterons and tritons) double-differential cross sections, as shown in Figure 3.1.8 for the case of protons at four angles $\vartheta = 11.4°$, $14.4°$, $17.2°$ and $19.4°$.As can be seen from the figure, the energy distributions fall off exponentially as the energy increases. A similar behavior has been also observed in other works where the $Z = 1$ particles have been assumed to be isotropically emitted from one or more moving sources and their energy distributions have been commonly reproduced with a *moving source fit* [126] [127].

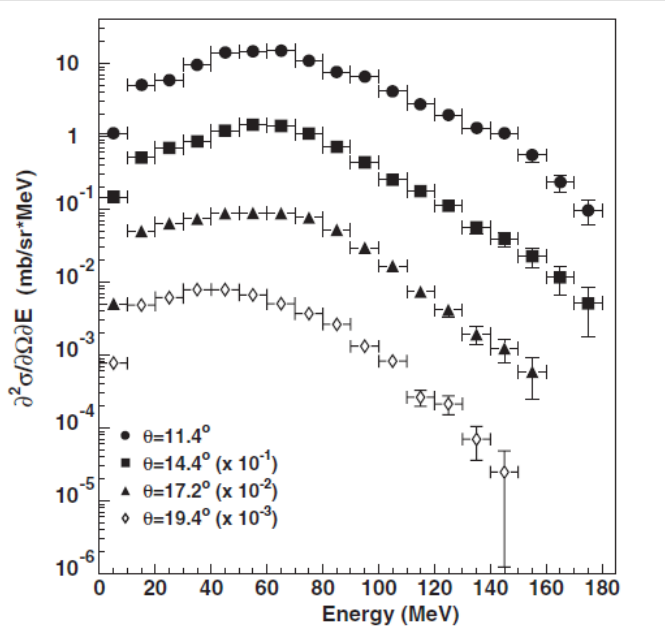

Figure 3.1.8: The protons double-differential cross sections measured at four angles: $\vartheta = 11.4°$, $14.4°$, $17.2°$ and $19.4°$. Cross sections at $\vartheta = 14.4°$, $17.2°$ and $19.4°$ are scaled by the factors 10^{-1}, 10^{-2} and 10^{-3} respectively.

The measured cross sections were used to evaluate the performance of the nuclear reaction models implemented in GEANT4 [57] in the region of intermediate energies and in the optimum experimental condition of a thin target. GEANT4 is an object-oriented toolkit to simulate the passage of particles through matter. It is currently used in a variety of physics domains, including medical physics, since it provides interaction models for electromagnetic and nuclear processes involved in the transport of therapeutic ion beams.

Nucleus-nucleus collisions, pre-equilibrium and de-excitation stages can be described by different models in GEANT4. At present, two models are potentially able to provide a realistic description of light-ions inelastic interactions in the energy range of interest for this work: `G4BinaryLightIonReaction`[1] and `G4QMDReaction`[2].

The `G4BinaryLightIonReaction` model is based on the Binary Cascade approach (BIC) [128]. Although the suggested energy range of the model is 80 AMeV-10 AGeV, its reference physics lists implement the model down to zero energy.

`G4QMDReaction` is a new native GEANT4 implementation [129] of the general Quantum Molecular Dynamic model (QMD) [130] [131]. The set of parameters in the QMD model were originally optimized to reproduce data in the energy range between 100 AMeV and 3 AGeV. In order to test the QMD model in the energy range of interest for this work, the reference physics list had to be manually edited with respect to the version provided with GEANT4. More details on both models can be found in Appendix A (4.6).

The simulations reported in this work were performed by the user group of GEANT4 at LNS-INFN by using the version 9.4.p01 of the code. In particular, in the simulation both the ^{12}C beam spot and the energy straggling in the target were considered. In order to reduce the calculation time of the simulation, the inelastic interaction cross section of the ions was artificially increased by a factor of 100. The scaling factor was chosen such that the thin-target approximation is still valid, namely the probability of having two or more inelastic interactions within the target remains negligible. A total statistic of a few 10^{12} events was generated for each of the two physics models considered. Finally, the results of the simulations were processed by an analytical algorithm to reproduce angular resolution, geometrical efficiency, energy resolution and energy thresholds of the detectors.

Figures 3.1.9 - 3.1.15 show the comparison between the double-differential cross sections of the $Z > 1$ fragments with the BIC (dashed lines) and the QMD (solid lines) model predictions at different emission angles.

Since the experimental results were compared with the code predictions for many different isotopes in a wide angular range, some general conclusions can be drawn for the two models. As one can see, e.g., from Figure

[1] http://geant4.cern.ch/support/proc_mod_catalog/models/hadronic/G4BinaryLightIonReaction.html

[2] http://geant4.cern.ch/support/source/geant4.9.5/source/processes/hadronic/models/qmd/src/G4QMDReaction.cc

3.1.9, the BIC model better reproduces the cross sections of the fragments emitted at high energies and small angles, i.e. the fragments produced in peripheral collisions, rather than those of the fragments emitted at low energies. A possible explanation could be that in the BIC model a time-invariant optical potential is used. Indeed, this approach seems to be more appropriate for treating peripheral reactions, where the dynamical evolution of the potential is slightly affected by the nucleon scatterings, with respect to the central ones. Moreover, the BIC model assumption that the participant nucleons, i.e. nucleons in the projectile and the ones scattered in the cascade, cannot collide with each other may have a minor effect on the description of peripheral reactions than the central ones. As has been pointed out in [128], the BIC applicability is limited to small participant densities.

In contrast, the QMD model better reproduces the low-energy part of the spectra, i.e. the fragments produced in more dissipative central collisions. Indeed, in the QMD model, unlike the BIC, all nucleons, tracked simultaneously, can collide to each other and the potential dynamically changes along with the time evolution of the nucleons. Based on these assumptions, the QMD model seems to be more suitable to describe central reactions where the participant-participant collisions and the dynamical evolution of the potential become more important.

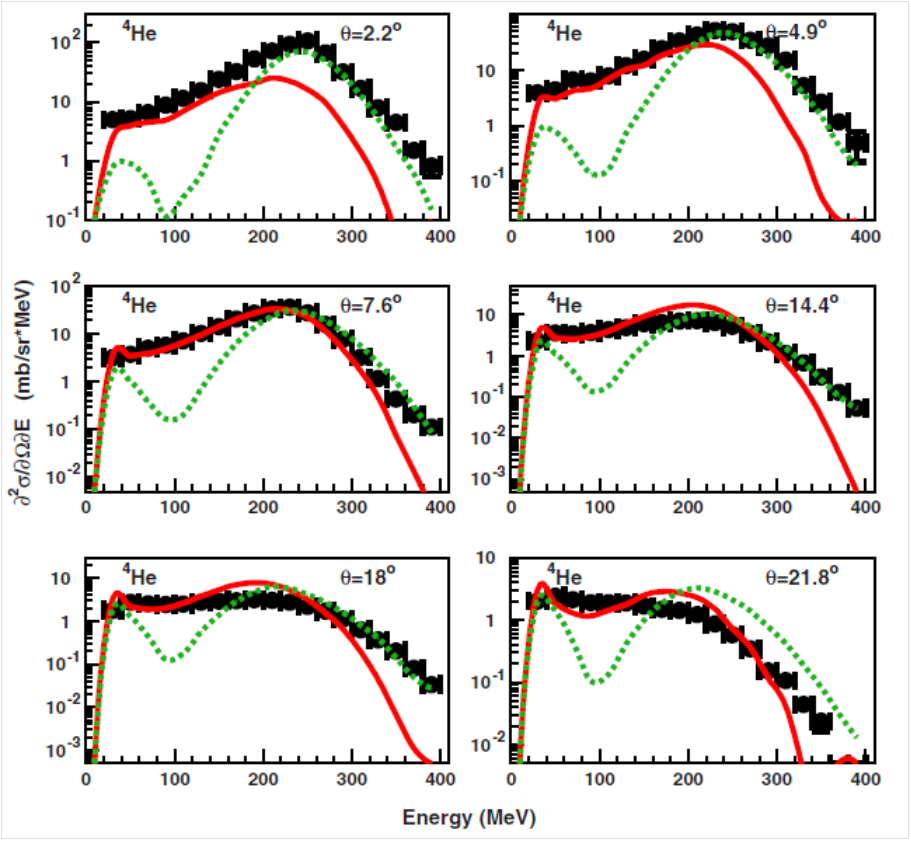

Figure 3.1.9: Double differential cross-sections for ^{4}He measured at six different ϑ angles in the ^{12}C + ^{12}C reaction performed at 62 AMeV incident energy. Experimental data are compared with the two nucleus-nucleus reaction models, BIC (dashed lines) and QMD (solid lines), implemented in GEANT4 Monte Carlo code.

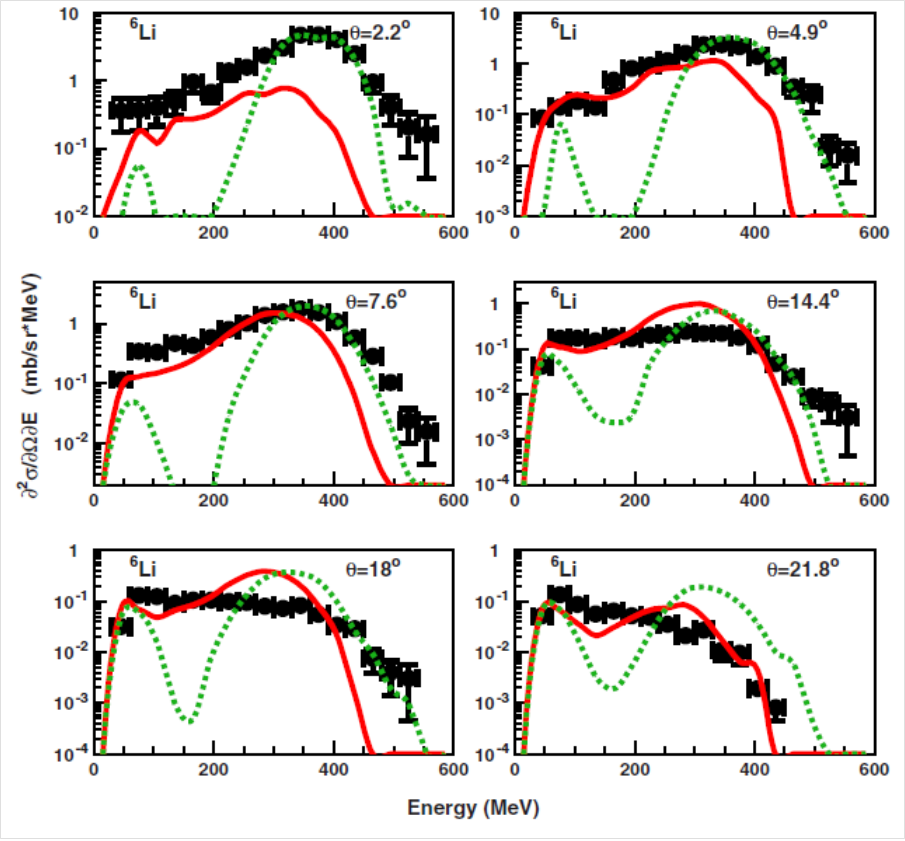

Figure 3.1.10: Double differential cross-sections for ^{6}Li measured at six different ϑ angles in the ^{12}C + ^{12}C reaction performed at 62 AMeV incident energy. Experimental data are compared with the two nucleus-nucleus reaction models, BIC (dashed lines) and QMD (solid lines), implemented in GEANT4 Monte Carlo code.

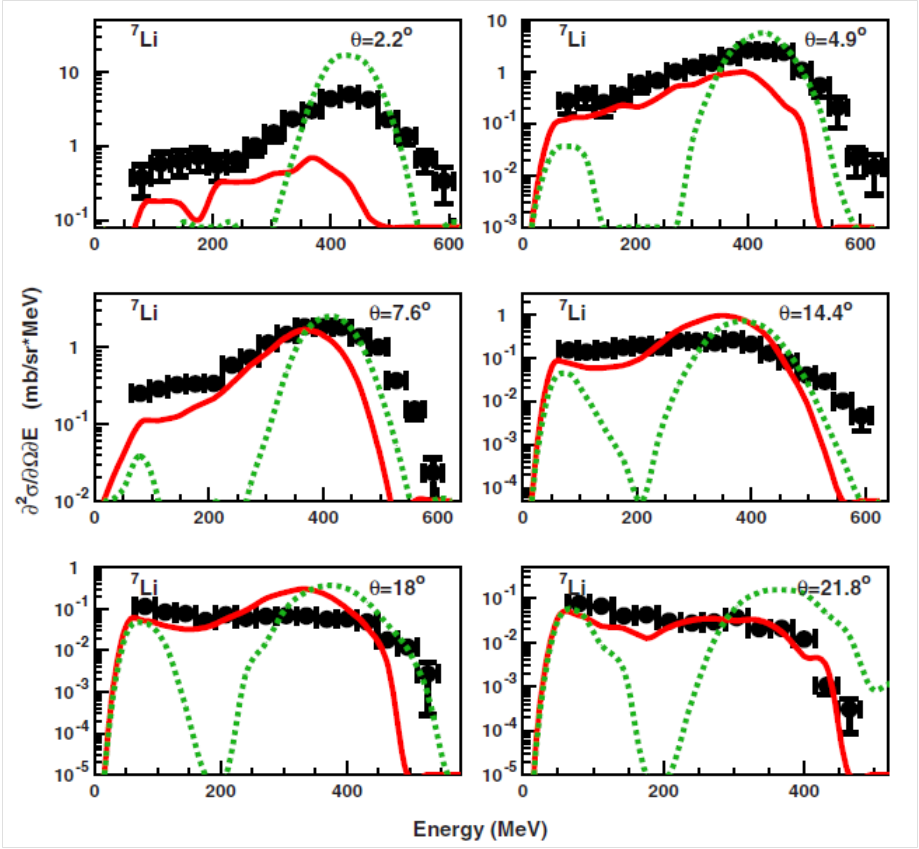

Figure 3.1.11: Double differential cross-sections for ^{7}Li measured at six different ϑ angles in the ^{12}C + ^{12}C reaction performed at 62 AMeV incident energy. Experimental data are compared with the two nucleus-nucleus reaction models, BIC (dashed lines) and QMD (solid lines), implemented in GEANT4 Monte Carlo code.

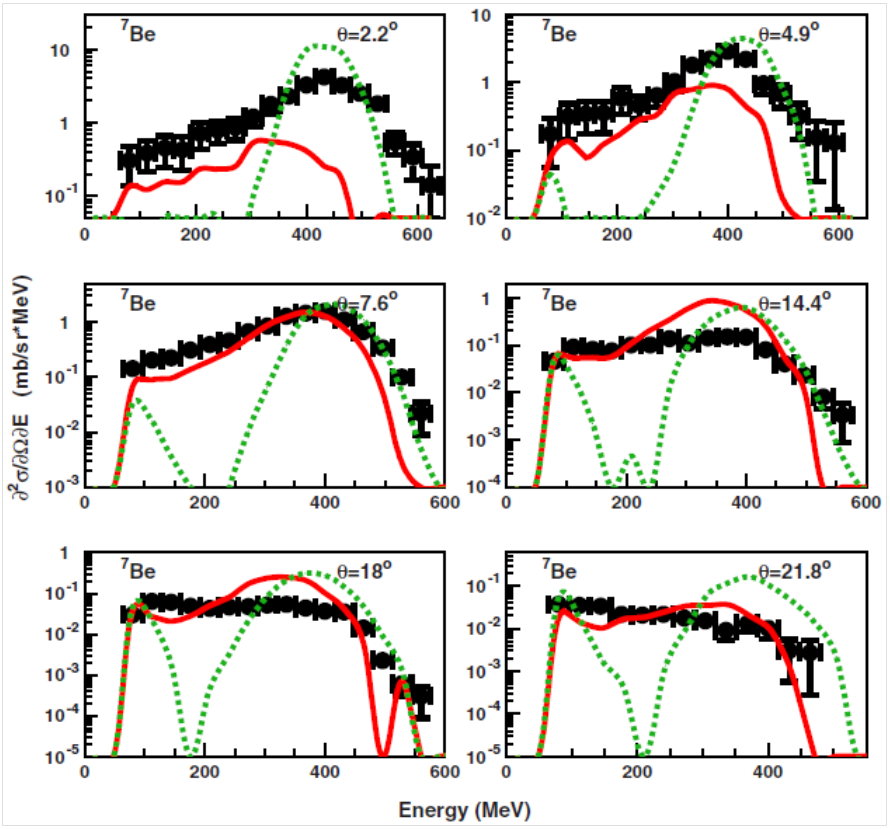

Figure 3.1.12: Double differential cross-sections for ^{7}Be measured at six different ϑ angles in the ^{12}C + ^{12}C reaction performed at 62 AMeV incident energy. Experimental data are compared with the two nucleus-nucleus reaction models, BIC (dashed lines) and QMD (solid lines), implemented in GEANT4 Monte Carlo code.

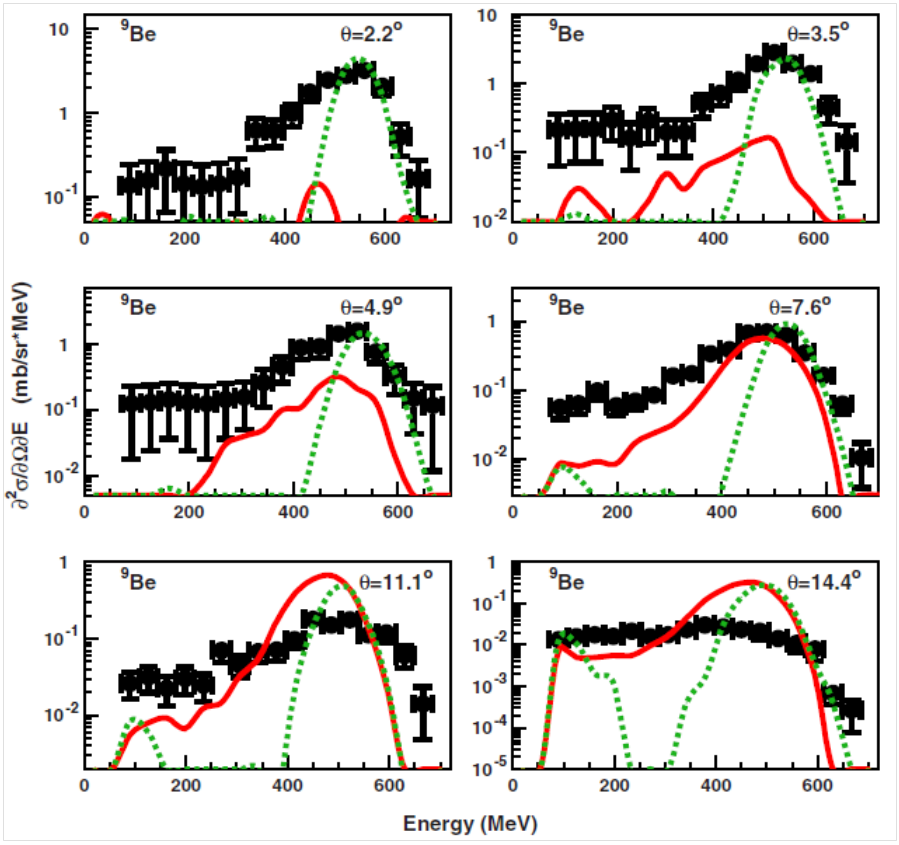

Figure 3.1.13: Double differential cross-sections for ^{9}Be measured at six different ϑ angles in the ^{12}C + ^{12}C reaction performed at 62 AMeV incident energy. Experimental data are compared with the two nucleus-nucleus reaction models, BIC (dashed lines) and QMD (solid lines), implemented in GEANT4 Monte Carlo code.

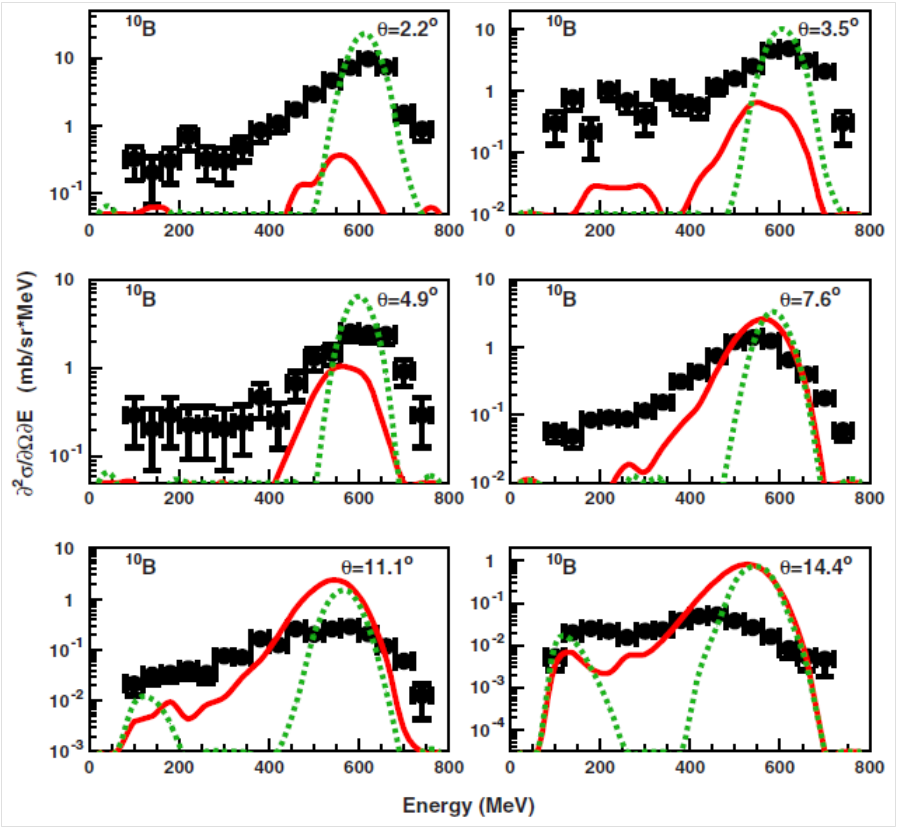

Figure 3.1.14: Double differential cross-sections for ^{10}B measured at six different ϑ angles in the ^{12}C + ^{12}C reaction performed at 62 AMeV incident energy. Experimental data are compared with the two nucleus-nucleus reaction models, BIC (dashed lines) and QMD (solid lines), implemented in GEANT4 Monte Carlo code.

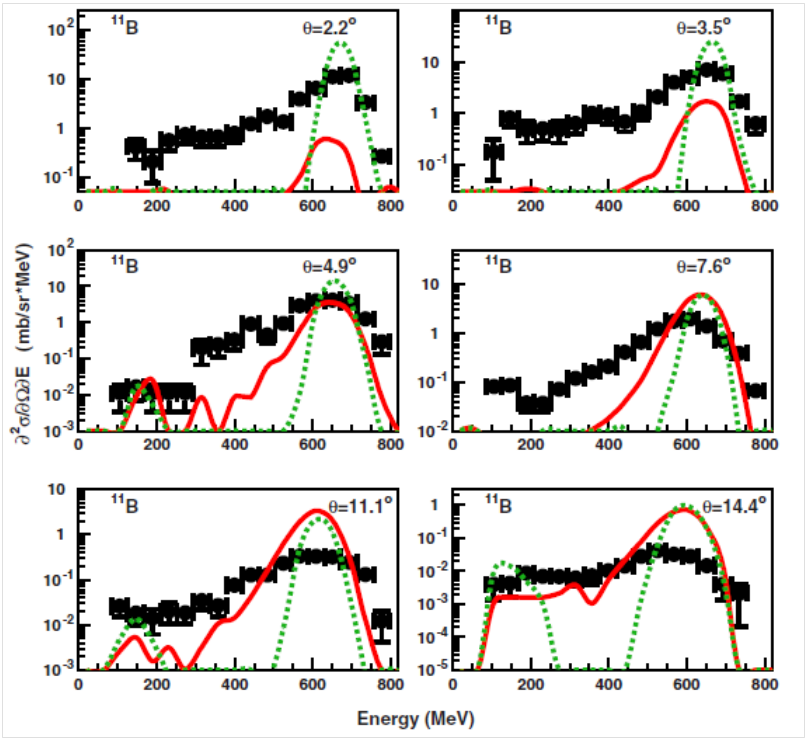

Figure 3.1.15: Double differential cross-sections for ^{11}B measured at six different ϑ angles in the ^{12}C + ^{12}C reaction performed at 62 AMeV incident energy. Experimental data are compared with the two nucleus-nucleus reaction models, BIC (dashed lines) and QMD (solid lines), implemented in GEANT4 Monte Carlo code.

In Figures 3.1.16 - 3.1.18, the double-differential cross sections of the $Z = 1$ isotopes were compared with the BIC (dashed lines) and the QMD (solid lines) predictions. As has been observed in the $Z > 1$ cases, the high-energy region of the distributions at small angles is better reproduced by the BIC model rather than the QMD.

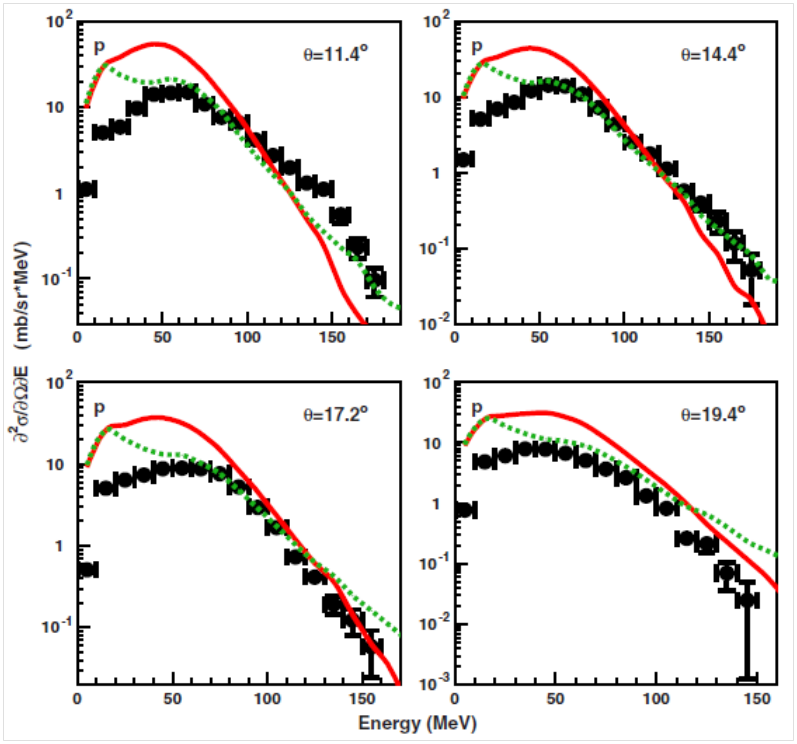

Figure 3.1.16: Double differential cross-sections for protons measured at four different ϑ angles in the $^{12}C + {}^{12}C$ reaction performed at 62 AMeV incident energy. Experimental data are compared with the two nucleus-nucleus reaction models, BIC (dashed lines) and QMD (solid lines), implemented in GEANT4 Monte Carlo code.

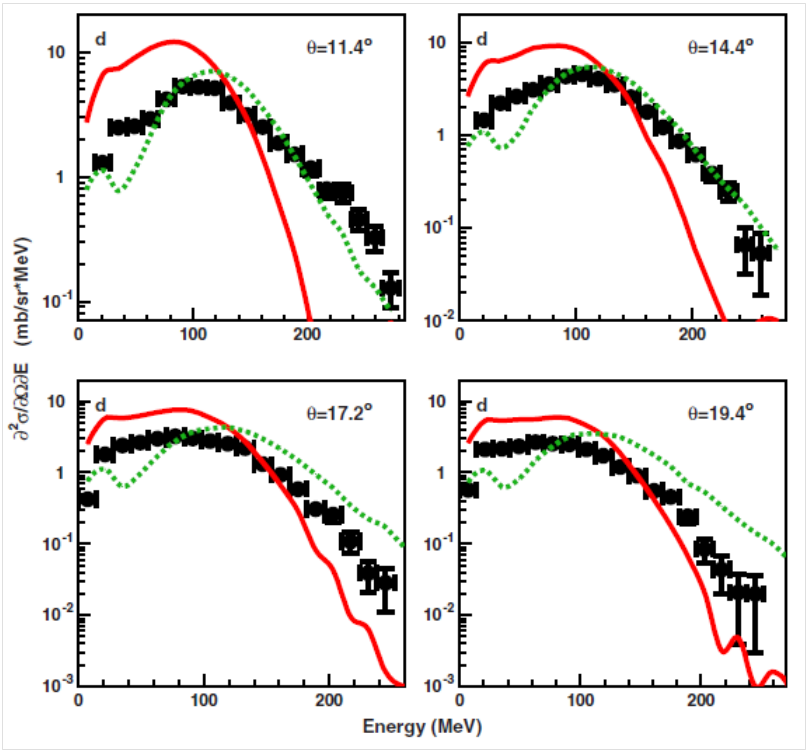

Figure 3.1.17: Double differential cross-sections for deuterons measured at four different ϑ angles in the $^{12}C + ^{12}C$ reaction performed at 62 AMeV incident energy. Experimental data are compared with the two nucleus-nucleus reaction models, BIC (dashed lines) and QMD (solid lines), implemented in GEANT4 Monte Carlo code.

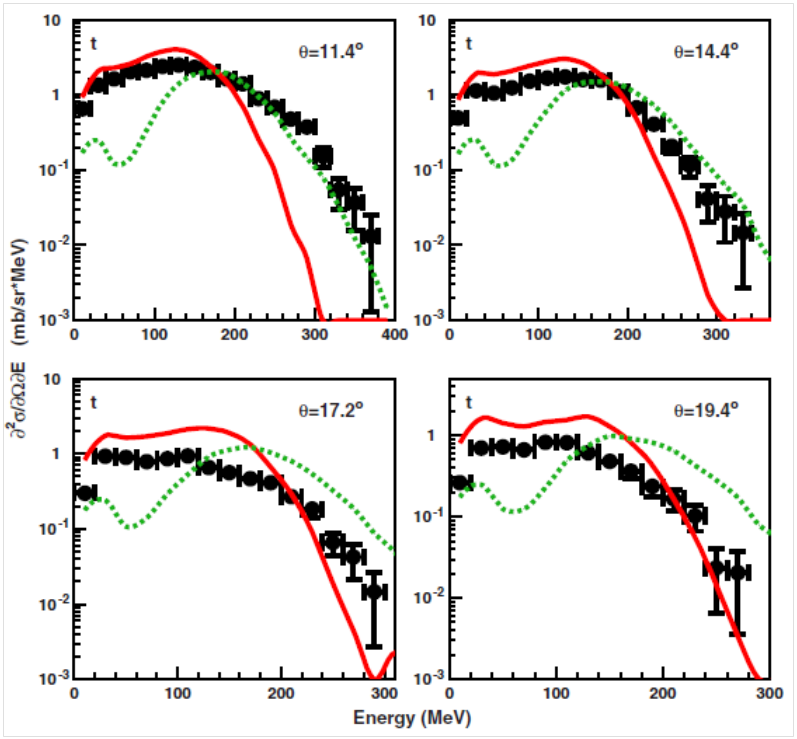

Figure 3.1.18: Double differential cross-sections for tritons measured at four different ϑ angles in the $^{12}C + ^{12}C$ reaction performed at 62 AMeV incident energy. Experimental data are compared with the two nucleus-nucleus reaction models, BIC (dashed lines) and QMD (solid lines), implemented in GEANT4 Monte Carlo code.

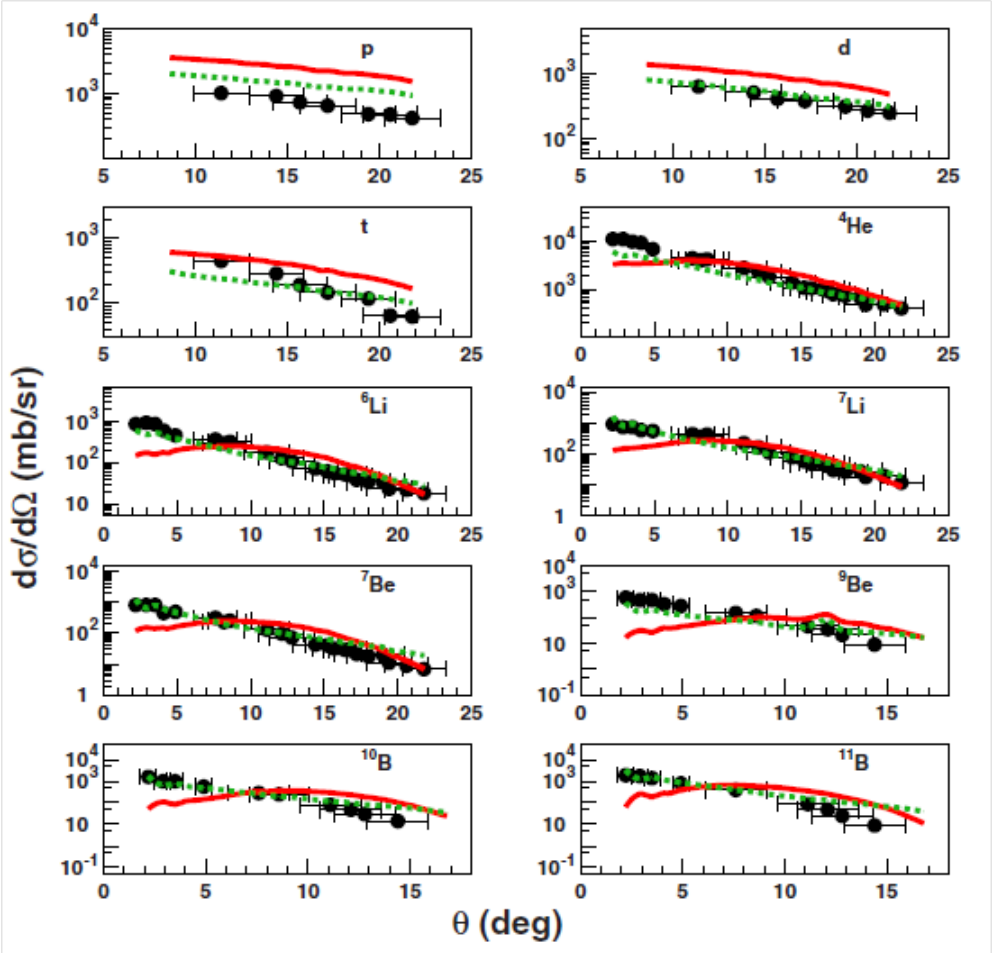

Figure 3.1.19: Data-Monte Carlo simulation comparisons for differential cross sections with respect to the emission angle determined for all the fragments detected in the $^{12}C + {}^{12}C$ reaction performed at 62 AMeV incident energy. Dashed lines refer to the BIC predictions, while the solid lines to the QMD ones.

The comparison between the experimental angular distributions of all fragments and the two model predictions are shown in Figure 3.1.19. As one can clearly see, the angular distributions of the fragment production cross sections are better approximated by the BIC calculations than by the QMD ones. Large discrepancies between the experimental cross sections and both model predictions can be observed. Indeed, differences up to a factor of 5 have been found in the comparison with the BIC calculations, whereas

discrepancies up to one order of magnitude have been obtained between the experimental data and the QMD.

In particular, for the $Z > 1$ fragments, the experimental production cross sections are underestimated at most forward angles by the QMD and overestimated at larger angles by both models. As has been observed from the comparison between the double-differential cross sections and the calculations (see, e.g., Figure 3.1.9), at most forward angles the contribution predicted by the QMD to the high-energy part of the energy distributions is smaller than the experimental cross section. On the other hand, at larger angles, both BIC and QMD predict a Gaussian-like peak that is not present in the experimental data (see, e.g., Figure 3.1.13).

It is interesting to observe how similar results were obtained in Böhlen et al. [67], where the performances of both GEANT4 nuclear fragmentation models, BIC and QMD, were investigated for carbon ions incident energies between 100 and 500 AMeV. Also in Böhlen et al., for both models, the fragmentation yields tend to be underestimated at small angles, while at larger angles the trend is to overestimate the produced fragments, especially for the heavier ones. Nevertheless, the conclusion drawn by Böhlen et al. is that the QMD model is preferable over the BIC for a better fragments yields prevision. In the present work the QMD capability of reproducing experimental data is found to be worse than BIC, probably because the QMD model is designed to work properly in a higher energy range (over 100 AMeV) with respect to the energy at which the fragmentation measurements analyzed in the present work were performed.

Essentially, the comparison between experimental cross sections and GEANT4 predictions show a modest agreement, then the predictive ability of both Monte Carlo models implemented in the transport code needs to be improved at intermediate energies, in order to make them suitable for carbon ion therapy applications. Actually, it is still necessary to perform further high-quality and systematic measurements of double-differential cross sections for improving and validating nuclear interactions models in the energy range of interest for hadrontherapy purposes.

Specifically, Monte Carlo codes are employed for computing fluences and dose distribution in patients both for proton and ion beam therapy. Even though these codes are generally not used for treatment planning optimization, as they are currently too time consuming, they represents very useful tools for dose verification of analytical treatment planning codes and their models can be used to complement experimental data of physical quantities as input for treatment planning codes [132].

Moreover, the accessibility of double-differential cross sections in the intermediate energies range is important, not only for predicting the fluences of secondary fragments and their angular distributions inside biological tissues, but also to correctly describe the inelastic processes associated with the slowing down of carbons through the patient body. Due to the very limited experimental fragmentation data presently available in literature, in the next sections other combinations of incident carbons energies and targets will be studied and the analysis results will be discussed.

3.2 Thick targets measurements

The experimental results discussed in the previous sections, concerning carbon fragmentation on a thin carbon target, represent the optimal input information requested for benchmarking the nuclear reaction models embedded in the Monte Carlo simulation code GEANT4. In order to reproduce accurately the fragments build-up in an experimental condition closer to the real case of irradiating a patient, the most suitable choice is to study carbon interaction at atmospheric pressure with thicker targets, whose chemical composition is very similar to the actual composition of the human body.

This idea is the basis for the FRATT experiment (see section 2.2), performed at the INFN-LNS by a 62 AMeV carbon beam impinging on different tissue-equivalent targets (PMMA and lung). The purpose was to extract the secondary fragments yields, as a function of the target thickness, and the associated energy distributions measured at $\vartheta = 0°$.

Concerning fragmentation data for carbon therapy development already available in literature, it should be noted that they refers mostly to thick targets experiments, while the thin target case has been poorly investigated, as already mentioned in the previous sections. More precisely, many experiments have been performed by accelerating carbon ions beams in the energy range from 200 to 400 AMeV on thick water, PMMA ($C_5H_8O_2$) or polycarbonate ($C_{16}H_{14}O_3$) targets both in Japan, at the Chiba and Hyogo treatment centers [133], [134], and in Germany, at the GSI biophysics department [135] [136]. Recently, another experiment took place in France at GANIL[3] with a 95 AMeV ^{12}C beam on thick PMMA targets aiming to measure the production rates, the energy and the angular distributions of the detected fragments [137].

Three aspects characterize the FRATT experiment, discussed in this section, with respect to those performed so far: the lower beam energy, but

[3]Grand Accélérateur National d'Ions Lourds.

still useful for carbon therapy applications, the use of specifically prepared targets to reproduce particular human organs tissues, such as lung, and the positioning of the charged fragments detector at zero degrees, i.e. along the incident beam direction. Particularly, the chosen lung tissue equivalent targets are produced by GAMMEX [138], a manufacturing expert of advanced materials, which replicate human body, and devices for diagnostic imaging and radiation oncology. The lung-equivalent targets were provided along with their exact chemical composition, given in Table 3.1, in terms of its constituents mass fractions[4].

Target	**Density [g/cm^3]**	**Element (mass fraction)**
Lung	0.300	H (0.0846), C (0.5938), N (0.0196), O (0.1814), Mg (0.1119), Si (0.0078), Cl (0.0010)

Table 3.1: Lung tissue equivalent targets composition provided by GAMMEX [138].

These were also fundamental input information for the GEANT4 user group at LNS-INFN for correctly simulating both the fragments yields and their energy distributions. The data analysis results have been compared with the simulated ones for testing the Monte Carlo code predictive ability in an experimental condition completely different from the previous ones.

3.2.1 Detector calibration

The energy, charge and mass calibration procedures of the ΔE-E$_{res}$ telescope, employed for detecting the produced fragments, are very similar to those already reported in section 3.1.1 for a single hodoscope element, so that they will be briefly addressed. In Figure 3.2.1 a not calibrated ΔE-E$_{res}$ matrix related to the carbon beam interaction with the 3.28 mm thick PMMA target is shown.

The first calibration step consisted in estimating the linear relatioship between the energy deposited by ^{12}C ions and fragments inside the ΔE silicon detector and the ADC channels. As it is known, this relationship is independent from the charge Z and mass A of the incident particle. As a consequence, the silicon calibration can be uniquely determined placing at least two reference point with known energies in the ΔE channels spectrum.

[4]Mass fraction is defined as the mass of a constituent divided by the total mass of all constituents in a mixture [139].

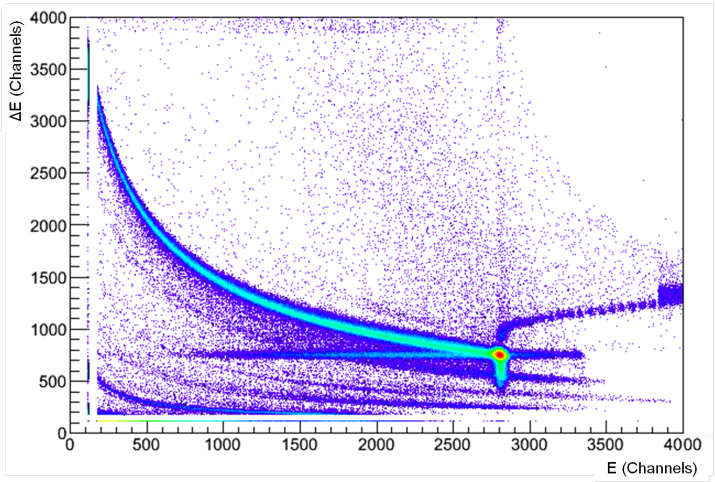

Figure 3.2.1: ΔE-E$_{res}$ scatter plot related to the ^{12}C ions interacton with the 3.28 mm thick PMMA target.

For this purpose, the ^{12}C ions of the primary beam, which slow down inside the target thickness and hit the detector, were selected. These are good events for calibration, since carbons energy loss is due only to electromagnetic interactions with the target atoms and can be accurately computed by means of dedicated software tools as LISE [140] and SRIM [141], or simulated by means of Monte Carlo codes like GEANT4 [57], [58]. Moreover, being the ΔE-E$_{res}$ telescope placed at 0° with respect to the beam direction, the most part of the detected carbons experienced sequential electromagnetic collisions with the target atoms giving rise to a sharp peak in the silicon channels spectrum.

In order to precisely determine the linear correlation between deposited energy and channel value, the PMMA target together with the four different lung-equivalent targets were used. For each of them the experimental peak value and the standard deviation were determined by means of a Gaussian fit of the silicon ADC spectrum. The same procedure were applied for estimating the corresponding fit parameters relative to the GEANT4 simulated spectra. Thus the silicon energy calibration were evaluated through a *linear best fit* of the channel values and the correspondent simulated energy values.

Concerning the isotopes identification and CsI(Tl) energy calibration, the same procedures already treated in section 3.1.1 were applied. The total

kinetic energy released by fragments in the ΔE-E$_{res}$ detector was determined with an estimated error around 8%. In Figure 3.2.1 a calibrated ΔE-E$_{res}$ matrix is shown.

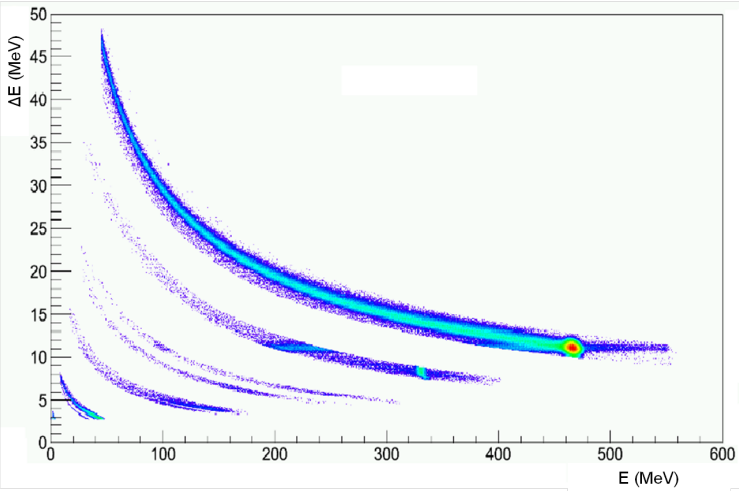

Figure 3.2.2: ΔE-E$_{res}$ matrix after applying the complete procedures of energy calibration and isotopes identification.

3.2.2 Fragments energy spectra

In the following, the detected fragments energy spectra are shown. The production yields for each isotope have been corrected for the acquisition system dead time and normalized with respect to the total incident ^{12}C ions. Due to the very small energy released by the $Z = 1$ (protons, deuterons and tritons) and $Z = 2$ (^{3}He and ^{4}He) particles, the associated signal amplitudes produced in the ΔE silicon detector were comparable to the intrinsic electronic noise, so that it was impossible to extract the corresponding yields. Furthermore, the carbon beam contamination prevented also for the correct identification of the $Z = 5$ (^{10}B and ^{11}B) fragments, which also could not be analysed. The energy spectra related to the ^{6}Li, ^{7}Li, ^{7}Be and ^{9}Be isotopes produced in the interaction of the carbon beam with the 3.28 mm thick PMMA target are shown in Figures 3.2.3 and 3.2.4.

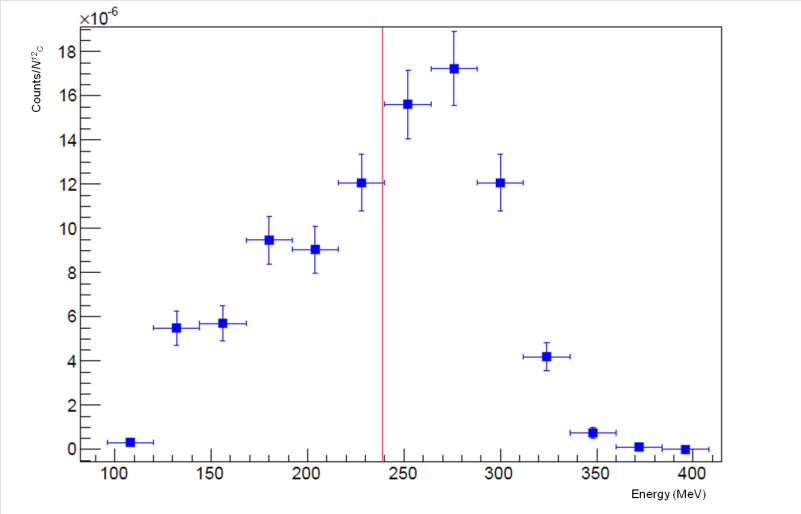

(a)

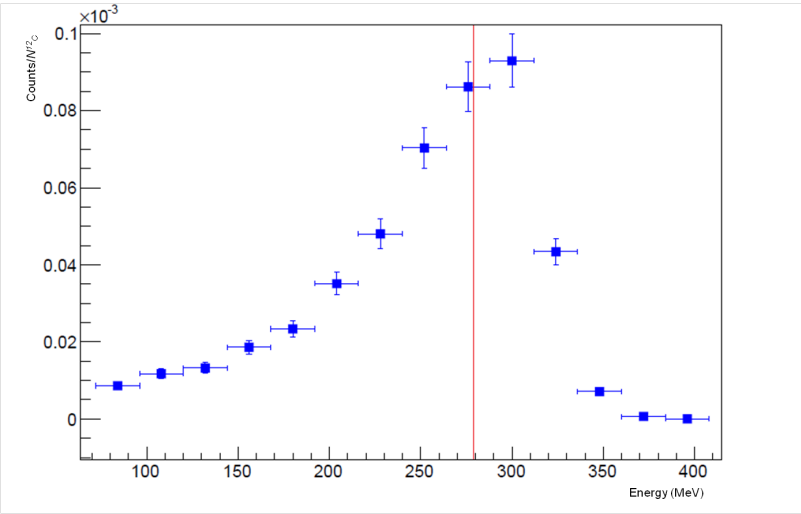

(b)

Figure 3.2.3: (a), (b): ^{6}Li and ^{7}Li energy spectra associated to carbon fragmentation on the 3.28 thick PMMA target. The expected ^{6}Li and ^{7}Li energies are also displayed (red lines).

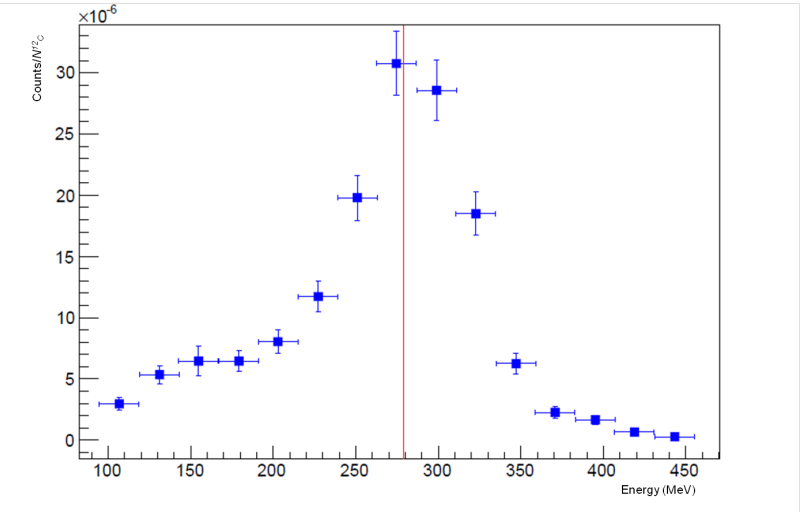

(a)

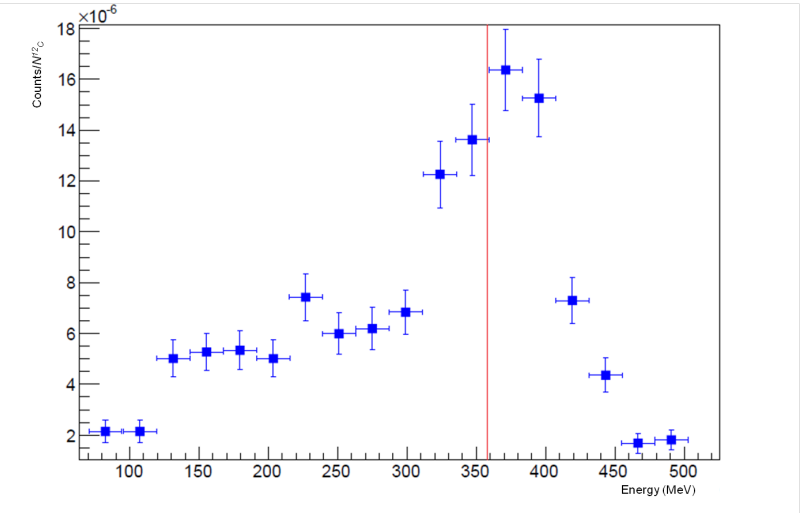

(b)

Figure 3.2.4: (a), (b): ^{7}Be and ^{9}Be energy spectra associated to carbon fragmentation on the 3.28 thick PMMA target. The expected ^{7}Be and ^{9}Be energies are also displayed (red lines).

It has to be noted that carbons slow down in air and lose energy also in the plastic scintillator and in the target thickness. Taking into account of these energy losses, it was estimated a ^{12}C ions residual energy of about 476 MeV. The energy loss was accurately computed by means of dedicated software tools as LISE [140] and SRIM [141]. Then the expected *projectile-like* fragments energies were also calculated and displayed. The uncertainties on the fragments yields were determined by propagating the errors on the number of counts, on the dead time and on the total number of incident carbon ions. As it has been already observed for the thin target measurements, the energy spectra show a main peak centered around the beam energy per nucleon, associated to peripheral collisions, and a low energy tail, associated to more central collisions, as expected.

3.2.3 GEANT4 BIC model validation

In order to test the perfomances of the GEANT4 BIC nuclear reaction model (see Appendix A), for the specific case of carbon interaction with a thick target, the experimental energy spectra were compared to those obtained by the GEANT4 code. The comparisons done for the ^{6}Li, ^{7}Li, ^{7}Be and ^{9}Be ejectiles produced in the interaction of the carbon beam with the 3.28 mm thick PMMA target and with the 3.12 mm, 5.81 mm, 10.3 mm and 20,6 mm thick lung-equivalent targets are shown, respectively, in Figures from 3.2.5 to 3.2.14.

As can be seen, GEANT4 BIC model reproduce fairly well the shapes of the experimental energy spectra but, in most cases, it underestimates the fragment yields. Particularly, the ability to predict the produced fragments is worse for ^{7}Li but it seems to get better for the other isotopes, especially for ^{7}Be. Moreover, the most probable energy for all fragments decreases with increasing the lung target thickness, as expected.

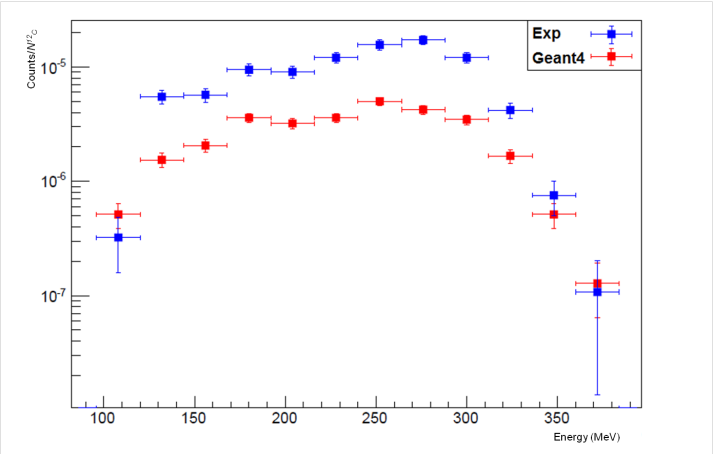

(a)

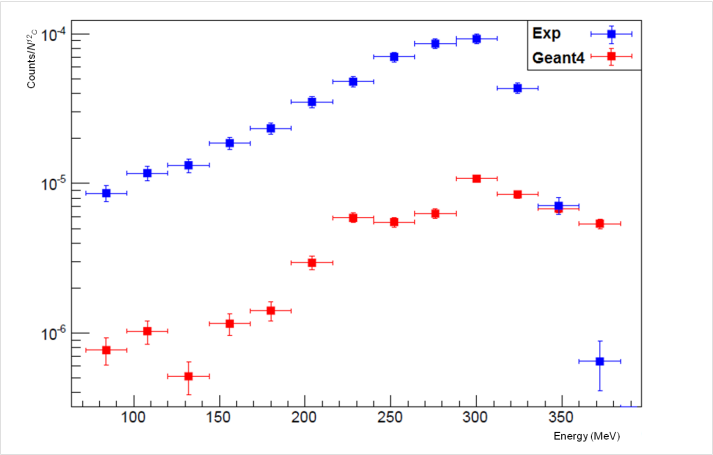

(b)

Figure 3.2.5: (a), (b): Data-Monte Carlo simulation comparisons for the ^{6}Li and ^{7}Li energy spectra associated to carbon fragmentation on the 3.28 mm thick PMMA target (color online).

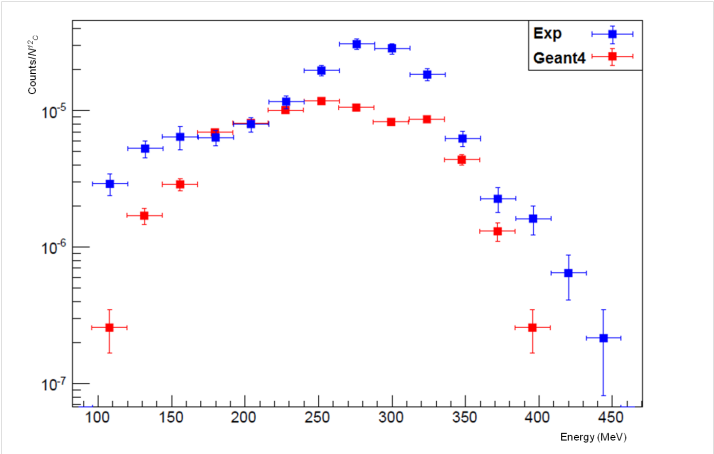

(a)

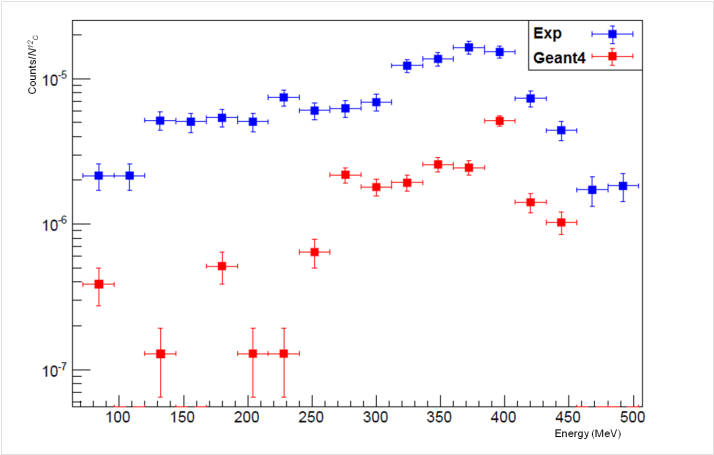

(b)

Figure 3.2.6: (a), (b): Data-Monte Carlo simulation comparisons for the ^{7}Be and ^{9}Be energy spectra associated to carbon fragmentation on the 3.28 mm thick PMMA target (color online).

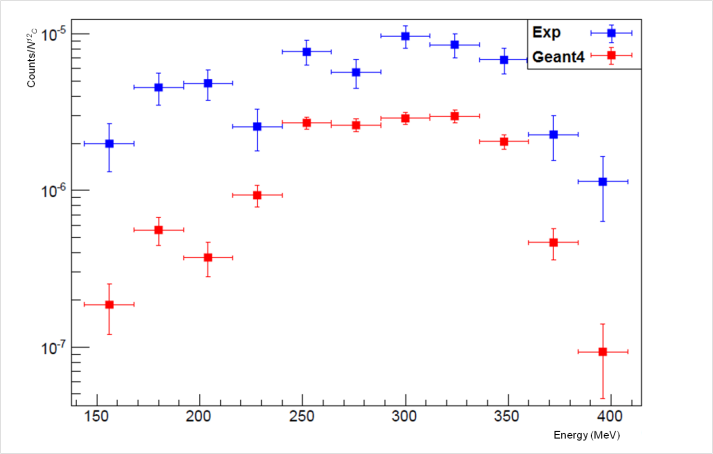

(a)

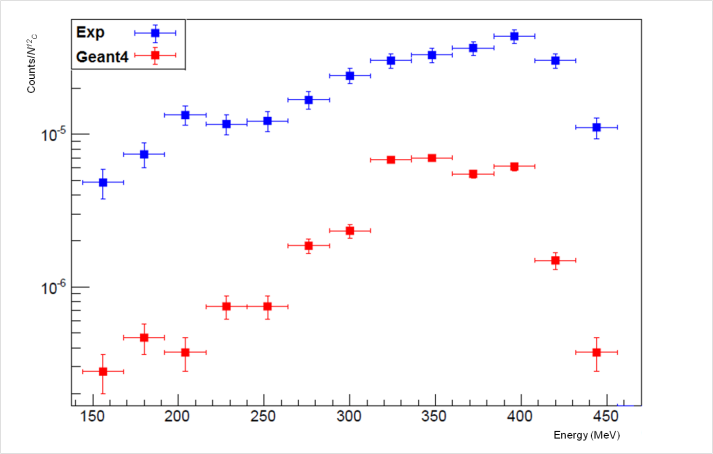

(b)

Figure 3.2.7: (a), (b): Data-Monte Carlo simulation comparisons for the ^{6}Li and ^{7}Li energy spectra associated to carbon fragmentation on the 3.12 mm thick lung-equivalent target (color online).

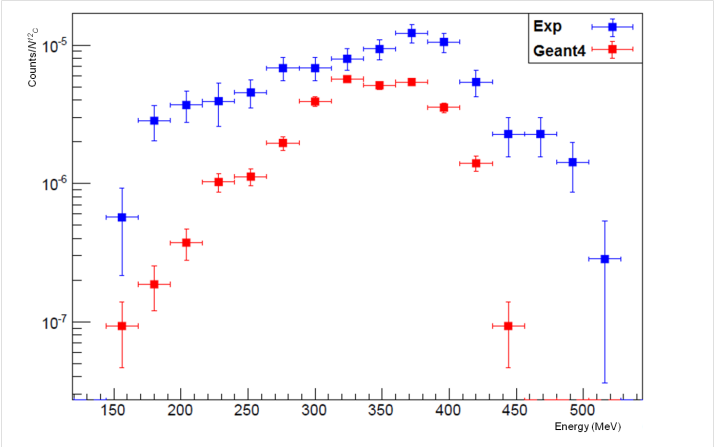

(a)

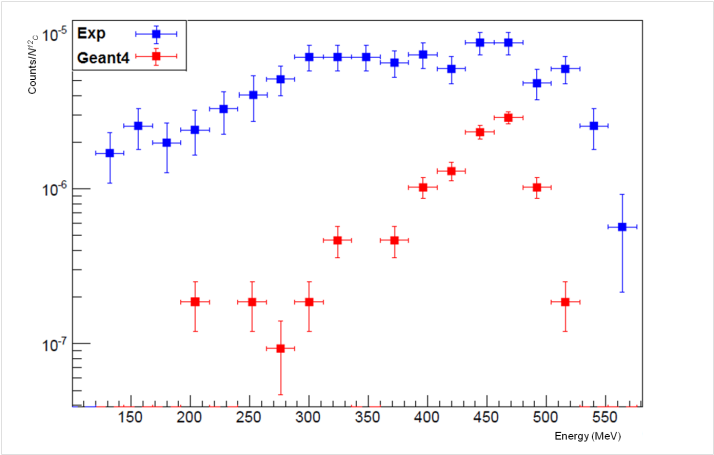

(b)

Figure 3.2.8: (a), (b): Data-Monte Carlo simulation comparisons for the ^{7}Be and ^{9}Be energy spectra associated to carbon fragmentation on the 3.12 mm thick lung-equivalent target (color online).

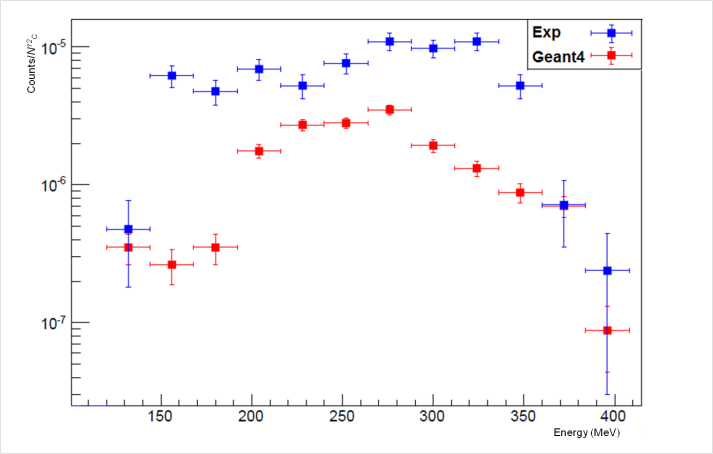

(a)

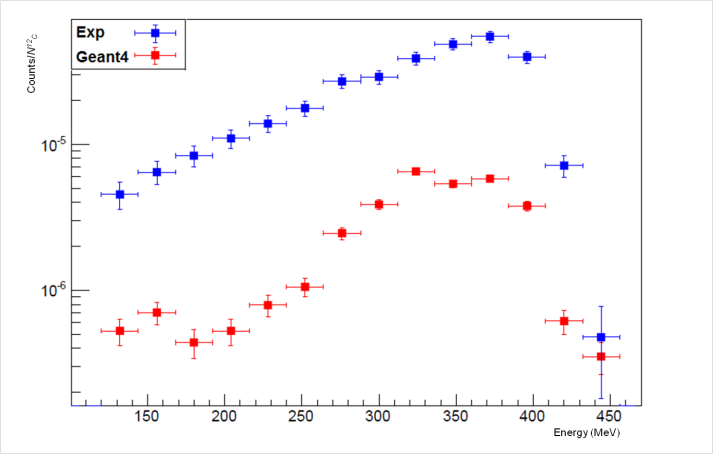

(b)

Figure 3.2.9: (a), (b): Data-Monte Carlo simulation comparisons for the ^{6}Li and ^{7}Li energy spectra associated to carbon fragmentation on the 5.81 mm thick lung-equivalent target (color online).

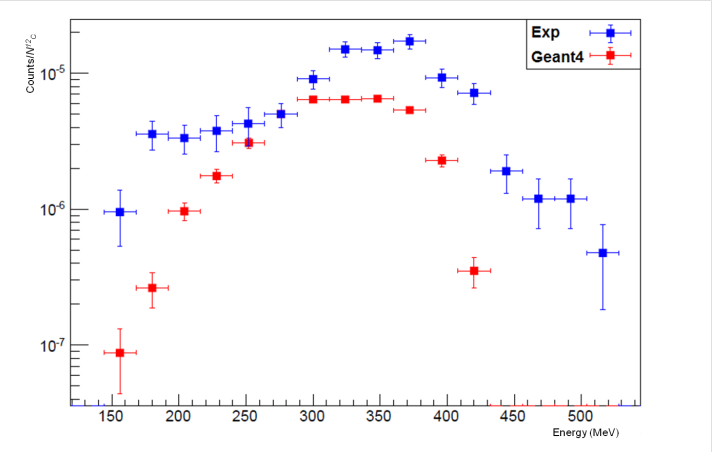

(a)

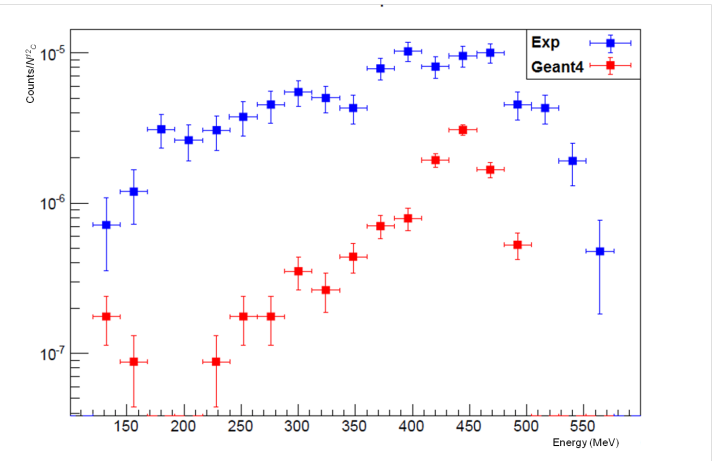

(b)

Figure 3.2.10: (a), (b): Data-Monte Carlo simulation comparisons for the ^{7}Be and ^{9}Be energy spectra associated to carbon fragmentation on the 5.81 mm thick lung-equivalent target (color online).

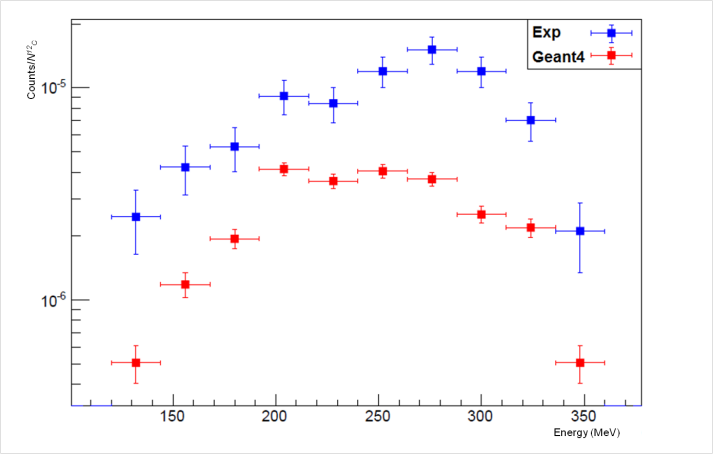

(a)

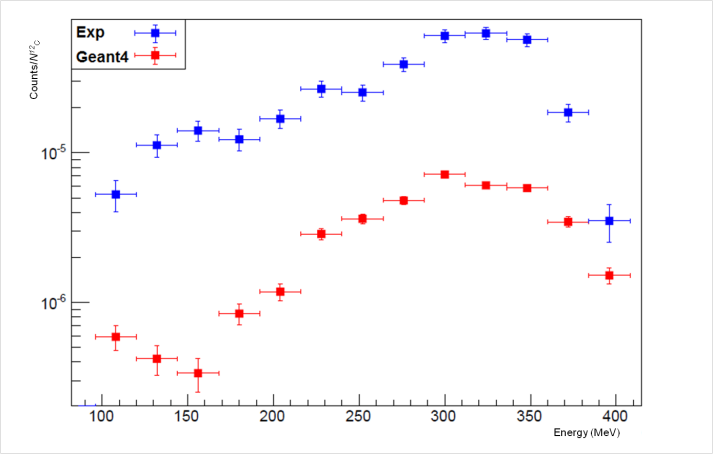

(b)

Figure 3.2.11: (a), (b): Data-Monte Carlo simulation comparisons for the ^{6}Li and ^{7}Li energy spectra associated to carbon fragmentation on the 10.3 mm thick lung-equivalent target (color online).

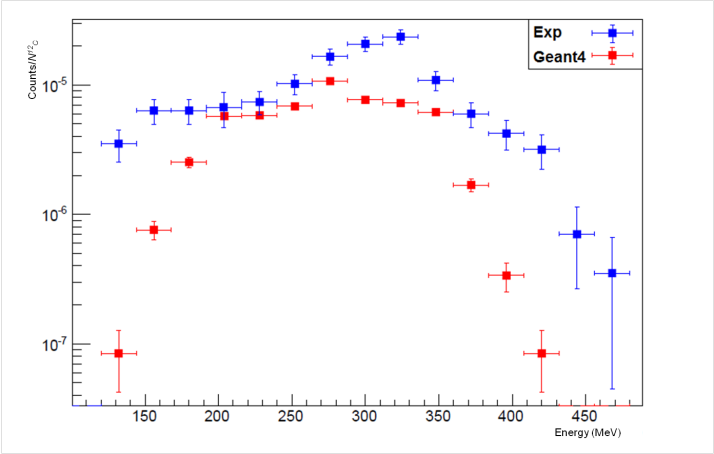

(a)

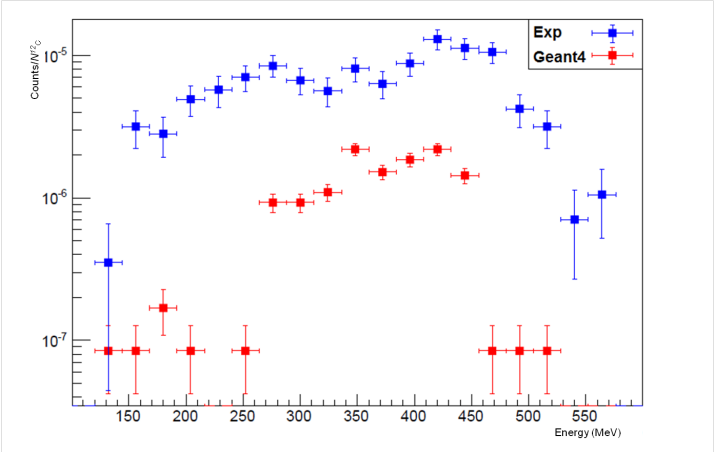

(b)

Figure 3.2.12: (a), (b): Data-Monte Carlo simulation comparisons for the ^{7}Be and ^{9}Be energy spectra associated to carbon fragmentation on the 10.3 mm thick lung-equivalent target (color online).

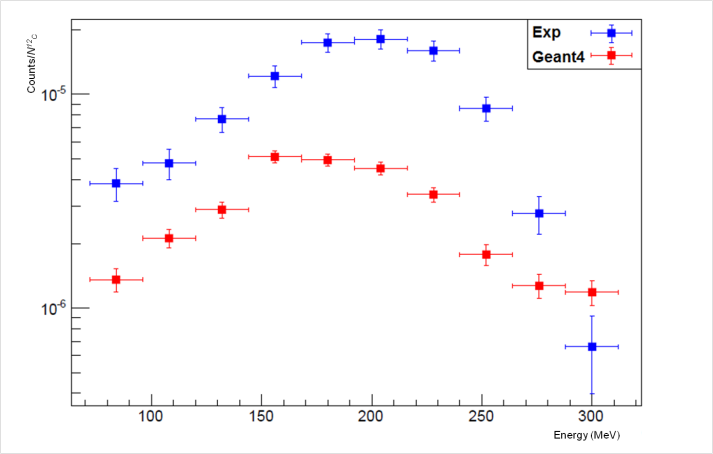

(a)

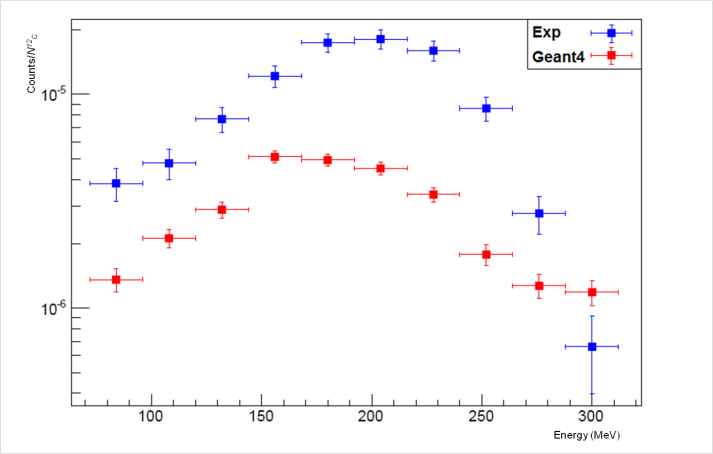

(b)

Figure 3.2.13: (a), (b): Data-Monte Carlo simulation comparisons for the ^{6}Li and ^{7}Li energy spectra associated to carbon fragmentation on the 20.6 mm thick lung-equivalent target (color online).

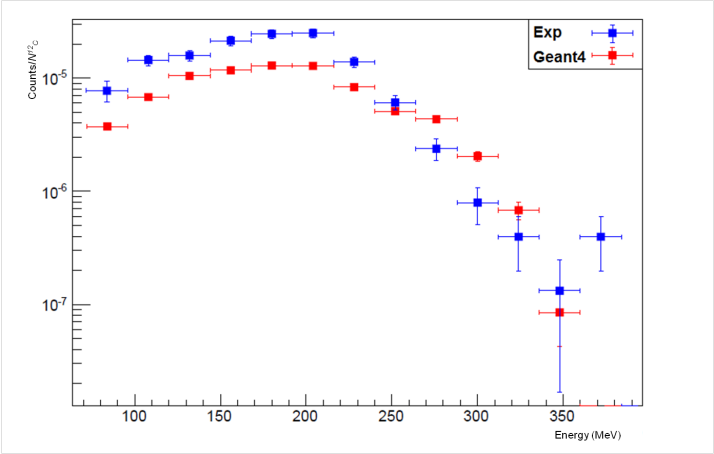

(a)

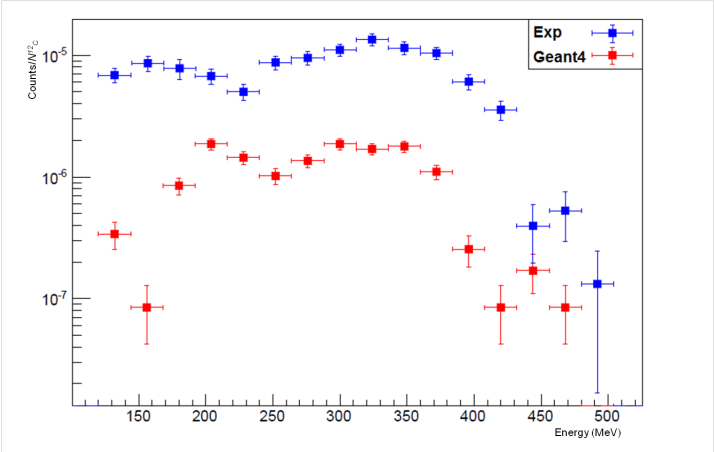

(b)

Figure 3.2.14: (a), (b): Data-Monte Carlo simulation comparisons for the ^{7}Be and ^{9}Be energy spectra associated to carbon fragmentation on the 20.6 mm thick lung-equivalent target (color online).

3.2.4 Fragments build-up curves

The build-up curves, i.e. the fragment yields as a function of the target thickness, shown in this section, were extracted by integrating the whole energy spectra for both experimental data and GEANT4 simulation.

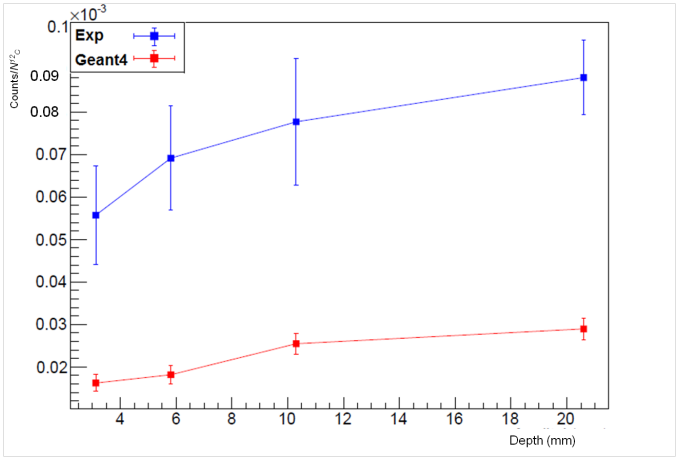

(a)

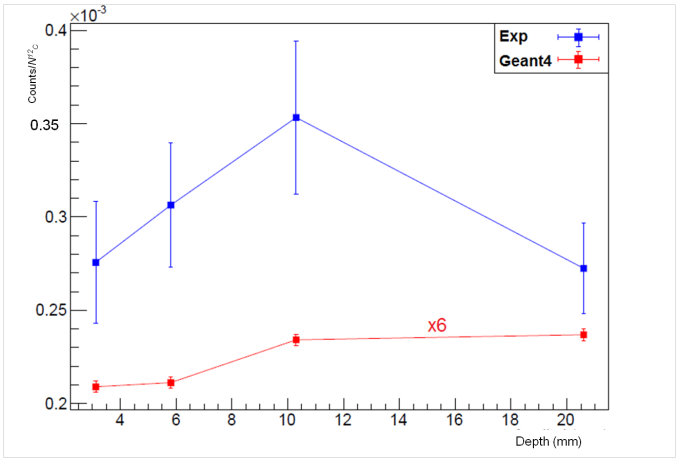

(b)

Figure 3.2.15: (a), (b): Data-Monte Carlo simulation comparisons for the ^{6}Li and ^{7}Li build-up curves associated to carbon fragmentation on different lung-equivalent target thicknesses. The ^{7}Li simulated yields are multiplied by a factor 6 (color online).

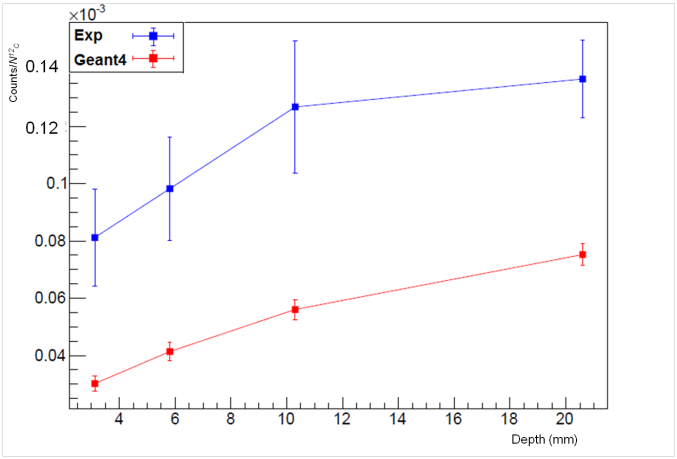

(a)

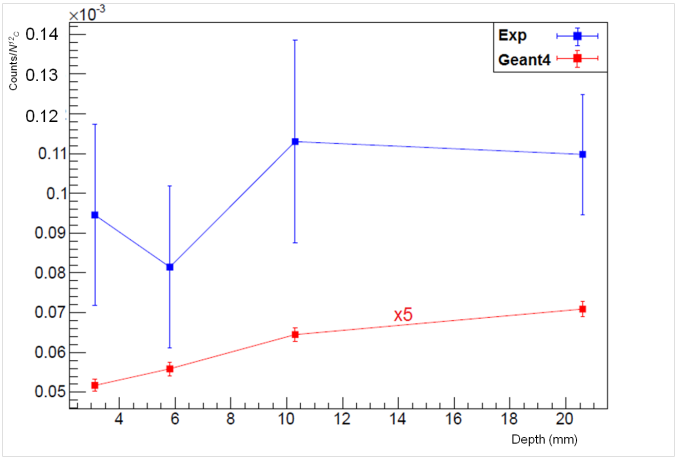

(b)

Figure 3.2.16: (a), (b): Data-Monte Carlo simulation comparisons for the ^{7}Be and ^{9}Be build-up curves associated to carbon fragmentation on different lung-equivalent target thicknesses. The ^{9}Be simulated yields are multiplied by a factor 5 (color online).

As can be seen from Figures 3.2.15 and 3.2.16, the amount of charged fragments detected increase accordingly with the target thickness, reaching a maximum value in correspondence to the carbon Bragg Peak, which equals about 29.2 mm for lung.

The GEANT4 BIC model seems reliable in reproducing the shape of the yields ditribution with respect to the target thickness but, as already seen by comparing the energy spectra, it strongly underestimates their absolute values. Indeed, the ^{7}Li and ^{9}Be simulated yields distributions have been multiplied by factors 6 and 5, respectively, in order to highlight their shapes.

The poor predictive ability of the GEANT4 BIC model indicates that further experimental measurements in different energy range and with different kinds of targets are mandatory. Indeed, other carbon fragmentation experiments on tissue-equivalent targets, as cortical bone and muscle, are foreseen. In order to evaluate also the lightest fragments production, i.e. the hydrogen and helium isotopes, a thicker silicon ΔE detector will be employed. Moreover, in order to extract the angular distributions, a device able to measure the produced fragments at different $\vartheta > 0°$ is also foreseen.

Chapter 4

Carbon fragmentation at relativistic energies

Inclusive double-differential cross-sections with respect to angle and energy are needed in the whole energy range of interest for cancer therapy, between 60 and 400 AMeV, for improving the three-dimensional transport of ^{12}C ions in matter.

Indeed, the chosen energy for the clinical beam implies a precise ions range in the tissue to be treated. Since the planned target volume can be up to about 30 cm deep inside the patient body, the needed carbons energy has to be, correspondingly, up to about 400 AMeV. This is the main reason for investigating carbon fragmentation, not only at intermediate energies, but also in the relativistic energy range, as it has been done at GSI laboratory by performing the ^{12}C + ^{12}C reaction at 400 AMeV on an 8 mm graphite target.

In this section, some preliminary data analysis results together with the comparison with those obtained by means of FLUKA Monte Carlo code are shown and discussed.

4.1 The global reconstruction algorithm

In order to fix the complete kinematics of the reaction, i.e. to determine the type and momentum of all the outgoing charged particles produced, a global reconstruction algorithm has been developed. While the particles charge has been directly measured via their energy loss in the ToF-Wall slats, their mass has been reconstructed via the measurement of their magnetic rigidity R, i.e. by exploiting the deflection of the ions trajectories inside the

ALADiN dipole magnet. This approach required the precise knowledge of the (non uniform) magnetic field inside and outside the magnet. Both the ALADiN geometry and the field map, consisting in a set of values (B_x, B_y, B_z) measured for various currents by the "Hall probes" in different points of the magnet, have been inherited from previous experiments already performed at GSI within the ALADiN collaboration [142].

Particularly, by means of the reconstruction algorithm, registered hits in the FIRST sub-detectors are combined to tracklets and later to global tracks for each event. Firstly, Interaction Region (IR) tracklets are obtained. Indeed, the four-planes Vertex Detector is used to reconstruct tracks of particles exiting the target.

The vertex tracking algorithm is based on a local approach. Starting from the last plane, a road is defined to find candidate cluster onto the next planes. At each step, the track parameters are re-computed thanks to a conventional χ^2-fit procedure. Together with the track information about the impact point of the primary ion on the target from the Beam Monitor, the vertex tracklets allow to reconstruct the interaction vertex in the target for fragmentation events. The recontructed interaction point can then serve as additional *hit*-point for subsequent track reconstruction.

The high spatial resolutions of the Vertex Detector and the Beam Monitor guaranteed an angular precision of the reconstructed tracklets of $\approx 0.06°$. IR tracklets with angles larger than 5° are extrapolated onto the KENTROS detector and matched to the hit KENTROS segments. The knowledge of the impact point on the KENTROS detector allows to perform signal attenuation and timing corrections for KENTROS hits before reconstructing the particle energy and its charge.

Forward-directed IR tracklets ($< 5°$) enter the ALADiN spectrometer and are subsequently detected by the ToF-Wall. The central part of the magnetic field of the ALADiN spectrometer resembles a Woods-Saxon potential of the form:

$$B\left(z\right) = \frac{B_0}{1 + exp\left(\frac{z-D}{a}\right)}, \tag{4.1.1}$$

where B_0 (≈ 0.8 Tesla) is the maximum magnetic field strength, D (≈ 70 cm) quantifies the length of the field and a (≈ 10 cm) quantifies the slope of the fall-off of the field, the so-called *surface thickness*, being $\vec{z}$ the incident beam direction. Taking into account the magnetic field shape, the relevant effect over the ion trajectories is a deflection in the horizontal ($\vec{x}$) direction, depending on the ion type and its energy.

A priori, particle properties as energy, charge and mass of the IR tracklets are not known and, as a consequence, the magnetic rigidity:

$$R = B\rho = \frac{p}{q} = \frac{mv}{q}, \tag{4.1.2}$$

needed for tracking in the magnetic field B of ALADiN is not at hand, with ρ being the trajectory curvature radius, p the particle momentum, q its charge and m its mass.

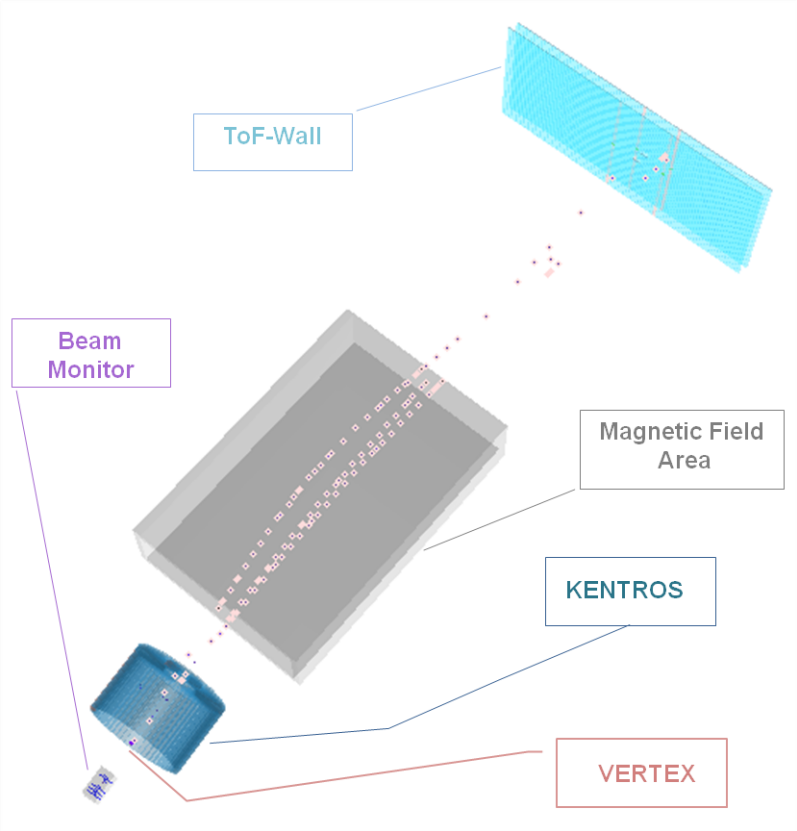

Figure 4.1.1: A 3-dimensional event display in the $(\vec{x}, \vec{z})$ bending plane associated to particles trajectories reconstructed by the global tracking algorithm.

For magnetic field tracking, the reconstruction code uses the measured magnetic field maps for different magnetic currents which are interpolated linearly in space and with the magnet current I, taking into account the

magnetic hysteresis. The strategy used for matching the IR tracklets to hits in the ToF-Wall and to obtain global tracks is outlined in the following.

For a given event, so-called *Global Track Candidates* (GTC) are established by combining all IR tracklets with all the hits in the ToF-Wall. This allows to associate a charge from the ToF-Wall to each GTC. An algorithm performs, then, iterative forward-tracking through the magnetic field which bends the particles in the horizontal plane for a given GTC. Indeed, starting from the positions and angles measured in the IR and with a *first-guess* value for the momentum, the measured coordinates are forward-tracked inside the ALADiN magnetic field. This task is performed by solving the equation of motion of a charge in a magnetic field, which is, as known, governed by the Lorentz equation:

$$\vec{F} = \frac{d\vec{p}}{dt} = \gamma m \frac{d\vec{v}}{dt}. \tag{4.1.3}$$

The procedure ends at the hit position on the ToF-Wall and, according to the difference between the measured value and the calculated one, the initial momentum is varied and the whole loop starts again until the calculated hit position agrees with the measured one. After convergence, a trajectory and momentum p for which the GTC impinges on the centre of the hit slat of the ToF-Wall is obtained. The vertical coordinate ($\vec{y}$) serves then to establish an objective function to rank the GTC and allows to select the best matching GTC as global tracks.

In Figure 4.1.1, a 3-dimesional event display of the reconstructed tracklets in shown.

The global track matching and reconstruction algorithm has been written in C++ and tested on several different Linux platforms. The low level software package has been developed for the raw data decoding, while the high level one has been established for performing a per event tracking by combining the information extracted from each sub-detector. The reconstruction output files are made as ROOT[1] ntples to be treated with opportunely written programs (*macros*) for extracting the searched cross-section distributions in angle and energy.

4.2 Mass distributions

Starting from the particles charge and time of flight given by the ToF-Wall and the reconstructed values for the rigidity and path length, the ve-

[1] http://root.cern.ch/drupal/content/about.

locity and the momentum vector have been calculated for each detected charged fragment. The knowledge of velocity and momentum allows then the calculation of the particle mass. As far as the fine-tuning of the global reconstruction code is ongoing, only very preliminary results will be shown.

As already mentioned, a maximum 10% relative error on the fragment mass is mandatory in order to have a clear separation of all the ions and isotopes under study. The requirement on the fragment mass separation directly translates into performance requirements (time and momentum resolution) for all the detectors that are used in the FIRST setup.

Particularly, being the mass of each fragment defined as:

$$m = Am_0\gamma = \frac{Am_0}{\sqrt{1-\beta^2}} \tag{4.2.1}$$

with m_0 being the proton rest mass energy (= 938.27 MeV), A the mass number and $\beta = v/c$, the mass measured in the spectrometer can be obtained by combining equations (4.1.2) and (4.2.1) as:

$$A = \frac{0.3RZ\sqrt{1-\beta^2}}{m_0\beta}, \tag{4.2.2}$$

where 0.3 is the conversion factor from Tm to GeV/c. As already seen, R is measured through the momentum-reconstruction procedure, the charge and the time of flight are both measured by the ToF-Wall and thus velocity is obtained after the pathlenght has been reconstructed by the global tracking algorithm.

In Figure 4.2.1 the preliminary mass spectra obtained for the different detected charged fragments are shown.

The relative error on A is hence related to the time and momentum resolutions by the relation:

$$\frac{(\Delta A)}{A} = \sqrt{\frac{(\Delta p)^2}{p^2} + \gamma^2\frac{(\Delta t)^2}{t^2}} \tag{4.2.3}$$

where $(\Delta p)^2/p^2 = (\Delta R)^2/R^2$ has been used. Single mass resolution for charges up to 6 is obtained, corresponding to a mass resolution $\Delta A/A$ of approximately 6% for $Z = 1$ fragments while it deteriorates for the $Z \geq 1$ ones. The dominant contribution to the uncertainty of the mass measurement is caused by the mass-dependent error of the time measurement which is amplified by the factor γ^2 ($\gamma^2 = 2.0$ for 400 AMeV). As the reconstruction code improving is in progress, better mass resolutions are foreseen.

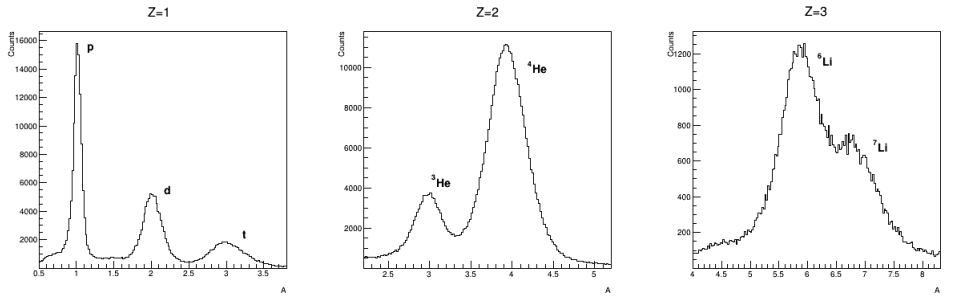

(a)

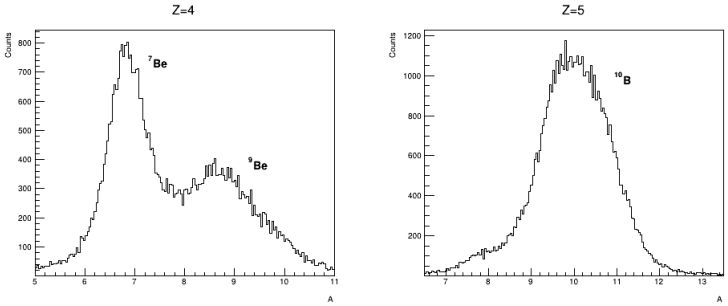

(b)

Figure 4.2.1: (a), (b): Reconstructed mass distributions of the detected carbons and fragments.

As one can clearly see from Figure 4.2.1, the hydrogen (p, d, t) and helium (^{3}He, ^{4}He) isotopes are fairly well resolved in the mass spectra, while for the lithium (^{6}Li, ^{7}Li), berillium (^{7}Be, ^{9}Be) and boron (^{10}B, ^{11}B) ones the resolution significantly worsens. Moreover, background events visible in Figure 4.2.1 are related to charges non correctly identified by the reconstruction algorithm. Nevertheless, an attempt to extract the first results from the data has been done trying to look at the cross-section angular and energy distributions presented in the next sections, in which background will be removed by means of a suitable correction factor.

4.3 Preliminary cross-section angular distributions

After performing Gaussian fits of the peaks, the mass spectra shown in Figure 4.2.1 have been integrated in order to extract the production yields

Y_i for each *ith* particle of charge Z and mass A. Then, the associated ^{12}C fragmentation cross-section has been obtained as follows:

$$\frac{d\sigma_i}{d\Omega} = \frac{Y_i}{N_{^{12}C} \cdot N_{t,S} \cdot 2\pi(cos\vartheta_2 - cos\vartheta_1) \cdot \epsilon_{rec} \cdot \epsilon_{id}}, \tag{4.3.1}$$

being $N_{^{12}C}$ the incident carbon ions measured by the Start Counter, $N_{t,S}$ the number of atoms per unit area of the ^{12}C target, $\Delta\Omega = 2\pi \cdot (cos\vartheta_2 - cos\vartheta_1)$ the solid angle covered by a circular crown of $\Delta\vartheta$ aperture, ϵ_{rec} and ϵ_{id} the reconstruction and the identification efficiencies of the tracking software, respectively.

Since a *minimum-bias*[2] trigger has been used, i.e. the trigger fires whenever the Start Counter gives a signal, both the dead time and the Start Counter efficiency are taken into account by normalizing with respect to the $N_{^{12}C}$ value.

For the $N_{t,S}$ calculation, both the ^{12}C target density ($\rho \approx 4.48$ g/cm^3) and thickness ($\delta x \approx 8.08$ mm) have been taken into account in the relation:

$$N_{t,S} = \frac{N_A \cdot \rho}{M} \cdot \delta x, \tag{4.3.2}$$

being N_A the Avogadro's number and M the carbon molecular weight. Concerning uncertainties estimate, 1% and 5% relative errors have been assumed for the $N_{t,S}$ and $\Delta\Omega$ estimates respectively, while the Poissonian error given by $\delta N_{^{12}C} = \sqrt{N_{^{12}C}}$ has been considered for the total incident carbon ions. Concerning δY_i, the standard deviation of the area of the Gaussian fit in the corresponding mass spectrum has been taken into account. As far as the systematic uncertainties on δY_i study is ongoing, only statistical errors have been considered.

Regarding the efficiencies estimation, both ϵ_{rec} and ϵ_{id} have been determined by comparing the information coming from the reconstruction algorithm applied to the data with those obtained by processing Monte Carlo events. Particularly, ϵ_{rec} is given by:

$$\epsilon_{rec} = \frac{N_{Glb}}{N_{Tot}}, \tag{4.3.3}$$

being N_{Glb} the number of reconstructed global tracks of the data sample and N_{Tot} the total number of reconstructed tracks of a Monte Carlo sample, obtained by selecting positive charged particles which originate from

[2] *Minimum-bias* refers to events collected with (ideally) totally inclusive trigger as, in principle, contains all types of interactions proportionally to their natural production rate.

the target, traverse the Vertex Detector and produce a hit in the ToF-Wall. The particles are simulated and tracked for a fixed Z, thus avoiding reconstrunction possible failure related to *full* fragmentation events processing. The ϵ_{rec} values have been determined depending on the charge of the particle and for well defined energy and angle intervals.

The ϵ_{rec} value does not include the charge identification efficiency, separately estimated by counting how many reconstructed charges have been wrongly identified. This is a more complex correction obtained by building the matrix with the number of reconstructed charges as row elements and with the number of simulated charges (*true charges*) as column ones. After normalizing each entry by the sum of the column elements, i.e. by the total number of true reconstructed charges, and after inverting the obtained matrix, the charge identification correction ϵ_{id} for each Z has been obtained and applied to the data.

In Figures 4.3.1 and 4.3.2, the preliminary $Z = 1$ and $Z > 1$ experimental cross-section distributions with respect to the emission angle ϑ_{lab} are shown.

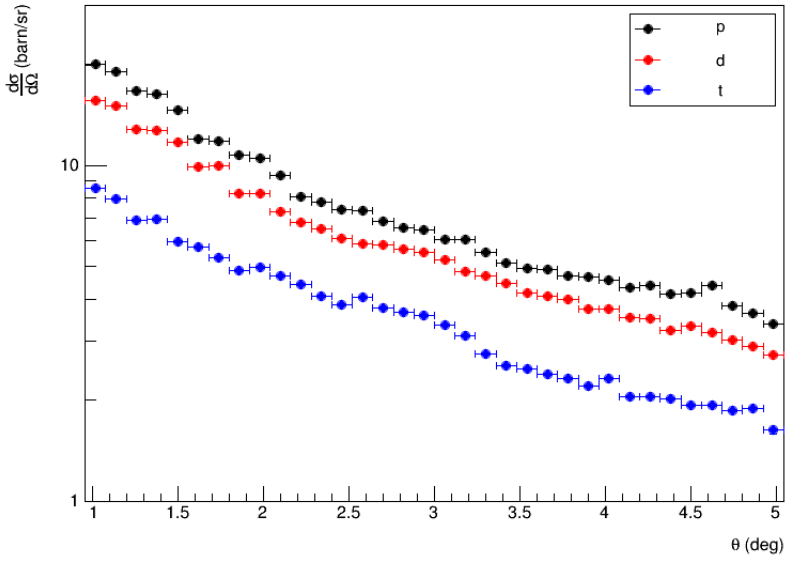

Figure 4.3.1: Experimental cross-section angular distributions for protons, deuterons and tritons.

In order to better disentangling the produced fragments from the elastic ^{12}C ions, the selected events are only those for which more than one track with a common vertex have been reconstructed.

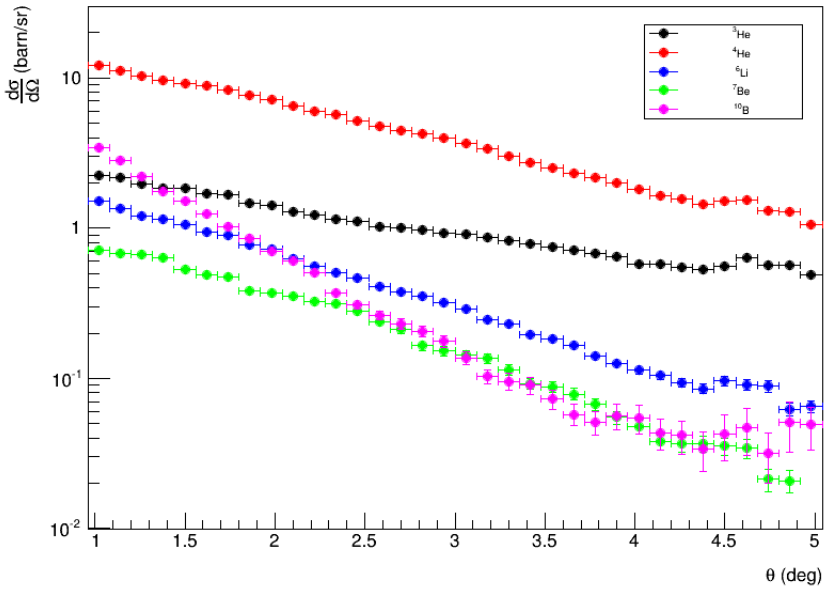

Figure 4.3.2: Experimental cross-section angular distribution for ^{3}He, ^{4}He, ^{6}Li, ^{7}Be and ^{10}B.

Nevertheless, the data corresponding to emission angles $\vartheta_{lab} \leq 1°$ are not shown as the reconstruction code, even if applying the ϵ_{id} correction, still misidentifies the detected particles. Indeed, approaching to $\vartheta_{lab} \approx 0°$, the fragmentation events are overwhelmed by the carbon beam, so that an improved charge identification efficiency at very small deflection angles would be necessary.

The general trend of the cross-section angular distributions already discussed for the intermediate energy results is confirmed also for the relativistic energy domain. Indeed, the probability to detect fragments fall exponentially with increasing angle, except for the lighter ones, i.e. hydrogen and helium isotopes, which are spread out over the investigated angular range.

These results confirm that the lightest fragments ($Z = 1$ and 2) mainly contribute to the scatter of the dose far from the original beam direction

due to their large angular deflection while the heavier ones, being emitted at small angles, will essentially contribute to the dose deposition in and close the target volume.

4.4 Preliminary double-differential cross sections

In order to obtain the double-differential cross-section, the energy distributions have been determined at each point of the previous angular distributions. As far as both the reconstruction and identification efficiencies evaluation with respect to kinetic energy is in progress, these factors have not been taken into account.

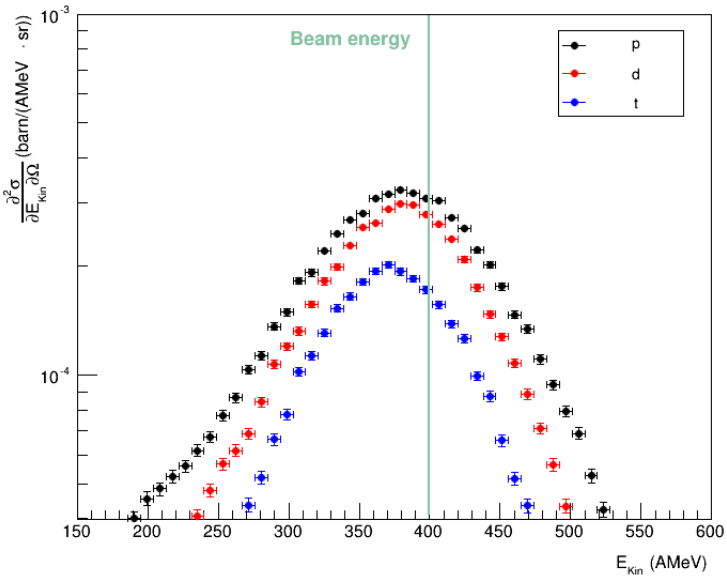

Figure 4.4.1: Experimental double-differential cross-section energy distributions for protons, deuterons and tritons.

Starting from the reconstructed momentum p and mass m, the kinetic energy E_{Kin} of each detected fragment has been computed via the relativistic relation:

$$E_{Kin} = E_{Tot} - mc^2, \tag{4.4.1}$$

being the total energy E_{Tot} of a relativistic particle given by:

$$E_{Tot} = \sqrt{p^2c^2 + m^2c^4}. \tag{4.4.2}$$

Since the natural units system has been used, i.e. $\hbar = c = 1$ has been assumed, equation (4.4.1) becomes:

$$E_{Kin} = \sqrt{p^2 + m^2} - m. \tag{4.4.3}$$

Thus, the $\partial^2\sigma/\partial E_{Kin}\partial\Omega$ have been extracted by dividing equation (4.3.1) for the energy bin width, as shown in Figures 4.4.1 and 4.4.2 for $Z = 1$ (protons, deuterons and tritons) and $Z > 1$ (^{3}He, ^{4}He, ^{6}Li, ^{7}Be and ^{10}B) particles, respectively.

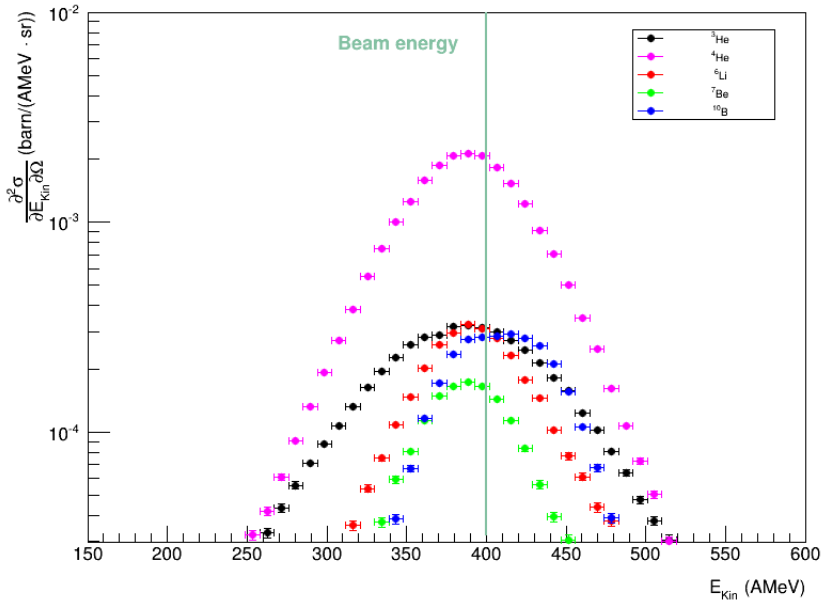

Figure 4.4.2: Experimental double differential cross-section energy distributions for ^{3}He, ^{4}He, ^{6}Li, ^{7}Be and ^{10}B.

As can be seen, the distributions are dominated by a Gaussian peak centered close to the beam energy per nucleon (400 AMeV), whose width and amplitude decrease with increasing the mass of the fragments. These

observations confirm that most of the detected particles are coming from the projectile fragmentation [143].

However, fragments with more energy per nucleon than the primary particle are observed. Bertini et al. [144] explained this as an interaction between nucleons where the Fermi momentum is transferred from target or projectile nucleons to the fragment. Sometimes the momentum is parallel resulting in high energy fragments.

4.5 The Monte Carlo simulation

As already mentioned, the experimental results will contribute directly to constrain the nuclear reaction models used in the FLUKA Monte Carlo code. In the following, an overview of the simulation approach is shown and some remark on the interaction models used by the code are pointed out.

The simulation of the FIRST experiment not only supported design and optimization of the experimental setup, but also provided training data for the reconstruction software development, since it can supply the simulated detector response data of a full event. Furthermore, it facilitates the evaluation of acceptances, reconstruction efficiencies and other systematics. By means of the multi-purpose FLUKA Monte Carlo code, the simulation of the particle transport and interactions has been performed. In addition to an accurate description of electromagnetic processes, FLUKA was shown to provide a modelling of nuclear interactions which is judged to be satisfactory in the energy range of FIRST [67] [69].

The implementation of the simulation can be divided into several subsectors:

- description of experimental set up configuration (beam phase space, geometry and materials, parameters describing detector properties and magnetic field),
- particle transport and retrieval (scoring) of basic physical quantities of the tracks (i.e., primary particles and created secondary particles which are propagated through the detector geometry) and hits (i.e., energy depositions of tracks in sensitive detector elements),
- modelling of the subdetector responses and digitization,
- storing of simulated track, hit and detector signal data for further processing and analysis.

The experimental setup has been implemented including all detectors and the ALADiN spectrometer. The geometry and all the materials of the detectors have been modelled with a considerable detail, i.e. including the wires of the BM, vacuum windows, the air and gas mixtures crossed in the setup, to reliably evaluate the out-of-target fragmentation in all the materials crossed by the carbon projectiles and the produced fragments.

More complex signal dependencies, such as detection efficiencies and resolutions, are determined from measurements and parametrized for the simulation. This guaranteed a reduced computative effort and decreased the overall complexity of the simulation, while preserving its predictive power at a reasonable level. The resulting analog quantities are digitized and cast into a format as needed to be processed by the data reconstruction software.

Concerning the interaction models for electromagnetic and nuclear processes relevant for the transport of both primary and secondary particles, the recommended configuration for hadrontherapy ('HADROTHErapy') has been chosen. This option uses delta-ray production and transport cuts of 100 keV. Neutrons are tracked down to thermal energies. Electromagnetic physics are described within the EMF (ElectroMagnetic Fluka) package which accounts for energy loss, straggling and multiple Coulomb scattering of charged particles. However, no EM particle tracks were scored and no delta-rays were produced (high cut values) in order to save computation time.

For ion projectile energies from 5 AGeV down to 100 AMeV, the relativistic quantum molecular dynamics (rQMD) model [145] is employed as the hadronic event generator. For lower energies, a model based on the Boltzmann master equation (BME) theory [146] is used to describe hadronic interactions.

Total nuclear reaction cross-sections are calculated based on an empirically modified version of the Tripathi parametrization for nucleus-nucleus interactions [145] [147]. De-excitation of the excited fragments was processed with the FLUKA evaporation/fission/fragmentation module. Hadron-nucleus interactions were described by the PEANUT (PreEquilibrium Approach to NUclear Thermalization) model [59] which includes an intra-nuclear cascade stage followed by a pre-equilibrium stage, and then equilibrium particle emission. Simulations were done with the FLUKA version 2008.3.

Particularly, the rQMD nucleus-nucleus model [148] used by FLUKA in the energy range of interest for the present work, is an extension of the non-relativistic quantum molecular dynamics approach successfully used to study heavy ion collisions at low and medium beam energies E_{Kin} = 50 -

2000 AMeV [131]. Indeed it explicitly follows the trajectories of all hadrons (including the produced particles), thus providing the full information about the dynamical evolution of the N particle phase space distribution. Like the non-relativistic QMD, rQMD combines the classical propagation of the hadrons (molecular dynamics) with quantum effects as stochastic scattering, particle decay and Pauli blocking in the collisions. Furthermore, the rQMD approach treats both the explicit Lorentz invariance and the additional inelastic reaction channels.

A more detailed description of the models used by the FLUKA code is given in Appendix B (4.9).

4.6 Cross sections comparisons between data and FLUKA MC code

In order to make a first guess on the predictive ability of the simulation to reproduce the measured cross sections, the preliminary results presented in the previous sections have been compared with those obtained by using the FLUKA code.

In Figures 4.6.1 - 4.6.8 the experimental and simulated cross-section distributions with respect to ϑ_{lab} angle for protons, deuterons, tritons, ^{3}He, ^{4}He, ^{6}Li, ^{7}Be and ^{10}B are shown, respectively. Since the fine tuning of the reconstruction software is in progress and, as a consequence, efficiencies are still roughly estimated and systematic errors are not yet taken into account, it is possible to make only some considerations on the general agreement between experimental and simulated cross-sections.

Concerning the angular distributions comparisons, the FLUKA code seems to overestimate the cross-sections, especially for $Z > 1$, in the whole ϑ_{lab} range.

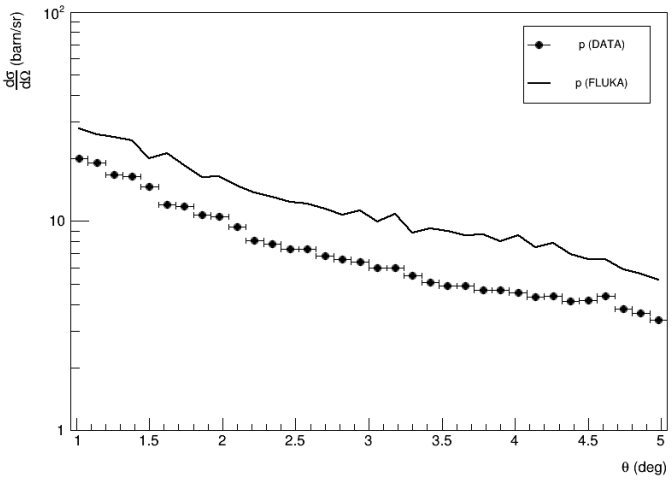

Figure 4.6.1: Comparison between experimental and simulated cross-section angular distributions for protons.

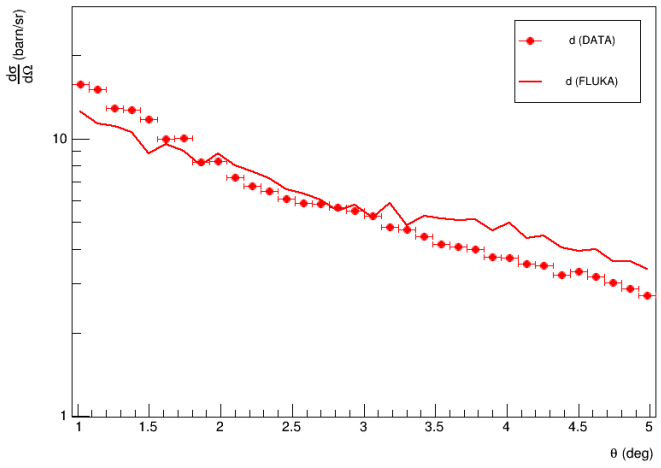

Figure 4.6.2: Comparison between experimental and simulated cross-section angular distributions for deuterons.

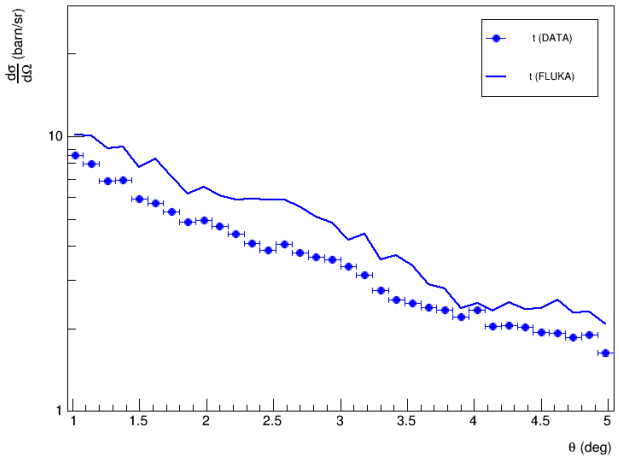

Figure 4.6.3: Comparison between experimental and simulated cross-section angular distributions for tritons.

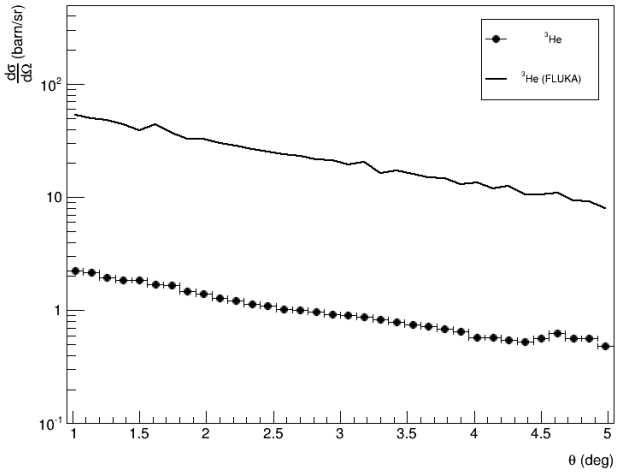

Figure 4.6.4: Comparison between experimental and simulated cross-section angular distributions for ^{3}He.

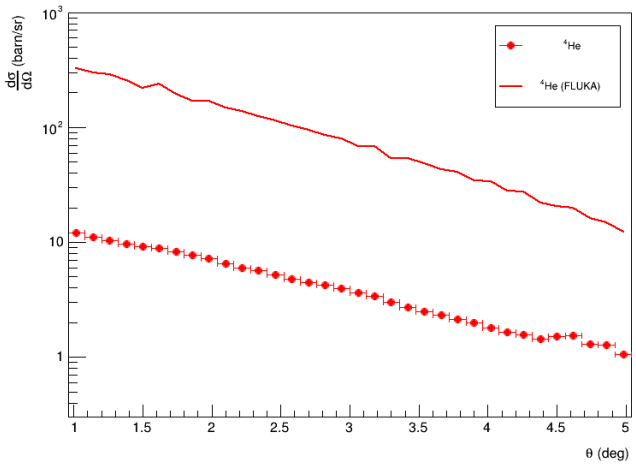

Figure 4.6.5: Comparison between experimental and simulated cross-section angular distributions for ^{4}He.

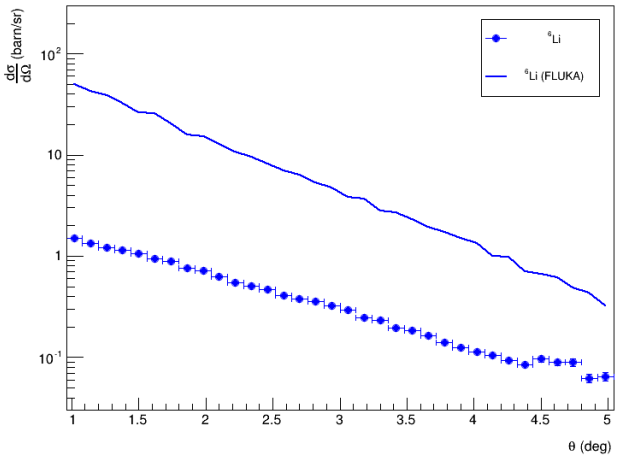

Figure 4.6.6: Comparison between experimental and simulated cross-section angular distributions for ^{6}Li.

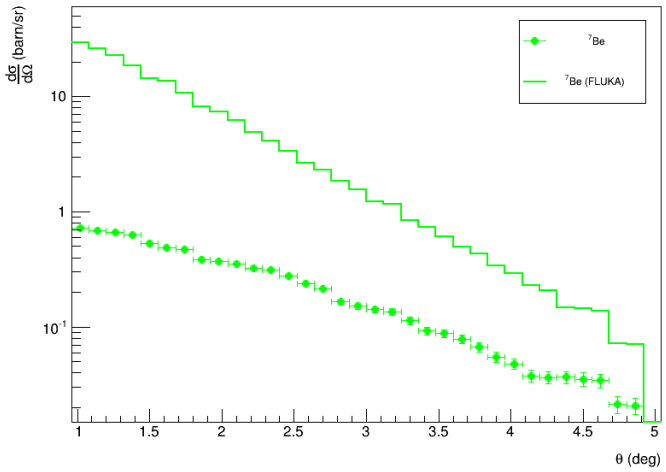

Figure 4.6.7: Comparison between experimental and simulated cross-section angular distributions for ^{7}Be.

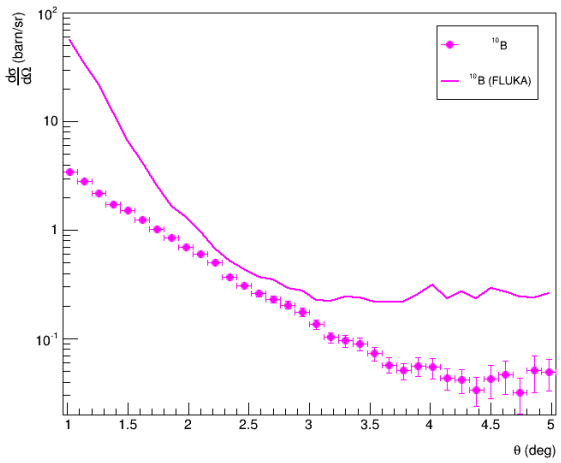

Figure 4.6.8: Comparison between experimental and simulated cross-section angular distributions for ^{10}B.

Particularly, the simulated protons, deuterons and tritons production cross-sections are only slightly greater than the experimental ones, while the exponential fall-off of the distributions is fairly well reproduced. Concerning heavier fragments, the higher slope of the simulated distribution with respect to the measured one seems to be a common feature, but it becomes more evident for increasing the mass of the fragment. The worst case is represented by ^{10}B comparison, for which the simulation predict a more focused distribution with respect to data and shows an exponential fall-off less steep than the experimental one, becoming almost constant for $\vartheta > 3°$. This can be a problematic aspect which one has to take carefully into account since boron, being the heaviest fragment, would produce a biological damage very similar to that of carbon but even outside the tumor region. As a consequence, the FLUKA predictions must be improved in order to better control the angular spreading.

In Figures from 4.6.9 to 4.6.16, the experimental and simulated double-differential cross-section distributions with respect to kinetic energy are shown. As already mentioned in section 4.4, the evaluation of the reconstruction and identification efficiencies for selected energy intervals is in progress, therefore the presented energy distributions for both data and Monte Carlo code have been determined without taking into account of these correction factors.

By observing the comparison between simulated and measured energy distributions, it can be seen that the simulation reproduce quite well the shape of fragments distribution, with the exception of protons for which the simulation foresees a low energy tail not present in the data. For heavier fragments the simulation predicts a Gaussian peak shifted towards lower energy than experimental data, which are centered closer to the beam energy per nucleon and with a narrower energy spread. Discrepancies between the results extracted from data and FLUKA code increase with increasing the mass of the fragments.

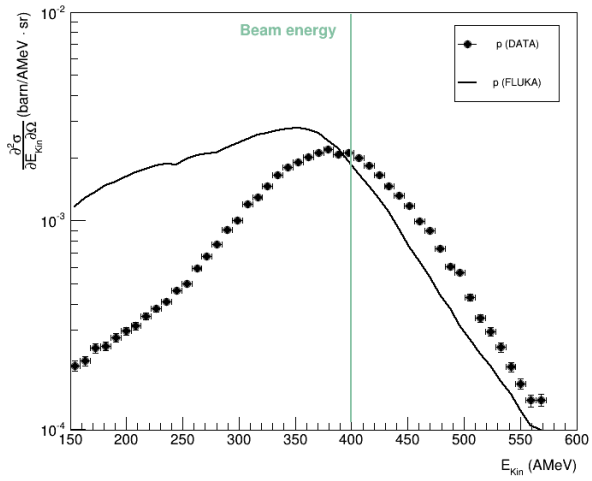

Figure 4.6.9: Comparison between experimental and simulated double-differential cross-sections for protons.

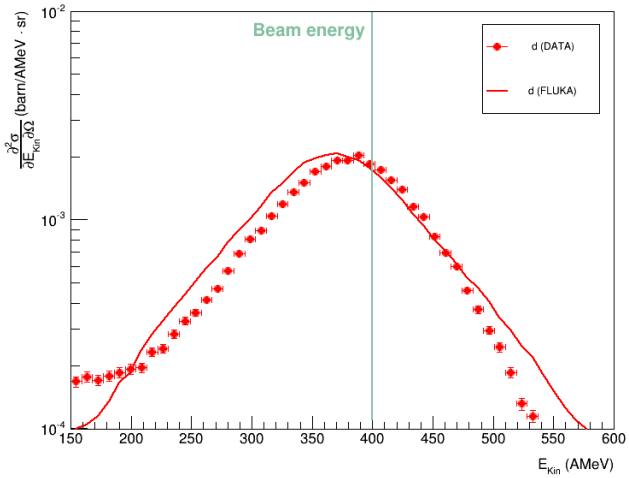

Figure 4.6.10: Comparison between experimental and simulated double-differential cross-sections for deuterons.

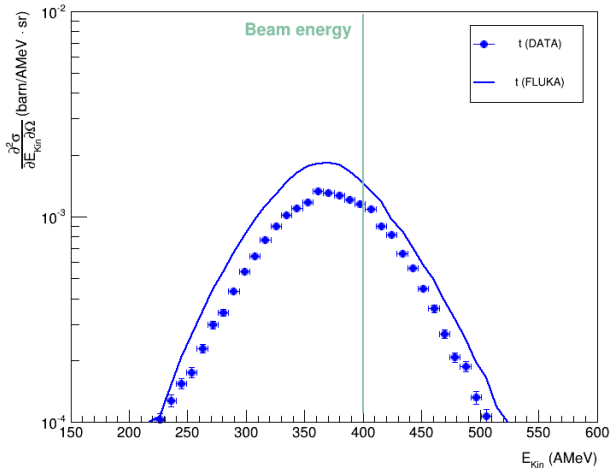

Figure 4.6.11: Comparison between experimental and simulated double-differential cross-sections for tritons.

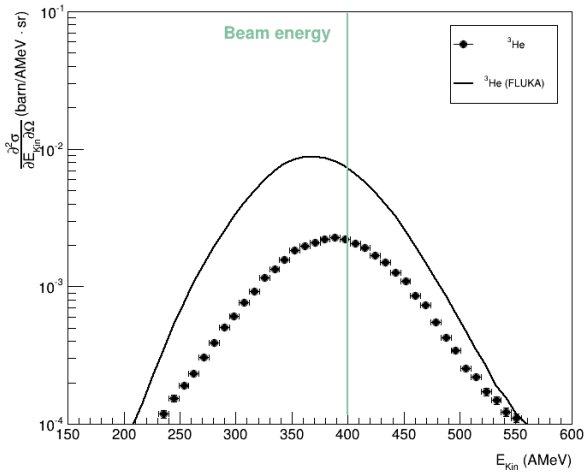

Figure 4.6.12: Comparison between experimental and simulated double-differential cross-sections for ^{3}He.

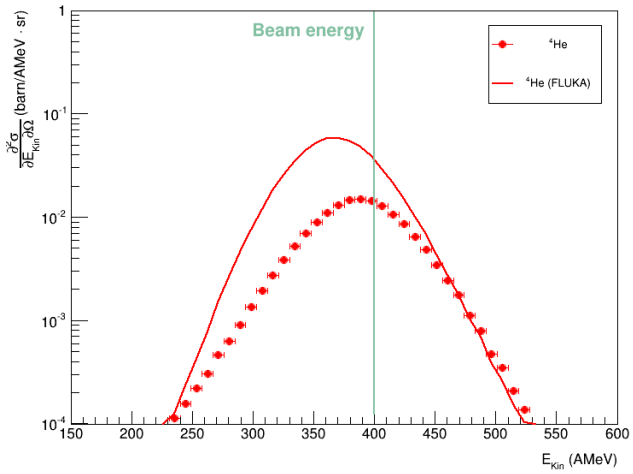

Figure 4.6.13: Comparison between experimental and simulated double-differential cross-sections for ^{4}He.

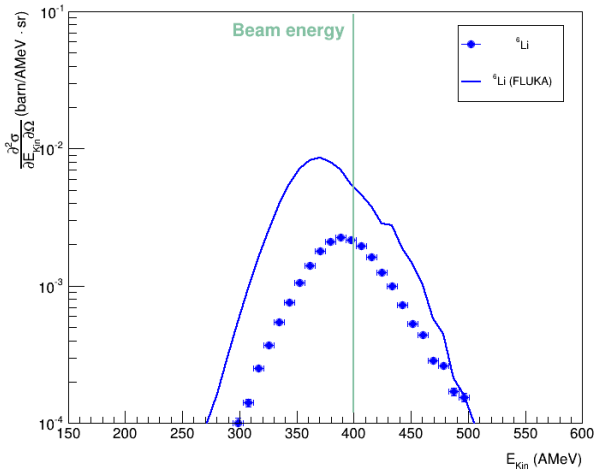

Figure 4.6.14: Comparison between experimental and simulated double-differential cross-sections for ^{6}Li.

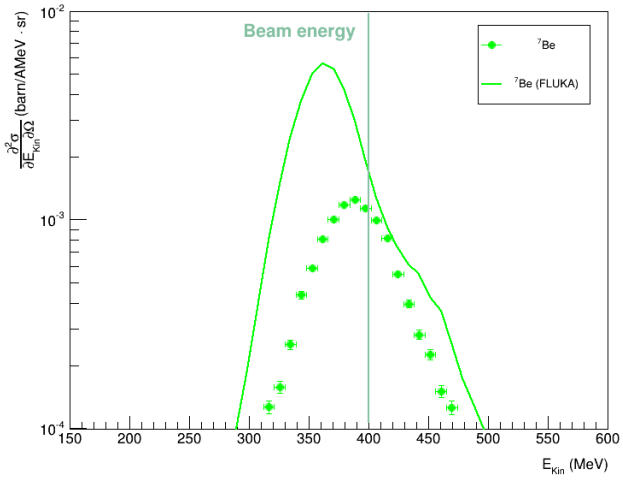

Figure 4.6.15: Comparison between experimental and simulated double-differential cross-sections for ^{7}Be.

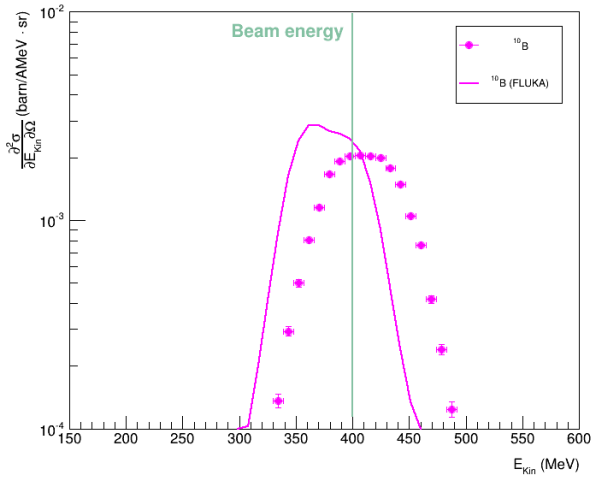

Figure 4.6.16: Comparison between experimental and simulated double-differential cross-sections for ^{10}B.

The general trend of the comparisons between data and FLUKA code seem to indicate that the nuclear reaction models implemented in the simulation, mainly referring to the rQMD model performances, are not reliable in reproducing the angular cross-section distributions, since the discrepancies between data and Monte Carlo can be up to about one order of magnitude, and even more in some cases, and the prediction ability of the models worsens for heavier fragments.

This is also probably related with the wrong assignment of the correct charge to the reconstructed global track which still affects the tracking software. Indeed it misidentifies with a higher probability the more focused fragments which tend to move on trajectories frequently mixed up with those of carbon ions. Moreover, the identification efficiency of the reconstruction algorithm worsens also for those particle tracks having a high deflection angle with respect to the ALADiN magnet optical axis. Travelling along a peripheral region inside the magnet, where the magnetic field is not accurately known, these particles are strongly affected by high order aberrations which prevent from the correct estimation of the p/q value.

Finally, it has to be noticed that the rQMD model benchmarking with respect to experimental fragmentation cross sections is very limited in the literature [67], with the exception of neutron production and fragments integral cross-section values [149]. As being a first attempt to validate the model versus experimental fragmentation data, taking into account the ongoing optimization work on the reconstruction software, the obtained preliminary results seem to be a good starting point.

Conclusions and outlook

One of the main motivations for the use of carbon ions beams in cancer therapy is their increased biological effectiveness in the tumor volume together with the lower radiation damage induced in the surrounding healthy tissue. On the other hand, the main drawback in carbon therapy is related to nuclear reactions which may cause a significant modification of the radiation field inside the patient. Particularly, fragmentation reactions occur along the beam penetration path in tissue leading to the attenuation of the primary ions flux, and to the build-up of secondary lower-charge fragments, which give rise to the characteristic dose tail behind the Bragg peak.

As it is known, the biological effect of accelerated ions interacting with the tissues depend on their energy and atomic number, therefore the produced fragments have a different biological effect than the primary ions. As a consequence the alterations induced in beam quality have to be considered in the treatment planning systems (TPSs) based on carbon beams.

Monte Carlo simulations represent one of the most effective tools for accurate calculations of dose deposition, being able to achieve a more realistic description of the physical processes with respect to analytical codes, taking into account the effects due to the primary particles as well as to the secondary ones produced along the path in the matter.

In order to obtain reliable results, the physical models implemented in the Monte Carlo codes have to be validated versus experimental data. In particular, the accuracy of nucleus-nucleus interaction models is crucial in carbon ion therapy, in order to have a reliable prediction of the produced nuclear fragments. It has to be stressed that the double-differential cross sections measurements already performed in order to benchmark the reaction models are still insufficient. Therefore, the main goal of the present work was to extend the experimental carbon fragmentation cross-sections database by performing three different experiments at both intermediate and relativistic energies. The data have been also used to test the performances of two

different Monte Carlo codes, GEANT4 and FLUKA. Consequently, the results shown in this work represent a contribution to improve the carbon ions TPSs performances.

The first experiment was performed with a carbon beam at 62 AMeV impiging on a thin carbon target and the measured cross sections were used to validate two GEANT4 nuclear reaction models: the Binary Light Ion Cascade (BIC) and the Quantum Molecular Dynamics (QMD). The results showed that the QMD model approximates the low-energy region of the double-differential cross sections better than the BIC one. The latter, on the other hand, gives better results with respect to the QMD in reproducing the fragmentation peak, i.e. the largest contribution to the double-differential cross sections. As a consequence, the integrated double-differential cross sections as a function of the angle, i.e. the angular distributions, are better approximated by the BIC model than the QMD one. Even though the comparison between the measured cross sections and the GEANT4 predictions shows promising results, the prediction capability of both models needs to be improved at intermediate energies.

A second experiment at 62 AMeV was performed in order to measure the fragment yields in a condition closer to that of a real treatment, i.e. by using thick tissue-equivalent (lung) targets. Since fragments are produced by projectiles at different energies in the thick targets, it is difficult to constraint the nuclear reaction models by a direct comparison between the results of these models and the presented experimental results. This is especially true if different models are necessary for different energy ranges. Nevertheless, the GEANT4 BIC model seems to reproduce fairly well the shape of the normalized yields distributions with respect to the energy and the penetration depth, but it underestimates sistematically their values. These results clearly indicates that the simulation predictive ability has to be improved in this energy range.

As far as the incident carbon ions energy for hadrontherapy applications ranges from about 30 to 400 AMeV, the third experiment was performed in order to cover the lack of information in the relativistic energy domain. Even if the data analysis is still in progress, preliminary results concerning both cross-section angular and energy distributions are presented. Moreover, by observing the comparison between data and the results coming from the FLUKA Monte carlo code, large discrepancies are evident, thus confirming the usefulness of the performed experimental measurements.

It has also to be noted that the presented preliminary results refers to the small angles analysis, i.e. for $\vartheta < 5°$, while the large angle data analysis

is still in progress. When the results of the two angular regions will be combined, the carbon fragmentation cross-sections with respect to energy and angle will be accurately known in a wide angular range for the first time.

Furthermore, when the data on carbon fragmentation will be adequate to ensure the proper simulation codes performances, the future goal is to measure with great accuracy the fragmentation of different projectile-target combinations, which seem potentially useful for medical applications. In particular, possible future measurements regard the He and Li fragmentation cross-sections in order to explore other possibilities besides the use of carbon ions.

Appendix A
GEANT4 ion interaction models for hadrontherapy applications

As far as the measured fragmentation cross-sections discussed in the present work have been used to test the performances of the nuclear reaction models implemented in the GEANT4 Monte Carlo code, in this section an overview of the code and the chosen models is given.

GEANT4 is an object-oriented toolkit to simulate the passage of particles through matter. Firstly developed for the high energy physics domain, nowadays it is used in several fields which involve also low energy range applications as medical physics, since it provides interaction models for electromagnetic and nuclear processes connected with the transport of therapeutic ion beams. Indeed, GEANT4 simulations of diagnostic devices or radiotherapy techniques have been worldwide carried out in recent years by several research groups involved in medical applications.

GEANT4 was designed and developed by an international collaboration, formed by individuals from a number of cooperating institutes and it builds on the accumulated experience of many contributors to the field of Monte Carlo simulation of physics detectors and physical processes. In this context, the medical physics research group at LNS-INFN in Catania, has taken part to the development of the toolkit, enjoying the collaboration and giving some contributions, as those concerning the low energy electromagnetic and hadronic models validation [150].

As far as a particle in flight is subjected to many competing processes and different models are available in the code for describing the same process, a criterion of choice has to be followed by the user, according to his require-

ments and physical constraints. The large number of available interaction models can be divided into three classes: the *data driven models* largely based on evaluated or measured data, the *parametrised models* predominantly based on parameterisations and extrapolations of experimental data under some theoretical assumptions, and models which are mainly *theory-based*, which includes a set of different theoretical approaches to describe hadronic interactions, depending on the addressed energy range and computing performance needs. Anyway, models belonging to different classes can be combined in order to achieve the required level of accuracy for the specific simulation purposes.

In order to simulate carbon ion beams inelastic interactions with matter at intermediate energies and study how the primary particle fragmentation can influence the radiation field, the more suitable nucleus-nucleus models implemented in GEANT4 are represented by the `G4BinaryLightIonReaction` and the `G4QMDReaction`.

4.7 The Binary Light Ion Reaction model

The `G4BinaryLightIonReaction` model is an improved version of the *Binary Cascade* model (applicable only to pions, protons and neutrons). It is an intranuclear cascade model used to simulate the inelastic scattering of light ion nuclei and it is applicable for projectile energy ranging from about 80 AMeV to 10 AGeV.

In simulating light ion reactions, the initial state of the cascade is prepared in the form of two nuclei. The lighter of the collision partners is selected to be the projectile. The scattering is modelled by propagating the nucleons of the ion as free particles through the nucleus [151]. In the model, primary nucleons are propagated within 3-dimensional detailed model of the nucleus where suffer binary scatterings with individual nucleons of the nucleus; secondary particles eventually produced in the interaction are propagated and can, in turn, re-scatter with nucleons, creating the cascade.

The nucleus is modelled by explicitly positioning nucleons in space, and assigning momenta to these nucleons. This is done in a way consistent with the nuclear density distributions, Pauli's exclusion principle and the total nuclear mass. Free hadron-hadron elastic and reaction cross-section are used to define collision locations within the nuclear frame. Where available, experimental cross-sections are used directly or as a basis for parameterizations used in the model. The propagation of particles in the nuclear field is done by

numerically solving the equations of motion, using time-independent fields derived from optical potentials. The cascade begins with a projectile and the nuclear description, and it stops when the average energy of all participants within the nuclear boundaries are below a given threshold. The remaining pre-fragment will be treated by pre-equilibrium decay and de-excitation models.

The initial condition of the transport algorithm is a 3-dimensional model of a nucleus and the primary particle type and energy. As regards the first one, a 3-dimensional model of the nucleus is constructed from A nucleons and Z protons with coordinates $\boldsymbol{r}_i$ and momenta $\boldsymbol{p}_i$, with i = 1, 2,..., A. Radial positions r_i are selected randomly in the nucleus rest frame according to the nuclear density $\rho(r_i)$. For nuclei with $A > 16$ a Woods-Saxon form of the nuclear density is used [152]:

$$\rho\left(r_i\right) = \frac{\rho_0}{1 + exp\left[\left(r_i - R\right)/a\right]}, \tag{4.7.1}$$

where ρ_0 is approximated as:

$$\rho_0 = \frac{3}{4\pi R^3}\left(1 + \frac{a^2\pi^2}{R^2}\right)^{-1}, \tag{4.7.2}$$

with a = 0.545 fm, $R = r_0 A^{1/3}$ fm and the correction r_0 = 1.16(1 - $1.16\mathrm{A}^{-2/3}$) fm.

For light nuclei the harmonic-oscillator shell model is used for the nuclear density [153]:

$$\rho\left(r_i\right) = \left(\pi R^2\right)^{-3/2} exp\left(-r_i^2/R^2\right), \tag{4.7.3}$$

where $R^2 = (2/3)<r^2> = 0.8133 \cdot A^{2/3}$ fm^2. To take into account the repulsive core of the nucleon-nucleon potential it is assumed inter-nucleon distance of 0.8 fm. The nucleus is assumed to be spherical and isotropic, i.e. each nucleon is placed using a random direction and the previously determined position r_i.

The momenta p_i of the nucleons are chosen randomly between 0 and the Fermi momentum ${p_F}^{max}(r_i)$. The Fermi momentum, in the local Thomas-Fermi approximation as a function of the nuclear density ρ is:

$$p_F^{max}\left(r\right) = \hbar c\left(3\pi^2\rho\left(r\right)\right)^{1/3}. \tag{4.7.4}$$

The total vector sum of the nucleon momenta has to be zero, i.e. the nucleus must be constructed at rest.

The effect of collective nuclear interaction upon participants is approximated by a time-invariant scalar optical potential, based on the properties of target nucleus. For protons and neutrons the potential used is determined by the local Fermi momentum $p_F(r)$ as:

$$V(r) = \frac{p_F^2(r)}{2m}, \tag{4.7.5}$$

where m is the mass of the neutron or the mass of the proton, respectively.

As concern the primary particle, an impact parameter is chosen randomly on a disk outside the nucleus, perpendicular to a vector passing through the center of the nucleus. The initial direction of the primary is perpendicular to this disk.

Using straight-line transport, the distance of closest approach ${d_i}^{min}$ to each nucleon i in the target nucleus and the corresponding time-of-flight ${t_i}^d$ are calculated. The interaction cross-section σ_i with target nucleons is calculated based on the momenta of the nucleons in the nucleus and the projectile momentum. Target nucleons for which ${d_i}^{min} < (\sigma_i/\pi)^{1/2}$ are candidate collision partners for the primary. All candidate collisions are ordered by increasing ${t_i}^d$. In case no collision is found, a new impact parameter is chosen.

The primary particle is then transported in the nuclear field by the time step given by the time to closest approach for the earliest collision candidate. Outside the nucleus, particles travel along straight-line trajectories. Inside the nucleus, particles are propagated in the nuclear field. At the end of each step, the interaction of the collision partners is simulated using the scattering term, resulting in a set of candidate particles for further transport. The secondaries from a binary collision are accepted subject to Pauli's exclusion principle. In the allowed cases, the tracking of the primary ends, and the secondaries are treated like the primary. All secondaries are tracked until they react, decay or leave the nucleus, or until the cascade stops due to the fact that the mean energy of all propagating particles in the system is below a threshold. At this stage the state of affairs has to be treated by means of pre-equilibrium decay and de-excitation models. Hence, the residual participants (pre-fragment), and the nucleus in its current state are then used to define the initial state for pre-equilibrium decay [154] [155].

4.8 The Quantum Molecular Dynamics model

`G4QMDReaction` is a new native GEANT4 implementation [129] of the general Quantum Molecular Dynamics model (QMD) [130] [131]. Indeed, QMD is the quantum extension of the classical molecular dynamics model and is widely used to analyze various aspects of heavy ion reactions, especially for many-body processes, and in particular the formation of complex fragments. There are three major differences between the BIC and the QMD models, concerning the definition of a participant particle, the participant-participant interactions and the system potential term. Firstly, a participant particle in the BIC is either a primary particle, including nucleons in the projectile nucleus, or particles generated or scattered in the cascade, and only the participant particles are propagated in the nucleus. Furthermore, scattering between participant particles is not taken into account. In contrast, the entire nucleons in the target and projectile nuclei are considered as participant particles in the QMD model, in which participant-participant scatterings are naturally included. Secondly, while in the BIC the participant particles are tracked sequentially, all particles in the system are tracked simultaneously in the QMD. Finally, along with the time evolution of the system, its potential is also dynamically changed in the QMD, while the Hamiltonian is calculated from the simple time-independent optical potential in the BIC. Therefore QMD seem to accomplish more detailed treatments of the above three points, however with a cost of computing performances. The set of parameters in the QMD model were originally optimized to reproduce data in the energy range between 100 AMeV and 3 AGeV.

The basic assumption of QMD is that each nucleon state is represented by a Gaussian wave function of width L, given by:

$$\phi_i(\mathbf{r}) \equiv \frac{1}{(2\pi L)^{3/4}} exp\left[-\frac{(\mathbf{r}-\mathbf{r}_i)^2}{4L} + \frac{i}{\hbar}\mathbf{r}\cdot\mathbf{p}_i\right], \tag{4.8.1}$$

where $\mathbf{r}_i$ and $\mathbf{p}_i$ represent the center values of position and momentum of the *ith* particle. The total wave function is assumed to be a direct product of them.

The time evolution of $\mathbf{r}_i$ and $\mathbf{p}_i$ is described by Newtonian equations and the stochastic two-body collision term. Particle equations of motion are derived on the basis of the time-dependent variational principle as:

$$\dot{\mathbf{r}_i} = \frac{\partial H}{\partial \mathbf{p}_i}, \dot{\mathbf{p}_i} = -\frac{\partial H}{\partial \mathbf{r}_i} \tag{4.8.2}$$

where the Hamiltonian H consists of the single-particle energy including the mass term and the energy of the two-body interaction as:

$$H = \sum_i \sqrt{m_i^2 + \mathbf{p}_i^2} + V. \tag{4.8.3}$$

A Skyrme type interaction, a Coulomb interaction and a symmetry term are included in the effective potential V.

The time evolution of the QMD system is calculated until a certain time, typically 100 fm/c. The user can modify this value from the Physics List of GEANT4. After the termination of the time evolution, cluster identification is carried out in the phase space distribution of nucleons in the system. Each identified cluster is considered as a fragmented nucleus from the reaction and it usually has more energy than the ground state. Therefore, excitation energy of the nucleus is calculated and then the nucleus is passed on to other GEANT4 models like *Binary Cascade*. However, unlike *Binary Cascade* which passes them to *Precompound* and *Excitation models* by calling them inside of the model, the QMD uses excitation models directly.

Nucleus-Nucleus (NN) cross section is not a fundamental component of either QMD or BIC models. However without cross section, no meaningful simulation beyond the study of the NN reaction itself can be done. In other words, GEANT4 needs the cross section to decide where an NN reaction will happen in simulation geometry. Many cross section formulae for NN collisions are included in GEANT4, such as Tripathi [156] and Tripathi Light System [157], Shen [158], Kox [159] and Sihver [160]. These are empirical and parameterized formulae with theoretical insights and give total reaction cross section of wide variety of combination of projectile and target nucleus in fast. These cross sections are also used in the sampling of impact parameter in the QMD model.

4.9 Pre-equilibrium decay and de-excitation models

As already mentioned, at the end of the cascade, a fragment is formed for further treatment in *Precompound* and nuclear *De-excitation* models. These models need some information about the nuclear fragment created by the cascade. The fragment formed is characterized by several parameters, such as the number of nucleons in the fragment, the charge, the momentum of the fragment and so on, which are used as input parameter by the pre-equilibrium and de-excitation models.

The GEANT4 *Precompound* model is considered as an extension of the hadron kinetic model. It gives a possibility to extend the low energy range of the hadron kinetic model for nucleon-nucleus inelastic collision and it provides a "smooth" transition from kinetic stage of reaction, described by the hadron kinetic model, to the equilibrium stage of reaction, described by the equilibrium de-excitation models [154]. The *Precompound* model is applicable in the energy range 0 - 170 MeV. Only emission of neutrons, protons, deutrons, thritium and helium nuclei are taken into account. The precompound stage of nuclear reaction is considered until nuclear system is not an equilibrium state. Further emission of nuclear fragments or photons from excited nucleus is simulated using equilibrium models implemented in GEANT4, such as the *Evaporation*, the *Fermi break-up* and the *Statistical Multifragmentation* models.

At the end of the pre-equilibrium stage, the residual nucleus is supposed to be left in an equilibrium state, in which the excitation energy E^* is shared by a large number of nucleons. Such an equilibrated compound nucleus is characterized by its mass, charge and excitation energy with no further memory of the steps which led to its formation.

If the excitation energy is higher than the separation energy, it can still ejects nucleons and light fragments (d, t, ^{3}He, α), whose description is treated by the *Evaporation* model (for excited nuclei at relatively low excitation energies). These constitute the low energy and most abundant part of the emitted particles in the rest system of the residual nucleus. The emission of particles by the *Evaporation* model is based on Weisskopf and Ewing model [161]. *Fission* (for nuclei with $A > 65$) and *Photon Evaporation* can be treated as competitive channels in the evaporation model.

The *Statistical Multifragmentation* and *Fermi break-up* models are used at excitation energies E^* above 3 AMeV.

The *Multifragmentation* model is capable to predict final states as a result of a highly excited nucleus statistical break-up. The initial information for calculation of multifragmentation stage consists in the atomic mass number A, charge Z of excited nucleus and its excitation energy E^*. At higher excitation energies ($E^* > 3$ AMeV) the multifragmentation mechanism, when nuclear system can eventually breaks down into fragments, becomes the dominant. Later on, the excited primary fragments propagate independently in the mutual Coulomb field and undergo de-excitation [162].

The *Fermi break-up* model is capable to predict final states of excited nuclei with atomic number $Z < 9$ and $A < 17$. For light nuclei the values of excitation energy per nucleon are often comparable with nucleon binding

energy. Thus a light excited nucleus breaks into two or more fragments with branching given by available phase space. This statistical approach was first used by Fermi to describe the multiple production in high energy nucleon collision [163].

Appendix B
Nucleus-nucleus models in the FLUKA Monte Carlo code

FLUKA[3] [59] is a general purpose tool, jointly developed by CERN and INFN, for calculations of particle transport and interactions with matter. FLUKA covers an extended range of applications spanning from proton and electron accelerator shielding to target design, calorimetry, activation, dosimetry, detector design, Accelerator Driven Systems, cosmic rays, neutrino physics, radiotherapy.

Sixty different particles plus heavy ions can be transported by the code. The energy range covered for hadron-hadron and hadron-nucleus interaction is from threshold up to 10000 TeV, while electromagnetic and μ interactions can be dealt with from 1 keV up to 10000 TeV. Nucleus-nucleus interactions are also supported up to 10000 ATeV. Neutron transport and interactions below 20 MeV down to thermal energies are treated in the framework of a multi-group approach, with cross section data sets developed for FLUKA starting from standard evaluated databases (mostly ENDF/B-VI, JENDL and JEFF). Transport in arbitrarily complex geometries, including magnetic field, can be accomplished using the FLUKA combinatorial geometry.

FLUKA is based, as far as possible, on original and well tested microscopic models. Due to this "microscopic" approach to hadronic interaction modelling, each step is self-consistent and has solid physical bases. Performances are optimized comparing with particle production data at single interaction level. No tuning whatsoever is performed on "integral" data.

[3] Fluktuierende Kaskade (*Fluctuating Cascade*).

Therefore, final predictions are obtained with a minimal set of free parameters, fixed for all energies and target/projectile combinations.

As it is known, nuclear processes in heavy ion collisions differ as a function of energy. In the energy interval of therapeutic interest, interaction mechanisms go from pure fragmentation at highest energies to more complex ones at the lowest energies. Depending on the nuclear structure of the interacting ions and on the impact parameter, the low energy reaction mechanisms vary from Coulomb Scattering to *deep inelastic processes* and fusion, complete and incomplete. However, FLUKA cannot be defined as a toolkit like GEANT4, but its physical models are fully integrated. Regarding the FLUKA code nucleus-nucleus reactions relevant for therapeutic applications, they are treated thanks to the interfaces with the rQMD [148] and the new BME [146] event generator.

In the following, some of the most important features of these two models implemented in FLUKA, relevant to reproduce the carbon fragmentation data at relativistic energies shown in Chapter 4, are briefly outlined. Description of other FLUKA models and extensive benchmarking can be found in the literature[4].

4.10 The rQMD model in FLUKA

Quantum Molecular Dynamics (QMD) approaches are a viable solution for nucleus-nucleus reactions as they represent a suitable way to describe the initial hot stage of heavy ion reactions. Indeed QMD models can be described as an improvement over classical Intra Nuclear Cascade (INC) codes, thanks to their dynamic modelling of the nuclear field among nucleons during the reaction (cfr. Appendix A). The treatment of individual two-body scattering/interactions is usually based on similar approaches for INC and QMD codes. Unfortunately, initialization of the projectile and target nuclear states is often difficult and their relativistic extension somewhat problematic.

The rQMD-2.4 [148] is a relativistic QMD model which has been applied successfully to relativistic A-A particle production over a wide energy range, from $\approx$ 100 AMeV up to 5 AGeV. Like the non-relativistic QMD, rQMD combines the classical propagation of the hadrons (molecular dynamics) with some quantum effects such as stochastic scattering, particle decay, and Pauli blocking in collisions.

Particularly, there are two main differences between the rQMD with

[4] http://www.fluka.org.

respect to the non-relativistic QMD model. A model of nucleus-nucleus collisions in the ultrarelativistic energy domain must be explicitly Lorentz invariant. The results of non-relativistic models become, with growing energies, more and more observer frame dependent. Compared to non-relativistic phase space models, the phase space in rQMD is enlarged to 8N dimensions (the positions and momenta of the N particle as 4-vectors). The propagation by a non-relativistic Hamiltonian in QMD is substituted in rQMD by equations of motion which are Lorentz invariant, because the Hamiltonian is a Lorentz scalar phase space function.

Regarding the implementation of the model in the FLUKA code, it has to be stressed that several improvements are ongoing. Indeed, the original version of the rQMD code did not identify nucleon clusters in the final state. Thus their de-excitation by pre-equilibrium emissions, fission, evaporation, or fragmentation could not be evaluated. This was a quite severe limitation: in fact, because of huge kinematical effects, ejectiles having low energy in the reference frame of the decaying projectile-like nucleus may contribute to the highest energy side of observed spectra at forward angles. At bombarding energies of interest, serious energy non-conservation issues were also affecting the original code, particularly when run in full QMD mode[5]. Therefore a meaningful calculation of residual excitation energies was impossible.

Then it has been developed a modified version of rQMD-2.4, where projectile- and target-like residues are identified by gathering the spectator nucleons, and their excitation energies are assumed to be essentially due to the holes left by the hit nucleons. Moreover, the exact energy balance is assured taking into account the experimental binding energies of nuclei, as is the case for all other models used in FLUKA. After these improvements, the fragment final de-excitation can be reasonably evaluated by the FLUKA evaporation/fission/fragmentation module.

4.11 The BME model in FLUKA

In order to extend the FLUKA capability to simulate heavy ion inelastic interaction, from the rQMD lower limit at 100 AMeV down to threshold, a suitable event generator based on the Boltzmann Master Equation (BME) theoretical approach has been implemented [146].

Beyond just providing general completeness in FLUKA's performances,

[5] rQMD-2.4 can run either in full QMD mode or in the so called *fast cascade mode* where it behaves like an Intra Nuclear Cascade code.

the motivation to extend the treatment of heavy ion interactions to these near threshold energies comes from the need to simulate the stopping processes involving heavy ion beams which are employed in radiation therapy.

Indeed, many different reaction mechanisms may concur to an heavy ion interaction: mean field interactions, break-up of the projectile and the target, inelastic scattering, the formation of non-equilibrated nuclei reaching a state of thermal equilibrium through a sequence of two-body interactions leading to the emission of fast particles (*thermalization*). The de-excitation process of the non-equilibrated nuclei which may be created is described, within the FLUKA code, by means of the BME model. It is a nucleon transport model based on nucleon-nucleon collision processes in the nuclear potential and describes the statistical evolution of a sample of systems, which evolve from an initial state, far from statistical equilibrium, to an equilibrium state through a sequence of two body interactions and emission of unbound particles to the continuum [164].

The nucleons of the two ions are assumed to exchange energy in standard conditions, i.e., not considering strongly compressed nuclear matter. In such a case, which is expected to occur when the kinetic energy of the ions is not too large, the nucleon energy exchanges produce a nuclear friction which damps the relative motion of the two ions. In the course of this thermalization, unbound particles may be emitted, greatly reducing the excited nucleus energy. It is assumed that the thermalization ends and an equilibrated system is produced when the probability of emission of fast particles becomes negligible and the hardest part of the spectrum of the emitted particles saturates. The thermal equilibrium states which are produced at the end of the thermalization phase of the reaction further de-excite by evaporation of particles and γ-ray emissions until a cold residual nucleus is formed.

The BME theory thus unifies the description of nucleon induced and heavy ion reactions even considering the much greater complexity of the last processes.

Acknowledgements

Since I am coming to the conclusion of the Ph.D. course, there are certainly many people to thank that supported me in different ways.

The first person I would like to thank is Dr. Giacomo Cuttone, who encouraged me to undertake the Ph.D., having trust in me, and for this reason I thank him sincerely. During these three years Dr. Titti Agodi has definitely been another very important person for me, as she has always been helpful listening to me and helping me in the most difficult moments of my work.

It was also essential for me to work with Dr. Francesco Cappuzzello who has always made his deep knowledge of nuclear physics available to me in order to deeply understand the most problematic aspects of the work done in these years.

I would also like to thank Dr. Marzio De Napoli, who has followed the progress of my work, being always available for any questions or problems, even of practical nature, giving me very useful suggestions and advice.

Since during the Ph.D. I have had the opportunity to work for the first time as a part of a scientific collaboration, I would like to especially thank those members who have welcomed me into their group in order to carry out a specific part of the data analysis. I learned very much from the time I spent at the Politecnico, in Turin, working with Riccardo Introzzi, Francesca Balestra and Hannan Younis, a group led by Prof. Iazzi. I would like to thank all of them for the fruitful days spent working together.

I would like also to thank the group of the Università "La Sapienza", in Rome, Vincenzo Patera and Alessio Sarti. Alessio's collaboration was particularly precious inasmuch he gave me the opportunity to understand the work to be done and also he was the person who gave me the tools to move forward and to work independently, even if in a collaboration framework. Of course all the people in the collaboration project have been very important for me and for the work done.

As far as many activities have been carried out in these three years, I would like to thank my group at LNS: Dario Nicolosi, Diana Carbone, Mariangela Bondì, Prof. Angelo Cunsolo, Prof. Nino Foti and Dr. Manuela Cavallaro. Particularly the work done together with Manuela has been very important for me as I had the opportunity of training on new subjects.

My thoughts now go to my roommates, who have represented a unique support throughout these three years, they are: Tiziana Licciardello, Sara La Rosa, Giuseppe Castro, Giuseppe Torrisi, Turi Viola and Sara Pulvirenti and to all my friends at the LNS. Thanks a lot guys for the moments of fun and sharing!

A special thank goes to my friends who went along with this *journey*: Daniela Campo, Rosalba Miracoli, Alessandra Blancato, Giusy Larosa, Agata Trovato, Nadia Gambino and Daniele Sardina.

My biggest thanks go to my family, without you all of this would not be possible in these three years, I love you.

Bibliography

[1] American Cancer Society, *Global Cancer Facts & Figures 2nd Edition*, Atlanta, 2011.

[2] J. Ferlay, H.-R. Shin, F. Bray, D. Forman, C. Mathers and D.M. Parkin. *GLOBOCAN 2008 v2.0, Cancer Incidence and Mortality Worldwide: IARC CancerBase N°10.* Lyon, France: International Agency for Research on Cancer, 2010. Available from: http://globocan.iarc.fr.

[3] International Atomic Energy Agency, *Relative biological effectiveness in ion beam therapy*, jointly sponsored by the International Atomic Energy Agency and the International Commission on Radiation Units and Measurements. Technical reports series no. 461, Vienna, 2008.

[4] W.C.Röntgen, *Über eine neue Art von Strahlen.* Vorläufige Mitteilung. In: Sitzungsberichte der physikalisch-medicinischen Gesellschaft zu Würzburg, Sitzung 30, 132-141 (1895).

[5] W.C. Röntgen, *On a new kind of Rays*, translated by Arthur Stanton, Nature 53, 274-277 (1896).

[6] L. Freund, *Elements of General Radiotherapy for Practitioners*, Rehman, New York (1904).

[7] W.D. Coolidge, *A powerful Röntgen ray tube with a pure electron discharge.* Physical Review 2, 409-413 (1913).

[8] *Report from the International X-Ray Unit Committe*, American Journal of Roentgenology, 20:470 (Nov.) 1928.

[9] E. B. Podgorsak et al., *Radiation oncology physics: a handbook for teachers and students*, International Atomic Energy Agency, Vienna (2005).

[10] R.J. Van de Graaff, *A 1.500.000 volt electrostatic generator*. Physical Review 38, 1919-1920 (1931).

[11] D.W. Kerst, *The acceleration of electrons by magnetic induction*. Physical Review 60, 47-53 (1941).

[12] C.W. Miller, *Travelling-Wave Linear Accelerator for X-Ray Therapy*, Nature 171, 297-298 (1953).

[13] W. Wieszczycka and W.H. Schaf, *Proton Radiotherapy Accelerators*. World Scientific Publishing Co. Pte. Ltd. (2001).

[14] U. Amaldi et al., *Accelerators for hadrontherapy: From Lawrence cyclotrons to linacs*, Nuclear Instruments and Methods in Physics Research A 620, 563-577 (2010).

[15] E.O. Lawrence, M.S. Livingston, *Production of high speed light ions without the use of high voltages*, Physical Review 40, 19-35 (1932).

[16] H. Childs, *An American genius: the life of Ernest Orlando Lawrence*, E.P. Dutton & Co., New York (1968).

[17] R.S. Stone, *Neutron therapy and specific ionization*, American Journal of Roentgenology 59, 771-785 (1948).

[18] R. Wilson. *Radiological use of fast protons*, Radiology 47, 487-491 (1946).

[19] W.H. Bragg, *On the α-particles of radium and their loss of range in passing through various atoms and molecules*, Philosophical Magazine 10, 318-340 (1905).

[20] C. A. Tobias, *Heavy charged particles in cancer therapy, radiobiology and radiotherapy*, National Cancer Institute Monograph N°24 (1967).

[21] Chu W.T. et al., *Instrumentation for Treatment of Cancer Using Proton and Light-Ion Beams*, Review of Scientific Instruments, Accelerator & Fusion Research Division, LBL-33403 UC-406 Preprint (1993).

[22] G.A.P. Cirrone et al., *A 62-MeV Proton Beam for the Treatment of Ocular Melanoma at Laboratori Nazionali del Sud-INFN*, IEEE Transactions On Nuclear Science, 51, 860-865 (2004).

[23] U. Amaldi, *History of hadrontherapy in the world and Italian developments*, Rivista Medica, vol. 14, N. 1, 7-22 (2008).

[24] J.R. Castro, *Heavy ion therapy: the BEVALAC epoch*. U. Amaldi, B. Larsson (editors): Hadrontherapy in oncology, Elsevier, Amsterdam, 208-216 (1994).

[25] Y. Hirao et al., *Heavy ion synchrotron for medical use - HIMAC project at NIRS - Japan*, Nuclear Physics A 538, 541-550 (1992).

[26] ICRU Report 51, *Quantities and Units in Radiation Protection Dosimetry*, International Commission on Radiation Units and Measurements (ICRU), Bethesda (1993).

[27] U. Amaldi and M. Silari, *The Blue Book: the TERA Project and the Centre of Oncological Hadrontherapy*, Vol. I-II, INFN-LNF, Frascati, Italy (1995).

[28] P. Peschke et al., *Relative Biological Effectiveness of Carbon Ions for Local Tumor Control of a Radioresistant Prostate Carcinoma in the Rat*, International Journal of Radiation Oncology, Biology and Physics, 79, 239-246 (2011).

[29] D. Schardt et al., *Heavy-ion tumor therapy: Physical and radiobiological benefits*, Review of Modern Physics 82, 383-425 (2010).

[30] G. Kraft and M. Krämer, *Linear Energy Transfer and Track Structure*, Advances in Radiation Biology 17, 1-52 (1993).

[31] W.K. Weyrather, *Medical Applications of Accelerated Ions*, Lecture Notes in Physics 651, 469-490 (2004).

[32] C.A. Tobias et al., *Radiological Use of High Energy Deuterons and Alpha Particles*, American Journal of Roentgenology 67, 1-27 (1952).

[33] H. Bethe, *Zur theorie des durchgangs schneller korpuskularstrahlen durch materie*. Annalen der Physik, 397(3), 325-400 (1930).

[34] F. Bloch, *Bremsvermögen von Atomen mit mehreren elektronen*, Zeitschrift für Physik A: Hadrons Nuclei 81, 363-376 (1933).

[35] U. Fano, *Penetration of protons, alpha particles, and mesons*, Annual Review of Nuclear and Particle Science 13, 1-66 (1963).

[36] J.F. Ziegler, *SRIM-2003 - Beam Interactions with Materials and Atoms* Nuclear Instruments and Methods in Physics Research Section B, 1027-1036 (2004).

[37] H. W. Barkas, *Nuclear Research Emulsions* Vol. 1, Academic Press New York and London (1963).

[38] T. Elsässer et al., *The relevance of very low energy ions for heavy-ion therapy*, Physics in Medicine and Biology 54, 101-106 (2009).

[39] P. V. Vavilov, *Ionizational losses of high energy heavy particles*, Zh. Eksp. Teor. Fiz. 32, 920-923 (1957) [Sov. Phys. JETP 5, 749-751 (1957)]

[40] N. Bohr, *Scattering and stopping of fission fragments*, Physical Review 58, 654-655 (1940).

[41] S. P. Ahlen, *Theoretical and experimental aspects of the energy loss of relativistic heavily ionizing particles*, Review of Modern Physics 52, 121-173 (1980).

[42] D. Schardt et al., *Precision Bragg-curve measurements for light ion beams in water*, GSI-Report, 373 (2008).

[43] Parodi K., *On the feasibility of dose quantification with in-beam PET data in radiotherapy with ^{12}C and proton beams*, Ph.D. thesis, Technische Universität Dresden, Fakultät Mathematik und Naturwissenschaften (2004).

[44] U. Weber, *Volumenkonforme Bestrahlung mit Kohlenstoffionen*, PhD-Thesis, Universitat Gh Kassel (1996).

[45] G. Molière, *Theorie der Streuung schneller geladener Teilchen II, Mehrfach-und Vielfachstreuung*, Z. Naturforschung A 3A, 78-97 (1948).

[46] H. A. Bethe, *Moliere's theory of multiple scattering*, Physical Review, 89(6), 1256-1266 (1952).

[47] V. L. Highland, *Some Practical Remarks on Multiple Scattering*, Nuclear Instruments and Methods 129, 497-499 (1975).

[48] B. Gottschalk et al., *Multiple Coulomb Scattering of 160 MeV Protons*, Nuclear Instruments and Methods B74, 467-490 (1992).

[49] Y. S. Tsai, *Pair production and bremsstrahlung of charged leptons*, Review of Modern Physics 46, 815-851 (1974).

[50] W.T.T. Chu, *Overview of light-ion beam therapy*, Dose Reporting in Ion Beam Therapy, IAEA-TECDOC-1560, 5-28 (2007).

[51] R. Serber, *Nuclear reactions at high energies*, Physical Review 72, pp. 1114-5 (1947).

[52] J. J. Bevelacqua, *Systematics of heavy ion radiotherapy*, Radiation Protection managment 22, 4-13 (2005).

[53] S. Kox et al., *Trends of total reaction cross sections for heavy ion collisions in the intermediate energy range*, Physical Review C35, 1678 (1987).

[54] M. Krämer, *Swift ions in radiotherapy - Treatment planning with TRiP98*, Nuclear Instruments and Methods in Physics Research Section B 267, 989-992 (2009).

[55] M. Krämer and M. Durante, *Ion beam transport calculations and treatment plans in particle therapy*, The European Physical Journal D60, 195 (2010).

[56] L .Sihver and D.Mancusi, *Present staus and validation of HIBRAC*, Radiation Measurements 44, 38 (2009).

[57] S. Agostinelli et al.(Geant4 Collaboration), *GEANT4 - A simulation toolkit*, Nuclear Instruments and Methods 506, 250-303 (2003).

[58] J. Allison et al.(Geant4 Collaboration), *Geant4 Developments and Applications*, IEEE Transactions On Nuclear Science 53, 270-8 (2006).

[59] G. Battistoni et al., *The FLUKA code: description and benchmarking*, AIP Conf. Proc. Hadronic Shower Simulation Workshop 2006, 896 31-49 (2007).

[60] A. Fassò et al., *FLUKA: a multi-particle transport code*, Technical Report CERN-2005-10, INFN/TC 05/11, SL AC-R-773 (2005).

[61] G. Hughes et al., *MCNPXTM: the LAHETTM/MCNPTM code merger*, KEK Proc. 3rd Workshop on Simulating Accelerator Radiation Environments (SARE 3) (Tsukuba, Japan, 7-9 May) p 44-51 (1997).

[62] LANL 2002 MCNPX Users Manual Version 2.4.0.

[63] A.V. Dementyev and N.M. Sobolevsky, *SHIELD universal Monte Carlo hadron transport code: scope and applications*, Radiation Measurements 30, 553-7 (1999).

[64] I. Gudowska et al., *Ion beam transport in tissue-like media using the Monte Carlo code SHIELD-HIT*, Physics in Medicine and Biology 49, 1933-58 (2004).

[65] K. Niita et al., *PHITS: a particle and heavy ion transport code system*, Radiation Measurements 41, 1080-90 (2006).

[66] M.C. Morone et al., *Monte Carlo simulation to evaluate the contamination in an energy modulated carbon ion beam for hadron therapy delivered by cyclotron*, Physics in Medicine and Biology 53, 6045 (2008).

[67] T.T. Böhlen et al., *Benchmarking nuclear models of FLUKA and GEANT4 for carbon ion therapy*, Physics in Medicine and Biology 55(19), 5833 (2010).

[68] A. Mairani, *Nucleus-nucleus interaction modelling and applications in ion therapy treatment planning*, Ph.D. Thesis, University of Pavia (2007).

[69] F. Sommerer et al., *Investigating the accuracy of the FLUKA code for transport of therapeutic ion beams in matter*, Physics in Medicine and Biology 51, 4385-98 (2006).

[70] I. Pshenichnov et al., *Nuclear fragmentation reactions in extended media studied with Geant4 toolkit*, Nuclear Instruments and Methods B 268, 604-15 (2010).

[71] J.H. Heinbockel et al., *Comparison of the transport codes HZETRN, HETC and FLUKA for a solar particle event*, Advances in Space Research 47, 1079-1088 (2011).

[72] J. Hüfner, *Heavy fragments produced in proton-nucleus and nucleus-nucleus collisions at relativistic energies*, Physics Reports 125 (1985).

[73] W. Enghart et al., Strahlenther. Onkol. 175, Suppl. II 33-36 (1999).

[74] K. Parodi et al., *Experimental study on the feasibility of in-beam PET for accurate monitoring of proton therapy*, IEEE Transactions on Nuclear Science 52, 778-786 (2005).

[75] W. Enghardt et al., *Charged hadron tumour therapy monitoring by means of PET*, Nuclear Instruments and Methods in Physics Research Section A 525, 284-288 (2004).

[76] G. Kraft, *Tumor therapy with heavy charged particles,* Progress in Particle and Nuclear Physics 45, S473-S544 (2000).

[77] R. Katz and F. A. Cucinotta, *Tracks to therapy*, Radiation Measurements 31, 379-388 (1999).

[78] M. Krämer, *Calculations of heavy-ion track structure*, Nuclear Instruments and Methods in Physics Research B 105, 14-20 (1995).

[79] M. N. Varma et al., *Radial dose, LET, and W for* ^{16}O *ions in* N_2 *and tissue-equivalent gases*, Radiation Research 70, 511-518 (1977).

[80] U. Amaldi and G. Kraft, *Radiotherapy with beams of carbon ions*, Report on Progress in Physics 68, 1861-1882 (2005).

[81] T. Kanai et al., *Biological and physical proposal for a heavy-ion clinical trial*, Proc. 3rd Workshop on Physics Biological Research with Heavy Ions (2-3 September 1993) NIRS M 99, HIMAC 006, pp 7-11.

[82] E. Hall, *Radiobiology for the Radiologist*, 5th ed., Lippincott Williams and Wilkins, Philadelphia (2000).

[83] W.K. Weyrather et al., *RBE for carbon track-segment irradiation in cell lines of differing repair capacity*, International Journal of Radiation Biology 75, 1357-1364, (1999).

[84] E. A. Blakely et al., *Inactivation of human kidney cells by high energy monoenergetic heavy-ion beams*, Radiationt Research 80, 122-160 (1979).

[85] A. Staab, *Response of Chinese hamster v79 multicellular spheroids exposed to high-energy carbon ions*, Radiation Research 161, 219-227 (2004).

[86] H. Paganetti et al., *Relative biological effectiveness RBE values for proton beam therapy*, International Journal of Radiation Oncology, Biology and Physics 53, 407-421 (2002).

[87] M. Belli, *RBE-LET relationships for cell inactivation and mutation induced by low energy protons in V79 cells: Further results at the LNL facility*, International Journal of Radiation Biology 74, 501-509 (1998).

[88] Y. Furusawa et al., *Inactivation of aerobic and hypoxic cells from three different cell lines by accelerated ^{3}He, ^{12}C ^{20}Ne ion-beams*, Radiation Research 154, 485-496 (2000).

[89] M. Scholz, *Effects of ion radiation on cells and tissues*, Advances in Polymer Science 62, 96-155 (2003).

[90] M. Suzuki et al., *Correlation between cell killing and residual chromatin breaks measured by PCC in six human cell lines irradiated with different radiation types*, International Journal of Radiation Biology 76, 1189-1196 (2000).

[91] M. Krämer and M. Scholz, *Treatment planning for heavy ion therapy*, Phys. Med. Biol. 45 3319-30 (2000).

[92] O. Jäkel, *Treatment planning for heavy ion radiotherapy: Clinical implementation and application*, Physics in Medicine and Biology 46, 1101-1116 (2001).

[93] S. Rossi and R. Orecchia, *The National Centre of Oncological Hadrontherapy (CNAO) project*, Rivista Medica, Vol.14 N.1, 69-79, 2008.

[94] C. Agodi et al., *The INFN TPS project*, Il Nuovo Cimento 31, 1, 99-108 (2008).

[95] E. Schmitt et al., *Treatment Planning System (TPS) for Carbon Ion Therapy: The INFN TPS project*, submitted to the refereed conference proceedings of the XLIX International Winter Meeting on Nuclear Physics (2011).

[96] L. Falbo, *Adavanced accelerator technology aspects for hadrontherapy*, Proceedings of HIAT 2012, Chicago, IL USA.

[97] T. Kanai et al., Medical Physics 7, 365-369 (1980).

[98] E. Pedroni et al., Medical Physics 22, 27-53 (1995).

[99] Th. Haberer et al., Nuclear Instruments and Methods in Physics Research A 330, 296-305 (1993).

[100] M. Donetti et al., Dose Delivery at CNAO, PTCOG51, Seoul (2012).

[101] http://ptcog.web.psi.ch/

[102] G. Raciti et al., *Experimental Evidence of* ^{2}*He Decay from* ^{18}*Ne Excited States*, Physical Review Letters 100, 192503 (2008).

[103] R. Pleskac et al., *The FIRST experiment at GSI*, Nuclear Instruments and Methods in Physics Research A 678, 130-138 (2012).

[104] Z. Abou-Haidar et al., *Performance of upstream interaction region detectors for the FIRST experiment at GSI*, Journal of Instrumentation 7, P02006 (2012).

[105] E. Spiriti, M. De Napoli, F. Romano et al., *The FIRST experiment: interaction region and MAPS vertex detector*, Nuclear Physics B - Proceedings Supplements, Volume 215, Issue 1, Pages 157-161 (2011).

[106] G. Deptuch et al., *Monolithic Active Pixel Sensors with In-Pixel Double Sampling Operation and Column-Level Discrimination*, IEEE Transactions on Nuclear Science 51, 2313-2321 (2004).

[107] J. Hubele et al., Zeitschrift für Physik A 340, 263 (1991).

[108] C. Sfienti et al., Proceedings of the XLI International Winter Meeting on Nuclear Physics, Bormio, Italy, p.323 (2003).

[109] C. Sfienti et al., Physical Review Letters 102, 152701 (2009).

[110] G. Bauer et al., Nuclear Instruments and Methods in Physics Research Section A 386, 249 (1997).

[111] A. Schüttauf et al., Nuclear Physics A 607, 457 (1996).

[112] C. Agodi et al., *The HADES time-of-flight wall*, Nuclear Instruments and Methods in Physics Research A 492, 14-25 (2002).

[113] T. Blaich et al., Nuclear Instruments and Methods in Physics Research Section A 314, 136 (1992).

[114] K. Boretzky et al., Physical Review C68, 024317 (2003).

[115] H. G. Essel, N. Kurz, IEEE Transactions on Nuclear Science NS-47(2), 337 (2000).

[116] https://www.gsi.de/informationen/wti/ee/elekt_entwicklung/vulom_m_e.html

[117] M. De Napoli et al., *Carbon fragmentation measurements and validation of the GEANT4 nuclear reaction models for hadrontherapy*, Physics in Medicine and Biology 57, 7651-7671 (2012).

[118] M. De Napoli, *Mass and Isospin Effects in Multifragmentation*, Ph.D. Thesis, University of Catania (2005).

[119] R. Glasow et al., *Projectile like fragment production in ^{14}N-induced reactions at projetile energies of 60 MeV*, Nuclear and Particle Physics 16, 1089-1094 (1990).

[120] R. Dayras et al., *Peripheral Interactions for 44 MeV/u ^{49}Ar on ^{27}Al and ^{nat}Ti targets*, Nuclear Physics A460, 299-323 (1986).

[121] O.B. Tarasov et al., *Production of nuclei in $^{32,34,36}S$-induced reactions in the energy range 6-75 MeV/A* , Nuclear Physics A 629, 605-620 (1998).

[122] J. Czudek et al., *Fragmentation of ^{12}C projectiles interacting with ^{12}C, ^{27}Al, and ^{58}Ni nuclei at energy 28.7 MeV/nucleon*, Physical Review C 43, 1248-54 (1991).

[123] C. Guet, *Some aspects of intermediate energy heavy ion reactions*, Nuclear Physics A400, 191c-220c (1983).

[124] C. Pruneau et al., *Peripheral collisions of 40 MeV/u ^{14}N with a ^{197}Au target*, Nuclear Physics A500, 168-194 (1989).

[125] O. Tarasov, *Analysis of momentum distributions of projectile fragmentation products*, Nuclear Physics A734, 536-540 (2004).

[126] B.V. Jacak et al., *Fragment production in intermediate energy heavy ion reactions*, Physical Review C 35, 1751-1788 (1987).

[127] R. Wada et al., *Temperatures and excitation energies of hot nuclei in the reactions of ^{32}S+Ag and ^{16}O+Ag at 30 MeV/nucleon*, Physical Review C 39, 497-515 (1989).

[128] G. Folger et al., *The Binary Cascade nucleon nuclear reactions*, European Physical Journal A21, 407-417 (2004).

[129] T. Koi, *New native QMD code in Geant4*, Joint International Conference on Supercomputing in Nuclear Applications and Monte Carlo 2010 (SNA + MC2010) Hitotsubashi Memorial Hall, Tokyo, Japan, October 17-21 (2010).

[130] K. Niita, *Analysis of the (N,xN') reactions by quantum molecular dynamics plus statistical decay model*, Physical Review C 52, 2620-2635 (1995).

[131] J. Aichelin, *"Quantum" molecular dinamics - A dynamical microscopic n-body approach to investigate fragment formation and the nuclear equation of state in heavy ion collisions*, Physics reports (Review Section of Physics Letters) 202, North-Holland, 233-360 (1991).

[132] K. Parodi et al., *The FLUKA code for application of Monte Carlo methods to promote high precision ion beam therapy* Proc. 12th Int. Conf. on Nucl. React. Mech. (Varenna, Italy, 15-19 June 2009).

[133] N. Matsufuji et al., *Spatial fragment distribution from a therapeutic pencil-like carbon beam in water*, Physics in Medicine and Biology 50, 3393-3403 (2005).

[134] T. Toshito et al., *Measurements of total and partial charge-changing cross sections for 200 to 400 MeV/nucleon* ^{12}C *on water and polycarbonate*, Physics Review C 75, 054606 (2007).

[135] I. Schall et al., *Charge-changing nuclear reactions of relativistic light-ion beams* ($5 \leq Z \leq 10$) *passing through thick absorbers*, Nuclear Instruments and Methods B 117, 221-234 (1996).

[136] K. Gunzert-Marx et al., *Secondary beam fragments produced by 200* $MeVu^{-1}$ ^{12}C *ions in water and their dose contributions in carbon ion radiotherapy*, New Journal of Physics 10, 075003 (2008).

[137] B. Braunn et al., *Nuclear reaction measurements of 95 MeV/u* ^{12}C *interactions on PMMA for hadrontherapy*, Nuclear Instruments and Methods in Physics Research B 269, 2676-2684, (2011).

[138] www.gammex.com

[139] International Union of Pure and Applied Chemistry (IUPAC), *Compendium of Chemical Terminology*, Gold Book, Version 2.3.2, 2012-08-19 (http://goldbook.iupac.org/).

[140] https://groups.nscl.msu.edu/lise/lise.html

[141] http://www.srim.org/

[142] C. Sfienti et al., *Mass and Isospin Effects in Multifragmentation*, Nuclear Physics A 749, 83c-92c (2005)

[143] M. Golovkov et al., *Fragmentation of 270 AMeV carbon ions in water*, 1st International Week on Hadrontherapy: Advances in Hadron Therapy, Archamps, France; 1995, pp. 316-324(CERN, Geneva, 1997).

[144] H.W. Bertini et al., *Calculated nucleon spectra at several angles from 192-, 500-, 700-, and 900-MeV ^{12}C on ^{56}Fe*, Physical Review C 14, 590-595 (1976).

[145] V. Andersen et al., *The FLUKA code for space applications: recent developments* Advances in Space Research 34, 1302-10 (2004).

[146] F. Cerutti, G. Battistoni et al., *Low energy nucleus-nucleus reactions: the BME approach and its interface with FLUKA* Proc. 11th Int. Conf. on Nucl. React. Mech. (Varenna, Italy, 12-16 June) pp 507-11 (2006).

[147] R.K. Tripathi F.A. Cucinotta and J.W. Wilson, *Accurate universal parameterization of absorption cross-sections III-light systems*, Nuclear Instruments and Methods B 155, 349-56 (1999).

[148] H. Sorge, H. Stocker and W. Greiner, *Relativistic Quantum Molecular Dynamics Approach to Nuclear Collisions at Ultrarelativistic Energies*, Nuclear Physics A498, 567c-576c (1989).

[149] A. Fassò et al., *The physics models of FLUKA: status and recent developments*, Computing in High Energy and Nuclear Physics, 24-28 March 2003, La Jolla, California.

[150] F. Romano, *Monte carlo simulations of carbon ions fragmentations in hadrontherapy*, Ph.D. Thesis, University of Catania (2009).

[151] G. Folger and P. Wellisch, *Computing in High Energy Physics and Nuclear Physics*, Interlaken, Switzerland, 27 Sep - 1 Oct 2004, pp. 313.

[152] M.E. Grypeos et al., Journal of Physics G 17, 1093 (1991).

[153] L.R.B Elton, Nuclear Sizes (Oxford University Press, Oxford, 1961).

[154] K. K. Gudima et al., *Cascade-Exciton Model of Nuclear Reactions*, Nuclear Physics A401, 329 (1983).

[155] V. Lara and J.P. Wellisch, *Pre-equilibrium and equilibrium decays in GEANT4*, published in Annecy 2000, Proceedings of the IX International Conference on Calorimetry in High Energy Physics, Annecy, France, 9-14 October, 2000, Frascati Physics Series, Vol. XXI (2001) p. 449.

[156] R. K. Tripathi, F. A. Cucinotta and J. W. Wilson, *Universal Parameterization of Absorption Cross Sections*, NASA Technical Paper TP-3621 (1997).

[157] R. K. Tripathi, F. A. Cucinotta and J. W. Wilson, *Universal Parameterization of Absorption Cross Sections*, NASA Technical Paper TP-209726 (1999).

[158] W. Shen, B. Wang, J. Feng, W. Zhan, Y. Zhu and E. Feng, *Total reaction cross section for heavy-ion collisions and its relation to the neutron excess degree of freedom*, Nuclear Physics. A 491, 130-146 (1989).

[159] S. Kox, A. Gamp, C. Perrin et al., *Trends of total reaction cross sections for heavy ion collisions in the intermediate energy range*, Physics Review C 35, 1678-1691 (1987).

[160] L. Sihver, C. H. Tsao, R. Silberberg, T. Kanai, and A. F. Barghouty, *Total reaction and partial cross section calculation in proton-nucleus ($Z_t \leq 26$) and nucleus-nucleus reactions (Z_p and $Z_t \leq 26$)*, Physics Review C 47, 1225-1236 (1993).

[161] V.E. Weisskopf and D.H. Ewing, Physics Review 57, 472 (1940).

[162] J.P. Bondorf et al., Physics Report 257, 133 (1995).

[163] E. Fermi, Progress of Theoretical Physics 5, 1570 (1950).

[164] M. Cavinato et al., *Boltzmann master equation theory of angular distributions in heavy-ion reactions*, Nuclear Physics A 643, 15 (1998).